POLITECNICO DI TORINO

Master of Science Degree in Aerospace Engineering
Academic Year 2023/2024

Master's Degree Thesis

Characterisation and Simulation of Reusable Single-Stage-To-Orbit Vehicles Ascent Phase during Conceptual Design

Supervisors:
Dott.ssa Roberta Fusaro
Prof.ssa Nicole Viola
Ing. Valeria Borio

Candidate:
Roberto Cau

April 2024

A mia mamma e mio babbo,
che hanno sempre creduto in me
e hanno reso tutto ciò possibile.

A mia sorella,
la mia fan n°1.

Alla mia famiglia e i miei amici,
che mi hanno sempre supportato.

A Virginia,
che ha reso tutto più bello.

Abstract

The increasingly larger request for access to space, driven by the constant growth of the space economy, leads to the request for new tools capable of performing fast and reliable mission designs. In this context, this master's thesis is part of a research project of Politecnico di Torino whose purpose is to develop a software tool to support the conceptual design of access-to-space missions with reusable vehicles. In particular, this tool will be able to guide researchers and engineers throughout the very first design phases, allowing the user to carry out quick but reliable analysis of alternative mission concepts. This thesis focuses on the conceptual design of the ascent phase of reusable Single Stage to Orbit (SSTO) launchers. Particular attention is paid to horizontal take-off and landing (HTOL) vehicles, given the growing interest and potential in the field of reusable launchers. The thesis has been carried out in collaboration with other two colleagues, whose work is focused on the sizing methodology and tool integration, and the analysis of the descent phase.

At first, high-level requirements for the ascent phase of a reusable single-stage access to space vehicle are elicited. Subsequently, the problem of aerodynamic and propulsive characterisation of the vehicles is tackled, using a multi-fidelity approach. From the aerodynamic perspective, various analytical models already available in literature are analysed to identify the most suitable for a conceptual design of the ascent phase, in case numerical or experimental databases are not available. Taking vehicle geometrical data as input (e.g. the total volume of the vehicle, the wetted surface, the wing span), these analytical models shall provide as output the aerodynamic coefficients as a function of flight conditions (i.e., Mach number, angle of attack), spanning from subsonic to hypersonic regimes. The most promising models have been published by Curran, Williams and Torenbeek, while the Raymer model is considered not applicable, due to its limitation to configurations with a clear distinction between the fuselage and the delta wing, which made it not appliable for blended-body aircraft. From the propulsive perspective, the methodology supports the preliminary estimation of propulsive performance for all possible propulsive systems combinations and combined cycle engines that might support future reusable launchers. To this purpose, analytical formulations of thrust (or specific thrust) and specific impulse of each propulsion system are studied, required for the creation of a propulsive database. This analytical modelling is complemented by a statistical analysis of the available thrust for ramjet/scramjet engines as well as an insight on the ramjet inlet sizing.

Following the aero-propulsive characterization, a revision of the Matching Chart is pur-

sued to extend its applicability beyond the aeronautical sector, including access to space missions. For this purpose, the Multiple Matching Charts tool approach is upgraded adding a new requirement representing the minimum thrust-weight ratio as a function of wing loading necessary to reach the desired orbit. Moreover, the geometrical and aero-propulsive characterization pave the way to nominal and out-of-nominal mission analysis. In this case, the commercial software ASTOS is used.

Finally, this thesis shows the application of the developed methodology to the Skylon vehicle, a reusable single-stage-to-orbit spaceplane developed by the British company Reaction Engines Limited (Reaction). The Skylon exploits the SABRE engine technology, a combined-cycle engine able to cover the entire mission of the vehicle by exploiting liquid hydrogen as propellant.

Contents

List of Figures

List of Tables

Acronyms

BPR By-Pass Ratio. 51, 52

ESA European Space Agency. 21, 87

GUI Graphic User Interface. 21

HTOL Horizontal Take-Off and Landing. 13, 17–20, 24, 38, 72

LACE Liquid Air Cycle Engines. 61, 63

LEO Low Earth Orbit. 17–19, 21, 58, 63

MC Matching Chart. 23, 71–74, 76, 86, 87

MMC Multiple Matching Charts. 7, 21, 22, 71–73, 75, 77, 86, 92

NASA National Aeronautics and Space Administration. 71

RBCC Rocket-Based Combined Cycle. 7, 63, 64, 66, 67

RLV Reusable Launch Vehicles. 13

ROC Rate Of Climb. 72, 75, 83

SABRE Synergetic Air-Breathing Rocket Engine. 19, 24–27, 65, 80, 81

SCV Supersonic Cruise Vehicles. 33

SSTO Single-Stage-To-Orbit. 7, 11, 13–15, 17–25, 47, 48, 58–63, 65, 68, 72, 86

TBCC Turbine-Based Combined Cycle. 7, 62, 65, 66

VLEO Very Low Earth Orbit. 48, 61

Chapter 1

Introduction

In this chapter is described the current way it can be possible to access to space, discussing the actual and under development technologies that make it possible. Particular attention is given to the concept of Single-Stage-To-Orbit (SSTO), that is of particular interest in the current access-to-space scenario and the study object of this thesis. The objectives of this thesis work are then discussed, followed by a description of the structure of this document.

1.1 Research Context

1.1.1 Access-to-Space Current Scenario

In contemporary times, the space industry holds significant importance and is experiencing a period of robust growth. While the public sector is increasingly inclined to invest in this field, there is a rising number of private companies and startups actively involved in space programs. This has led to the emergence of the so-called "New Space Economy" (or "Space 2.0") which is primarily driven by commercial motivations. This shift is driven by a desire to reduce costs and accelerate innovation. In Figure 1.1, the dominance of the commercial sector in the Space Economy (on the left) and its growth prospects in the following years (on the right) can be seen.

Emerging space technology and a plethora of innovative space applications are experiencing unprecedented growth and market dynamics. Only the fields of computer science and artificial intelligence (AI) – often referred to as cyber-industries – exhibit a similar trend of rapid technological advancement and industrial upheaval. New entities like SpaceX, Blue Origin, Virgin Galactic, Kymeta, OneWeb, and Planet are revolutionizing the commercial space sector. Consequently, longstanding players in the space industry, such as Lockheed Martin, Boeing, Airbus, Northrop Grumman, and MacDonald-Detwiler, are transforming to stay abreast of the commercial space revolution [21]. A recent study revealed that over 80 space companies have been established since 2000 in the domain of Space 2.0. Indeed, several of these emerging firms have grown into significant operations and are poised to become billion-dollar enterprises [22]. One major driver of innovation is the Small Satellite Revolution. Small satellites (Smallsats) are significantly cheaper and faster to develop and launch with respect to traditional satellites.

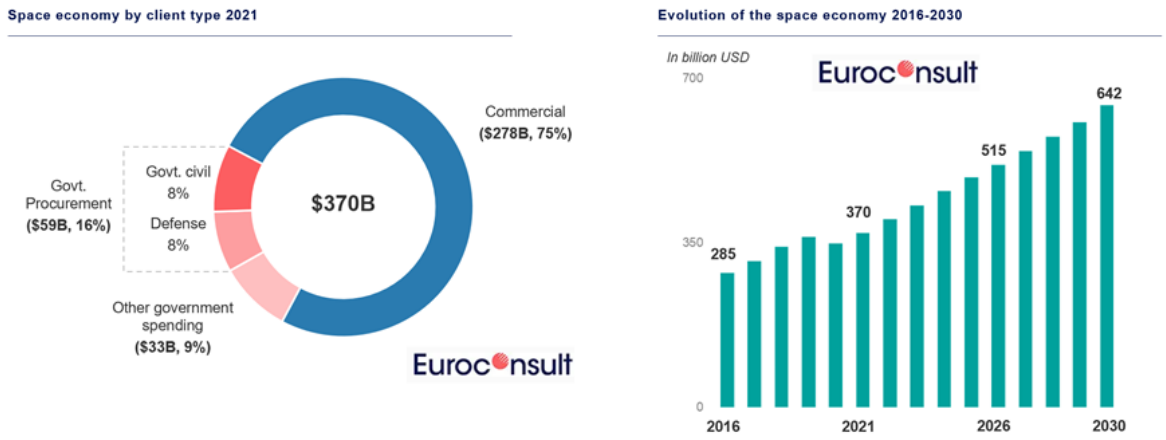

Figure 1.1: Space economy analysis (source: Euroconsult, 2021)

Their lower cost allows for constellations deployment, offering greater data collection and broader applications like Earth observation and internet access in remote areas [21].

According to "The Space Report 2023: Quarter 4" edited by Space Foundation, global launch attempts reached record highs for a third consecutive year, with 223 attempts and a high success rate with 212 successful launches. Commercial launches surged by 50% compared to 2022. The US significantly increased launches (33%), with China, India, and Japan also experiencing growth. Furthermore, more than 2800 satellites deployed into orbit, 23% more than in 2022.

For Europe, access to space is strategically vital, as it enables the deployment of space infrastructures such as Galileo, Copernicus, and EGNOS. These infrastructures, essential for our society, bolster the economy and enhance security. Additionally, future initiatives like Secure Connectivity further underscore the significance of maintaining robust access to space [1]. Upcoming projects encompass constellations comprising thousands of satellites, reusable launchers, space tourism (including suborbital flights, space flights, and space hotels), as well as more ambitious ventures such as Moon bases, Mars colonization, Earth-to-Earth high-speed transportation, asteroid mining, and space-based solar power initiatives [23].

The growing interest in space access and the resulting investments have led to a significant increase in launches. However, the price for accessing space is still very high, mainly because most launchers are either expendable or only partially reusable. Moreover, this also leads to an increase in space debris, as well as a rise in greenhouse gas emissions from traditional rocket engines. To address these growing issues, current methods of space access need to be changed and a paradigm-shift towards more reusable and sustainable assets is required. It is in this context that fully reusable launchers are catching on, currently a subject of intense research and development by both government agencies and private companies. These launchers incorporate advanced propulsion technologies that combine different engines and are capable of drastically reducing costs and environmental impact for access to space.

[1] source: Horizon Europe

1.1.2 Reusable Single-Stage-To-Orbit Vehicles

The increasing demand for space access and, consequently, launch vehicles, cannot be further met by current rocket launchers due to their environmental impact and economic unsustainability. Nowadays, many types of launch vehicles are "expendable", meaning they can only be used once, and the user bears the cost of the entire vehicle. Despite some companies, such as SpaceX, having developed partially reusable rockets, the upper stages must still be disposed of (except for the under-development Starship). Additionally, to notably minimize the economic impact of recovering and refurbishing lower stages, they need to be utilized for multiple launches. This situation requires careful evaluation to ensure safety is not compromised [24]. An alternative solution is essential, with the most appealing option being the development of a fully reusable SSTO vehicle, study object of this thesis.

Fully reusable SSTO vehicles are part of a broader category of Reusable Launch Vehicles (RLV), characterised by the fact that all parts of the launcher can be recovered and reused. Moreover, unlike conventional launch vehicles, where the first and last flight is solely for payload delivery, reusable launch vehicles can undergo flight testing before being deployed into service, thereby enhancing safety. This innovative utilization concept for launch vehicles offers numerous advantages that may outweigh the requirements of reusable launchers, such as additional systems, landing gear, or propellant for return and landing, which can result in increased overall vehicle weight.
The idea of RLVs originated in the 1950s, but technological limitations hindered progress until recently [25]. Developing fully reusable vehicles seems to be expensive compared to existing conventional launch vehicles or partially reusable options. However, RLVs hold the potential to cater to the growing demands of the space industry. This type of vehicles can be a single-stage or two-stage design for achieving orbit. Another aspect is the propulsion strategy chosen, which may involve utilizing airbreathing engines during the initial ascent stages and transitioning to rocket propulsion as the atmosphere thins, or relying solely on rocket propulsion throughout. Furthermore, the method of takeoff and landing can vary between horizontal, resembling conventional aircraft, and vertical. The selection of the takeoff mode often depends on the propulsion concept chosen, as the thrust requirements vary significantly between horizontal and vertical takeoff configurations, rather than being a predetermined decision.

This thesis focuses on SSTO designs, which offer potentially lower long-term costs compared to two-stage alternatives, due to the elimination of complex multi-stage systems and associated hardware, streamlining recovery processes and potentially lower transportation costs. This is despite the engineering challenges associated with single-stage vehicles. The idea for a fully reusable SSTO is influenced by lessons learned from partially reusable, multi-stage vehicles, like the Space Shuttle (STS). The high costs associated with the STS and its infrastructure highlight the potential advantages of a simpler SSTO design. Furthermore, this type of vehicle allows Horizontal Take-Off and Landing (HTOL) procedures, with the benefits of a reduced engine mass and a highly increased operational flexibility. This makes them ideally suited to meet the increasing demand for cost-effective and regular commercial space launches. Indeed, their potential for rapid reuse, including launches from any accessible airport, could

help bridge the substantial disparities in flight frequency and operational lifespan between a space launcher and an airliner. It is important to emphasise that this type of spaceplane has some challenging aspects: the entire empty weight of the vehicle must reach orbit, resulting in a very low payload fraction. Research is ongoing to develop high-performance engines that minimize fuel consumption during ascent, for which the integration of the airframe and engine efficiently is crucial.

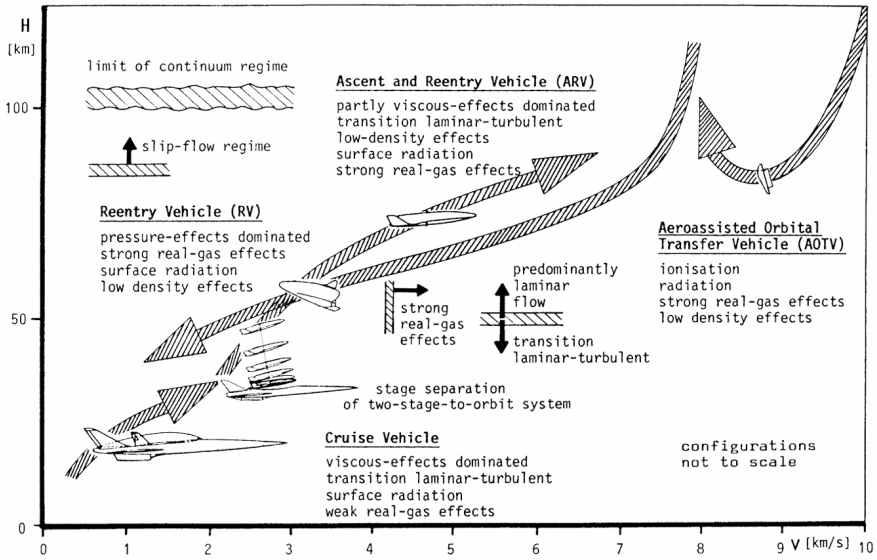

Figure 1.2: The four major classes of hypersonic vehicles [1]

Accordingly to [1], a reusable Single-Stage-To-Orbit spacecraft is categorized under the "Ascent and Re-entry Vehicles" classification within the Space Access Hypersonic Vehicles framework. Other categories within this domain include:

- Re-entry Vehicle (RV), divided in:
  a. Re-entry Vehicle Winged (RV-W): these vehicles re-enter Earth's atmosphere with controlled gliding maneuvers; they are designed to withstand high temperatures during re-entry while offering aircraft-like maneuverability within the atmosphere (example: Space Shuttle, see figure 1.3a).
  b. Re-entry Vehicle Non-Winged (RV-NW): these vehicles perform ballistic re-entry with limited controllability, their design prioritizes drag for deceleration, often resulting in blunt shapes (example: Soyuz capsule, see figure 1.3b).

- Cruise and Acceleration Vehicles (CAV): these aircraft-like vehicles operate at high altitudes and hypersonic speeds, with high aerodynamic efficiency during the cruise; they are not intended for reaching space but for point-to-point travel (similar to airplanes) or as the first stage in a two-stage launch system (examples: LAPCAT A2 (concept), see figure 1.4).

(a) RV-W: Space Shuttle

(b) RV-NW: Soyuz capsule

Figure 1.3: Re-entry Vehicles

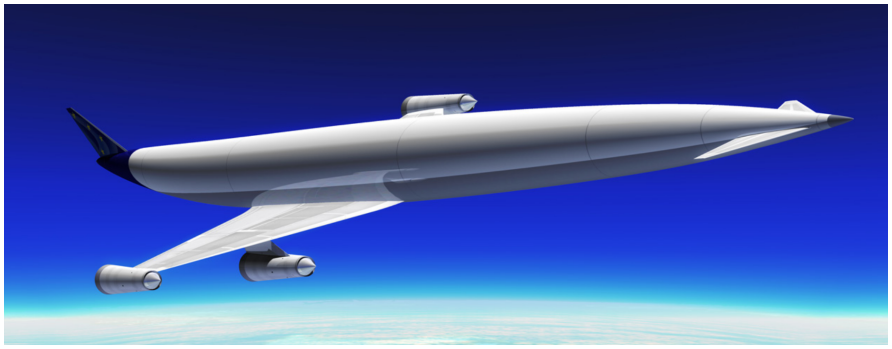

Figure 1.4: CAV: Reaction Engine LAPCAT A2

- Aero-Assisted Orbital Transfer Vehicles (AOTV): These vehicles use deployable heat shields for atmospheric drag during re-entry from space or high orbits, designed as wide-angle cones to reduce heat buildup on edges.

SSTO Vehicles Overview

Starting from the beginning of the idea of spaceplane, here is presented the historical background of SSTO vehicles. In 1931 Robert Goddard proposes a "stratosphere plane" concept, an early spaceplane design with combined air-breathing and rocket engines. This was one of the first spaceplane concepts ever made [26]. The spaceplane concept remained fictional until 1957, when the US Air Force launches the Aerospaceplane program aiming for a single-stage-to-orbit spaceplane. In 1959, the program develops the Recoverable Orbital Launch System (ROLS), a SSTO design with horizontal takeoff and air-breathing engines that collect oxygen from the atmosphere during flight. In 1963, the program terminated due to technical uncertainties and funding cuts.

Follow a description of the principal historical spaceplane's concepts:

(a) Star Raker artist's concept

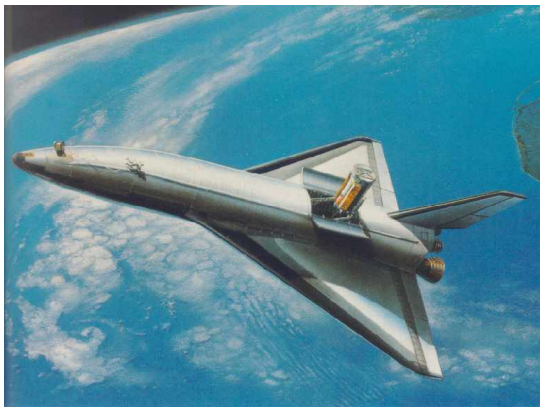

(b) Boeing RASV 2 artist's concept

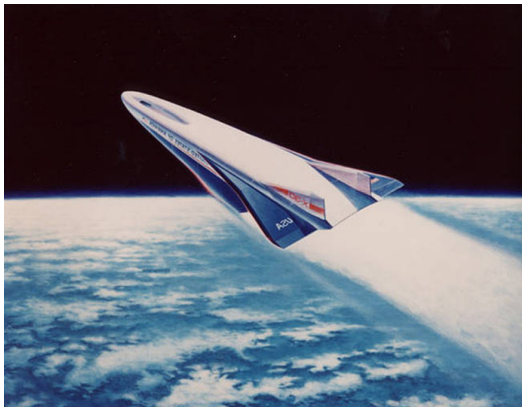

(c) X-30 artist's concept

(d) Tu-2000 artist's concept

(e) HOTOL artist's concept

(f) Japanese NAL artist's concept

Figure 1.5: SSTO historical vehicles

1. **Star-Raker:** It is a conceptual design vehicle for a Single-Stage-To-Orbit with Horizontal Take-Off and Landing, developed by North American Rockwell in the late 1970s. It was designed to meet the demanding launch requirements for a Satellite Power System (SPS) project, requiring frequent deliveries of heavy payloads (35,000 metric tons annually) to Low Earth Orbit (LEO). In table 1.1 the main features of the Star-Raker are reported. The Star-Traker propulsion system included a complex combination of en-

Fully reusable with rapid turnaround capability	
Horizontal takeoff and landing from airfields	
W_{pay}	= 89'176 kg to 556 km LEO orbit at 28.5°
GTOW	= 2'267'961 kg

Table 1.1: Star-Raker's Features

gines: ten hydrogen-powered turbofan/turbo-air exchange/ramjet engines for airbreathing propulsion, and three hydrogen-powered rocket engines for high-altitude thrust. This spaceplane challenged insurmountable limitations like the feasibility of achieving the required performance metrics (especially payload capacity and turnaround time) with 1970s technology.
An artistic representation is shown in figure 1.5a.

2. **Boeing/Langley SSTO:** Designed by Boeing in 1977, this NASA-funded study aimed to assess the feasibility of a fully reusable SSTO HTOL launch vehicle using airbreathing propulsion technology [27]. It was planned to deliver a 30'000 kg payload to a specific LEO orbit with a payload bay similar in size to the Space Shuttle, having a gross takeoff weight (GTOW) estimated at 1250 tons, with only 14% remaining as landing weight. This spaceplane either utilizes in-flight propellant transfer or a rocket sled for horizontal takeoff to reduce landing gear weight and to achieve an optimal thrust-to-weight ratio (0.7) lower than required for vertical takeoff (typically 1.3). The propulsion system was likely based on modified Space Shuttle main engines. An artistic representation is shown in figure 1.5b.

3. **NASP X-30:** The National Aerospace Plane (NASP) X-30 was a great ambitious project, aimed to be a revolutionary leap forward from the Space Shuttle. It was designed as both a SSTO vehicle and a point-to-point travel vehicle like a hypersonic airplane. The X-30 vehicle design relied on several unproven assumptions and overly optimistic interpretations of data, omitting crucial elements for a functional vehicle (e.g., landing gear). Due to the technological immaturity of the era (1980s) and the beginning of the Cold War, the program was cancelled in 1992. Despite not reaching its ambitious goals, the NASP program has contributed to advancements in high-temperature resistant materials for the vehicle's body and in materials for cryogenic fuel tanks that can withstand very low temperatures [28]. An artistic representation is shown in figure 1.5c.

4. **Tupolev Tu-2000:** The Tupolev Tu-2000 project began in 1986 as the Soviet Union's

response to the US hypersonic spaceplane, the X-30. Three versions were planned: a Mach 6 test vehicle, which was under construction at the cancellation of the program, a Mach 6 intercontinental bomber, and a SSTO launch vehicle. It was designed to have a take-off weight of 260'000 kg, with a payload capacity of 8'000-10'000 kg to a 200 km Low Earth Orbit. The propulsion system was characterized of eight turboramjet engines for airbreathing during atmospheric flight, and a rocket engine for achieving orbital velocity. The fall of the Soviet Union led to funding issues and the project was suspended in 1992 due to financial constraints. An artistic representation is shown in figure 1.5d.

5. **HOTOL:** The HOTOL program was a British Aerospace (BAe) and Rolls Royce initiative in the early 1980s for a SSTO vehicle with Horizontal Take-Off and Landing, stemmed from research on pre-cooled jet engines by British engineer Alan Bond. Designed for carry 7 tons of payload to LEO orbit (or lighter payloads to geostationary orbit with an additional perigee engine) with a GTOW of 275 tons, the HOTOL had an air-breathing mode using the unique RB545 ("Swallow") engine with liquid hydrogen/liquid oxygen propellant until reaching 26-32 km altitude. Then, at Mach 5-6, a transition to rocket was performed for orbital insertion. A rocket-sled-assisted launch was necessary to reach the initial speed, and a moderate re-entry profile was designed to reduce thermal stress. British government funding was withdrawn in 1989 due to budget constraints, followed by the program suspension and engine design classified as top secret, hindering potential private investment. An artistic representation is shown in figure 1.5e.

6. **Japanese Spaceplane NAL:** Japan's National Aerospace Laboratory's (NAL) concept for a SSTO spaceplane was designed around the same time as the US NASP project. With a 20 tons of payload capacity out of 350 tons of GTOW, this spaceplane was designed to reach an orbit altitude of 570 km [29]. Three designs were developed: Mitsubishi, Fujl, and Kawasaki, which have slightly different dimensions, such as vehicle length and wingspan. From a propulsion point of view, a combination of scramjet for airbreathing and a rocket engine for space travel was proposed, with liquid hydrogen and liquid oxygen as propellants. A launch of a prototype was proposed in 2006, but there is no information on whether the project progressed further. It's likely the project was cancelled, as there are no reports of a successful NAL spaceplane prototype. An artistic representation is shown in figure 1.5f.

Next are presented the ongoing projects for Single-Stage-To-Orbit configurations. It's possible that some of these projects are currently on hold or significantly delayed compared to the planned schedules.

AVATAR

AVATAR or Avtar, which stands for 'Aerobic Vehicle for Advanced Trans-Atmospheric Research', was first announced in May 1998, as a reusable launch vehicle with military applications. This India's spaceplane project was a smaller and more practical version of a previously

cancelled project, the 230-ton Hyperplane, and was publicly announced in the US in July 2001 [30].

AVATAR's takeoff weight is around 25 tons, comparable to an advanced fighter jet. This is claimed to be the smallest feasible weight for a reusable SSTO spaceplane capable of delivering 1 ton of payload to orbit. A small-scale flight demonstrator is also being designed. It operates with horizontal takeoff and landing (HTOL) like a conventional airplane, and use a combination of engines: a turbofan for initial takeoff, a ramjet for sustained hypersonic flight, a scramjet for even higher speeds, and a cryogenic rocket engine for final push into orbit. Around 60% of takeoff weight is liquid hydrogen (fuel), while oxygen (oxidizer) is collected from the atmosphere during hypersonic flight and liquefied onboard, eliminating the need for massive oxygen storage at takeoff. This self-refueling process nearly doubles the mass of the spaceplane during flight.

Overall, the AVATAR project aimed for a cost-effective and reusable space launch platform with military applications. However, there is no information available on the project's current status or if it achieved its goals.

Figure 1.6: AVATAR hyperplane model representation (credits: ISRO)

SKYLON

SKYLON is a SSTO reusable launch vehicle developed by Reaction Engines Ltd. in the UK, a company founded in 1989 by private investors and operating from Culham Science Park since 2000. It was founded to revive the HOTOL project and leverage its knowledge base.

SKYLON is designed to be fully reusable with Horizontal Take-Off and Landing characteristics like a conventional aircraft. It mounts two Synergetic Air-Breathing Rocket Engine (SABRE), highly complex engines mounted on wingtips in nacelles that function as both air-breathing jet engines in the atmosphere and rocket engines in space.

Starting from the HOTOL's 275-ton takeoff weight, the SKYLON project initial configuration (C1) was designed to have a 12-ton payload capacity to LEO orbit. A second configuration (C2) was a scaled-up version with a 345-ton takeoff weight to meet higher payload demands (15 tons). Finally, the actual configuration was established in 2010 after further technological

advancements and engine cycle studies.

Overall, the SKYLON project aimed to create a cost-effective and reusable space launch vehicle by leveraging the learnings from HOTOL and focusing on innovative engine technology. A deeper description of this spaceplane is reported in chapter 2, as a presentation of the case study of this thesis.

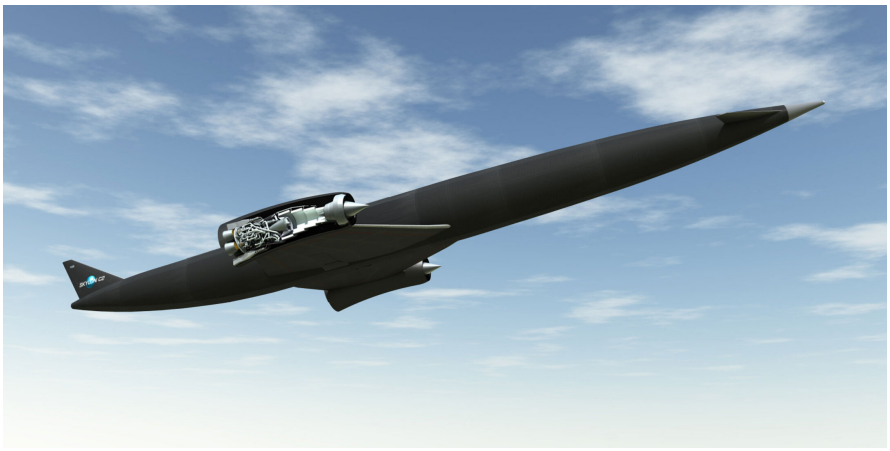

Figure 1.7: SKYLON spaceplane model representation (credits: Reaction Engines Ltd.)

Radian One

The Radian One is a Single-Stage-To-Orbit spaceplane under development by Radian Aerospace, a company founded in 2016 and based in Bellevue, Washington. It had secured $27.5 million in funding in January 2022 for the Radian One project [31].

Figure 1.8: Radian One spaceplane model representation (credits: Radian Aerospace.)

This spaceplane is a fully reusable HTOL vehicle, designer to be manned by a crew of five

people with an addition cargo capacity of 5000 lbs (2268 kg) to orbit. It has an expected return cargo capacity of 10'000 lbs (4,536 kg) and can deliver cargo anywhere on Earth in under an hour.

Radian One features an aircraft-like configuration requiring minimal launch infrastructure with a 48-hour turnaround time between missions. It performs a subsonic takeoff from a runway using a rocket-powered sled with full fuel tanks. Then, a low-gravity ascent is projected to Low Earth Orbit (LEO) for crew comfort. The orbit access is made by a propulsion system composed by three liquid-fueled rocket engines for orbital insertion, advanced cryogenic-fueled engines with a thrust of 200'000 lbs (90'718 kg) at full power. The winged configuration allows for smooth landing on any 10000 ft (3048 m) runway.

1.2 Conceptual Design methodology and tools

The increasingly larger request of access to space, driven by the constant growth of the space economy, leads to the request of new tools, strongly desired by space agencies as European Space Agency (ESA), capable of accelerate the mission design. In this context, a research project of Politecnico di Torino is aimed to develop a tool which purpose is assisting users in rapid and reliable conceptual design of reusable access-to-space vehicles. The aim of this tool will be to support students, researchers and engineers in the very first design phases of this type of mission, enabling the user to move from an initial hypothetical or statistical evaluation of design parameters to an accurate geometric and propulsive characterisation of the vehicle.

Through a Graphic User Interface (GUI), the user can define the mission requirements that the project vehicle must meet, input constraints, and make assumptions regarding mission performance. Subsequently, the user can select the vehicle configuration and propulsion strategy. At this point, the software is capable of sizing the vehicle through a dedicated sizing methodology.
The sizing code adopts an iterative process that, in the case of a feasible mission, converges the hypothetical variables to convergence values. In contrast, if the mission is infeasible, the code diverges, and the user is alerted to the mission's non-feasibility. In this analysis, the aircraft is treated as a unified system, given the interdependence of structural configuration, aerodynamics, and propulsion. The sizing methodology provides convergent mass and volume values for the system. With these values, using Multiple Matching Charts (MMC) tool, it is verified that the available thrust exceeds the required thrust, and the design planform area of the aircraft is determined.

The figure 1.9 shows the organisation chart of the project, i.e. how the development work of the conceptual design tool is coordinated.

1.2.1 Thesis Objectives

The work of this master's thesis focuses on the conceptual design of the **ascent phase**, a crucial and technically demanding stage for Single-Stage-To-Orbit vehicle missions from both aerodynamic and propulsion perspectives. During the ascent into orbit, the spaceplane is sub-

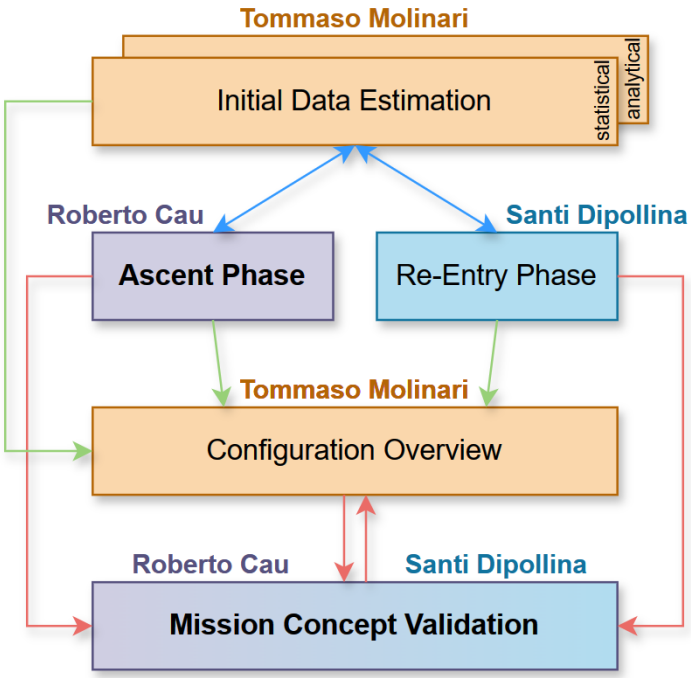

Figure 1.9: Organisation chart of the methodology and tools development, where this thesis's work is highlighted in bold

jected to continuous variations in environmental conditions such as density, temperature, and pressure, which interfere with aerodynamics, thermodynamics, and propulsion management, necessitating the aircraft's adaptation to complete the mission. For these reasons, the ascent phase requires a comprehensive study of the configuration and materials used, as well as the use of propulsion systems capable of changing operational modes. The first objective of this thesis is to study the aerodynamic and propulsion models to be incorporated into the tool's sizing code. These models are required to have relatively simple analytical treatments suitable for the aerodynamic and propulsion characterization of reusable SSTO access-to-space vehicles. To adequately verify the required thrust and design planform area, a new analytical formulation (Thrust-to-Weight ratio as a function of Wing Loading) of the orbit attainment requirement was studied for incorporation into the Multiple Matching Charts. The final objective of this work was to verify the methodology developed for the conceptual design of the ascent phase by conducting a mission simulation using the commercial software ASTOS, utilizing the outputs of the developed sizing code as input of the mission analysis.

1.3 Document Outline

The contents of this thesis are outlined below:

- In *Chapter 2* is briefly described the case study of this thesis: the SKYLON spaceplane; a general description of this characteristics and performances is reported, including a

review of the SABRE engine.
Bibliography: [2], [3], [4]

- In *Chapter 3* is reported the description of the most suitable aerodynamic models for the conceptual design of ascent phase, followed by a discussion about their applicability in the tool.
  Bibliography: [9], [5], [6], [32], [7], [33], [34], [35]

- In *Chapter 4* is presented the preliminary estimation of propulsive performance for all possible propulsive systems combinations and combined cycle engines that might support future reusable SSTO launchers.
  Bibliography: [14], [8], [9], [10], [12], [11], [13], [14], [15], [36], [37], [38], [24], [16], [39], [40], [17], [18], [41], [19]

- In *Chapter 5* a revision of the Matching Chart tool is made to extend its applicability at access to space missions; Multiple Matching Charts approach is used to include the reaching of the target orbit requirement through the development of a new formulation of the thrust-to-weight ratio as a function of the wing load.
  Bibliography: [42], [5], [43]

- In *Chapter 6* a mission analysis conducted using the commercial software ASTOS aimed to verify the developed conceptual design methodology is presented. In this context, the ascent phase of the sized SKYLON is simulated through the sizing code created.
  Bibliography: [2], [20], [3]

- In *Chapter 7* conclusion, limitations of the work and possible future implementations are analyzed.

Chapter 2

Case of study: SKYLON

2.1 SKYLON Concept

This chapter briefly presents SKYLON, the case study to which the developed methodology has been applied. SKYLON is a SSTO spaceplane fully reusable, currently under development by the British company Reaction Engines Limited (Reaction) since 2009. The SKYLON exploits the SABRE engine technology, a combined-cycle engine able to cover the entire mission of the vehicle by exploiting liquid hydrogen as propellant.

The SKYLON spaceplane possesses the capability to take-off and land on a runway like a conventional aircraft, thus belonging to the category of Horizontal Take-Off and Landing vehicles. This aspect constitutes a significant advantage in its operational management; for instance, it can be prepared for departure in a hangar near the runway, thereby avoiding the complex and expensive transportation challenges associated with launch facilities.
From the configuration perspective, as can be seen in figure 2.1, the payload bay of this vehicle is positioned at the wing attachment point, and the payload is loaded from above. In contrast to designs of other SSTO spaceplanes, SKYLON features a distinct separation between the slender fuselage and the delta wing (positioned approximately halfway up the fuselage), that has been demonstrated to be optimal in terms of weight, lift, and volume. However, this characteristic poses challenges in the management of heat flows, as it gives rise to localized high heat fluxes that necessitate an active cooling system. The axial symmetric nacelles, on which the SABRE engines are mounted, are positioned on the wingtips.
The dimensional and mass characteristics of the SKYLON are reported in table 2.1 [2]. The

Fuselage Length	83.1 m
Wing Span	26.8 m
Height	13.5 m
Max Payload Weight	15.0 tons
Dry Weight	53.4 tons
Gross Weight	325.0 tons

Table 2.1: Dimensional and weight characteristics of the SKYLON spaceplane

majority of the fuselage is dedicated to housing the hydrogen cryogenic tanks, with a smaller portion reserved for the liquid oxygen tanks. This allocation is facilitated by the fact that, during the initial phase of ascent, the oxidizer is sourced from the outside air, in addition to the low density of hydrogen that leads to larger fuel tanks. The placement of the tanks is associated with equilibrium problems that impact the vehicle. These challenges were resolved through meticulous aerodynamic design and the implementation of differential burning of the propellant in the two tanks.
The SKYLON is equipped with control surfaces for atmospheric flight, including Canard foreplanes for pitch control, ailerons for roll control, and an aft fin for yaw control. During the pure rocket phase, control is achieved through differential engine thrust. Additionally, it features a SOMA (SKYLON Orbital Maneuvering Assembly) module with engines designed for orbital manoeuvres.
Regarding the materials, the primary structure consists of a frame composed of titanium struts reinforced with silicon carbide, while the aluminium tanks are suspended using Kevlar ties. The frame is further covered with sheets of reinforced glass ceramic material, serving as both the aeroshell and the primary thermal protection system, supplemented by a multilayer metallic heat shield.

2.2 SABRE Engine

The Synergetic Air-Breathing Rocket Engine (SABRE) is the key component of the SKYLON, enabling the Single-Stage-To-Orbit vehicle to operate in both air-breathing and rocket modes. This unique engine concept operates like a turbojet, utilizing hydrogen as fuel in combination with air from take-off until the transition point, set at an altitude of 25 km, enabling the

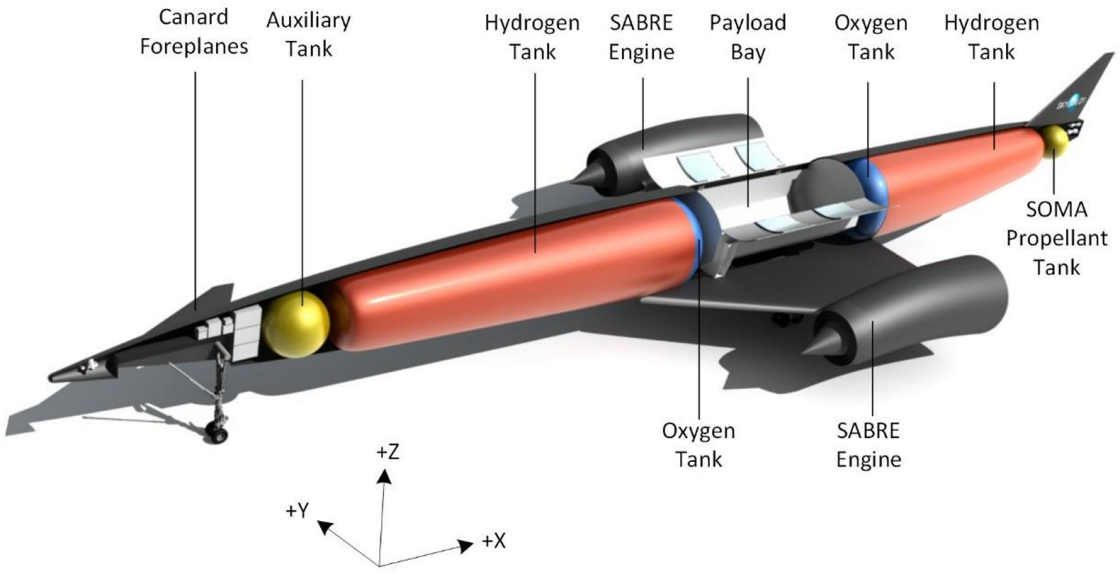

Figure 2.1: SKYLON layout [2]

engine to reach a Mach number of 5. Once this speed regime is reached, the engine transitions to rocket mode, during which air is replaced by liquid oxygen (LOx), ensuring a specific energy release during combustion compatible with the levels required for ascent to low Earth orbit. The transition of the SABRE to rocket mode occurs at an altitude where it is no longer feasible to sustain LH2-air external combustion due to the rarefied conditions of the atmosphere at that altitude. However, the advantages of this innovative engine design are significant, as the air-breathing operating mode allows for a reduction in the amount of propellant needed to be stored inside the SKYLON to ensure access to the target orbit, consequently increasing the payload mass that can be transported to its destination. The architecture of the SABRE is well summarized by the figure 2.2 provided by [3].

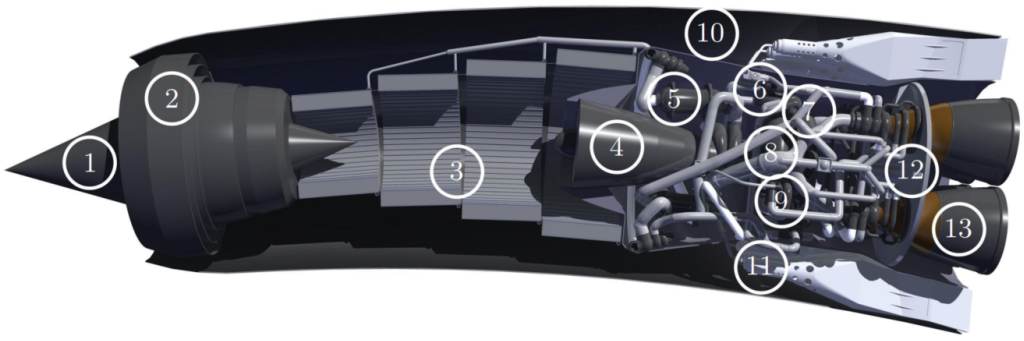

Figure 2.2: SABRE section: *1) movable spike 2) intake 3) precooler 4) air compressor 5) preburner and reheater 6) helium circulator 7) H2 pump 8) He turbine and regenerator 9) LOx pump 10) spill duct 11) ramjet burners 12) heat shield 13) thrust chamber (CC)* [3]

Regarding its air-breathing operating mode, the SABRE falls into the category of deeply precooled combined cycle engines, where the primary air cycle is coupled with a secondary regenerative cycle using helium for thermal management of the engine. In figure 2.3 is reported a scheme of cycle.

This solution allows for the regeneration of a portion of the heat extracted from the hot incoming airflow into the engine, extending its operation in air-breathing mode up to a Mach regime exceeding 5 without performance degradation, particularly in specific impulse. Additionally, the SABRE involves a two-stage combustion process occurring in two different combustion chambers: the PreBurner (PB) and the main combustion chamber (CC), enabling the regeneration of a portion of the heat produced during the initial combustion segment, again utilizing the helium cycle. The regenerated heat through the helium cycle is utilized to heat the cold flow of hydrogen stored at a temperature close to 0 K to maintain its liquid state during storage, as well as to power the compressor involved in the primary air cycle.
As reported by V. F. Villàcé [3], the incoming air captured by the intake is deeply cooled by a flow of cold helium inside the precooler (PC), then passes through the high-pressure ratio air compressor (AC), downstream of which the flow is split with a variable splitting ratio depending on the flight Mach number and redirected to the two combustion chambers. The two-stage combustion takes place first in the PB, where a portion of the air is burned under

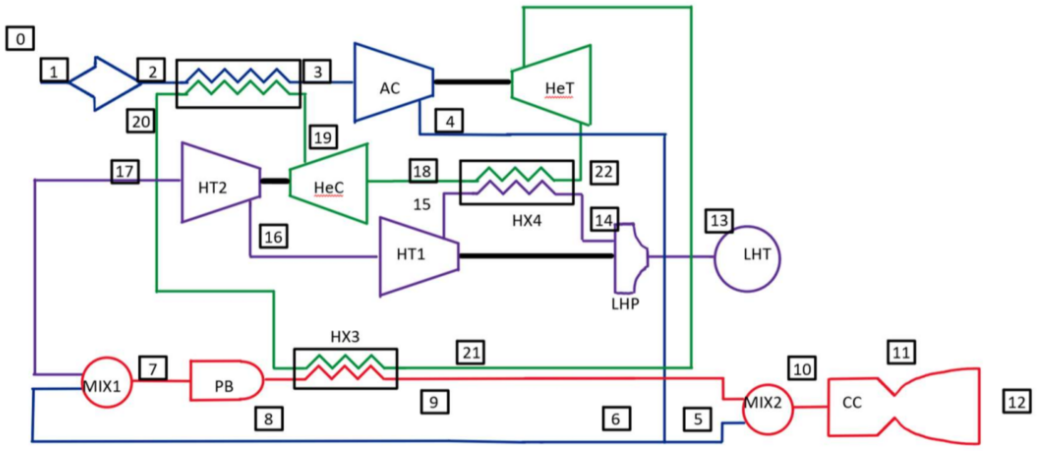

Figure 2.3: Cycle scheme of the complete model [4]

fuel-rich conditions. The exhaust gases from the PB, after exchanging some of their heat in a heat exchanger with helium, rejoin with the second airflow from the splitting at the main CC, where combustion is completed again under fuel-rich conditions. Finally, the combustion products from the main CC then expand in the nozzle, generating thrust. Additionally, bypass burners are provided for a portion of the incoming airflow at the intake, optimizing engine performance and efficiency. Regarding the engine's operation in rocket mode, the engine cycles are shorter as the air intake is closed, and the two-stage hydrogen-air combustion is replaced by a single stage of hydrogen-oxygen combustion. Oxygen in this configuration contributes to heat regeneration by cooling the nozzle walls, thereby recovering some of the heat produced during the hydrogen combustion.

As declared in the SKYLON User Manual [2], this engine can provide a gross thrust of approximately 2 MN per nacelle in both of its operating modes. In the air-breathing phase, it offers a specific impulse ranging from 40000 to 90000 m/s. However, in the rocket phase, the specific impulse value is around 4500 m/s. The architecture of the SABRE engine is indeed custom-designed for space access, offering significant advantages. It provides a high thrust-to-weight ratio during air-breathing operation, coupled with moderate specific fuel consumption, which enables efficient propulsion during the initial phase of flight. Furthermore, as it tran-

Specific Impulse Airbreathing	40'000 ÷ 90'000 m/s
Maximum Thrust Airbreathing	2 x 984 kN
Maximum Mach Airbreathing	5.5
Service Ceiling Airbreathing	28500 m
Specific Impulse Rocket	4500 m/s
Maximum Thrust Rocket	2 x 2000 kN

Table 2.2: SKYLON performances

sitions to rocket mode, it maintains a high specific impulse, ensuring optimal performance during the phase of reaching the target orbit.

Table 2.2 summarize the SKYLON performances.

Chapter 3

Aerodynamic Characterization

3.1 Aerodynamic models

In this chapter, various aerodynamic models studied for the analysis of the ascent phase of a reusable spacecraft for space access are presented. The mode of adoption, partial adoption, or rejection of these models are described. The objective is to identify relatively simple analytical formulations for the coefficients of Lift, Drag, and consequently, the aerodynamic efficiency (L/D), initially neglecting aerodynamic moment coefficients and, therefore, stability aspects (reserved for future developments).

The search for models suitable for this type of project involved a meticulous investigation of existing literature on the aerodynamic characterization of vehicles capable of achieving hypersonic speeds. Specifically, the ascent phase to the orbit of a spacecraft spans a broad spectrum of Mach numbers, ranging from $M = 0$ at Take-Off to $M = 20+$ in the final phase of ascent. To simplify the analysis, a more complex aerothermodynamic analysis, necessary at $M > 3$ due to the emergence of non-negligible thermodynamic effects [9], has not been undertaken. Heat flows affecting the thermal control system (TCS) of the spacecraft are ignored, as these become more critical during re-entry, making them conservative in the ascent phase. Furthermore, due to the lack of precise analytical formulations for aerodynamic characterization in the transonic regime ($0.8 < M < 1.2$) and its short duration, the study of this regime is neglected, and values interpolating the extremes of the transonic Mach range are considered.

Data from the aforementioned aerodynamic models can be integrated with experimental aerodynamic data derived from statistical analyses. This approach allows users to choose which data sources to rely on.

3.1.1 Curran model

The Curran aerodynamic model is presented in Chapter 16 (titled "Transatmospheric Launcher Sizing") in the book "Scramjet propulsion" edited by E.T. Curran and S.N.B. Murthy [5].

In this simplified model, the analysis of aerodynamic coefficients is correlated to a param-

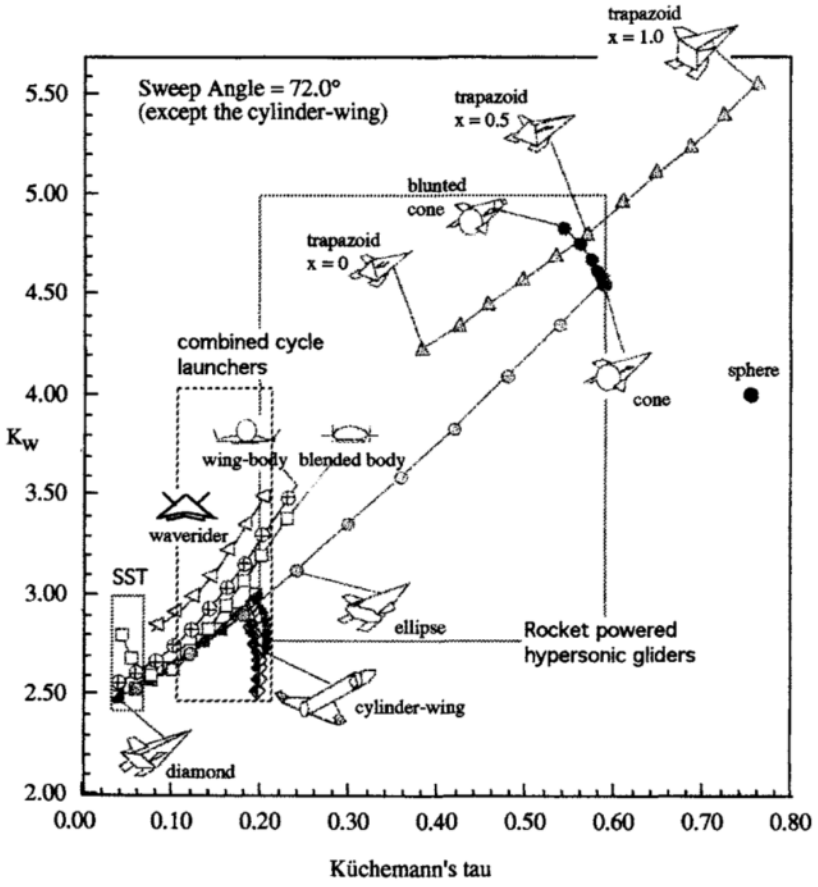

Figure 3.1: Surface and Volume Characteristics of Hypersonic Configuration Concepts [5]

eter F, which is dependent on the geometry of the aircraft and is defined as:

$$F = \sqrt{\left(\frac{V_{\text{tot}}^{0.667}}{S_{\text{pln}}}\right) \cdot \left(\frac{S_{\text{wet}}}{S_{\text{pln}}}\right)^{1.5}} = \tau^{0.333} \cdot K_W^{0.75} \tag{3.1}$$

in which appears the Küchemann parameter τ and the parameter K_w defined as follows:

$$\tau = \frac{V_{tot}}{S_{pln}^{1.5}}$$

$$K_w = \frac{S_{wet}}{S_{pln}}$$

which employs known geometric variables such as the total aircraft volume V_{tot}, the aircraft wetted surface S_{wet} and the aircraft planform area S_{pln} (also known as reference area). As it can seen in figure 3.1, the correlation between τ and K_w parameters determine the geometry configuration of the aircraft.

Having the parameter F, it is possible to determine the maximum aerodynamic efficiency

$(L/D)_{max}$ through an empirical correlation as a function of Mach number M:

$$\left(\frac{L}{D}\right)_{\max} = \frac{3.063}{M} \cdot (M+3) \cdot (1.11238 - 0.1866\dot{\theta} \cdot F) \ . \tag{3.2}$$

Also empirically bound to F is the C_{D_0}, which is found with

$$\beta C_{D_0} = 0.05772 \cdot e^{0.4076 \cdot F} \tag{3.3}$$

where $\beta = \sqrt{|M^2 - 1|}$. Hence, the Drag coefficient can be calculated:

$$C_D = C_{D_0} \cdot (1 + B) \tag{3.4}$$

where the term in brackets depends on the flight condition

- Acceleration: (1+B)=1.075
- Minimum fuel flow Cruise: (1+B)=1.75
- Max efficiency Glide: (1+B)=2

Having the Drag Coefficient and the Maximum Efficiency, it is now possible to calculate the Lift Coefficient for the three above-mentioned flight conditions:

- Acceleration: $C_L \sim 0.1 \cdot (C_L)_{L/D_{max}}$
- Minimum fuel flow Cruise: $C_L \sim 0.82 \cdot (C_L)_{L/D_{max}}$
- Max efficiency Glide: $C_L \sim (C_L)_{L/D_{max}}$

The aerodynamic model just described allows for a simplified and rapid determination of aerodynamic coefficients, requiring a minimal set of inputs. This facilitates its application to any selected aircraft configuration, for which knowledge of the two fundamental parameters, τ and K_w, is sufficient.
In this model, for a fixed configuration, the aerodynamic coefficients are solely functions of the flight Mach number, while the dependence on the angle of attack α is not considered. Consequently, the results obtained may be somewhat inaccurate and suitable primarily for an initial design iteration when very limited input data are available [35].

3.1.2 Torenbeek model

The Torenbeek aerodynamic model comes from the book "Essentials of Supersonic Commercial Aircraft Conceptual Design" by Egbert Torenbeek, Delft University of Technology [6]. This model, unlike the Curran's one, introduces the dependence of the aerodynamic coefficients on the angle of attack α, but the approach proposed in the book is only applicable for supersonic speeds.

It allows the evaluation of aerodynamic coefficients for three specific high-speed aircraft configurations: a generic one with a delta wing, a generic one with an arrow wing, and a

blended wing body configuration. The mathematical description of the Torenbeek model is given below.

Lift Coefficient

The analysis of the Lift Coefficient is centered around the delta wing configuration, as it is widely employed in supersonic aircraft due to its ability to deliver optimal aerodynamic performance both in subsonic and high Mach number flight. The flow characteristics around a flat delta wing are predominantly influenced by the leading edge flow parameter, defined as

$$m = \frac{\tan\gamma}{\tan\mu} = \beta \cot \Lambda_{le} \tag{3.5}$$

with γ denoting the complement of the leading edge sweep angle Λ_{le} and μ the Mach angle, as represented in figure 3.2. The Lift Coefficient is given by the product of the lift slope $C_{L_{alpha}}$

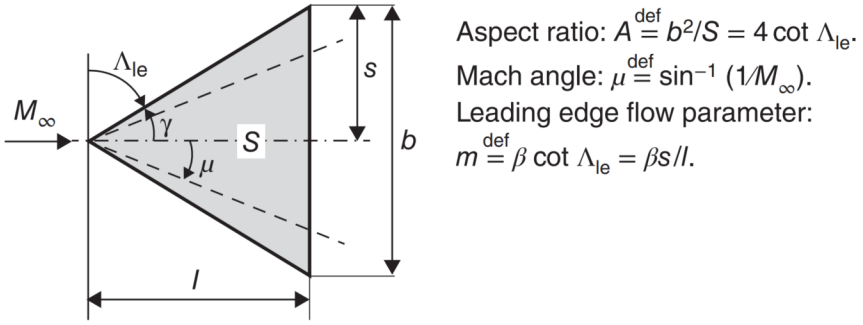

Figure 3.2: Delta wing geometry and definitions of flow parameters

and the angle of attack α, where the lift slope varies depending on whether the leading edge is supersonic[1] or subsonic[2].

$$C_L = C_{L_\alpha} \cdot \alpha \tag{3.6}$$

Supersonic Leading Edge At an incidence α to the oncoming flow, a delta wing experiences a speed of magnitude such that the component of the speed normal to the leading edge (V_n) exceeds the sonic velocity, i.e., $m > 1$. In this case, both the leading-edge and the trailing-edge are in a supersonic condition.

$$C_{L_\alpha} = \frac{4}{\sqrt{M^2 - 1}} = \frac{4}{\beta} \tag{3.7}$$

Subsonic Leading Edge When a delta wing is positioned in a lower-supersonic airflow, the Mach angle increases, causing the Mach waves originating at the wing vertex to rotate

[1] A supersonic leading edge refers to (a portion of) the leading edge where the component of the oncoming flow normal to the wing edge is supersonic ($m < 1$).

[2] A subsonic leading edge refers to (a portion of) the leading edge where the component of the oncoming flow normal to the wing edge is subsonic. ($m > 1$).

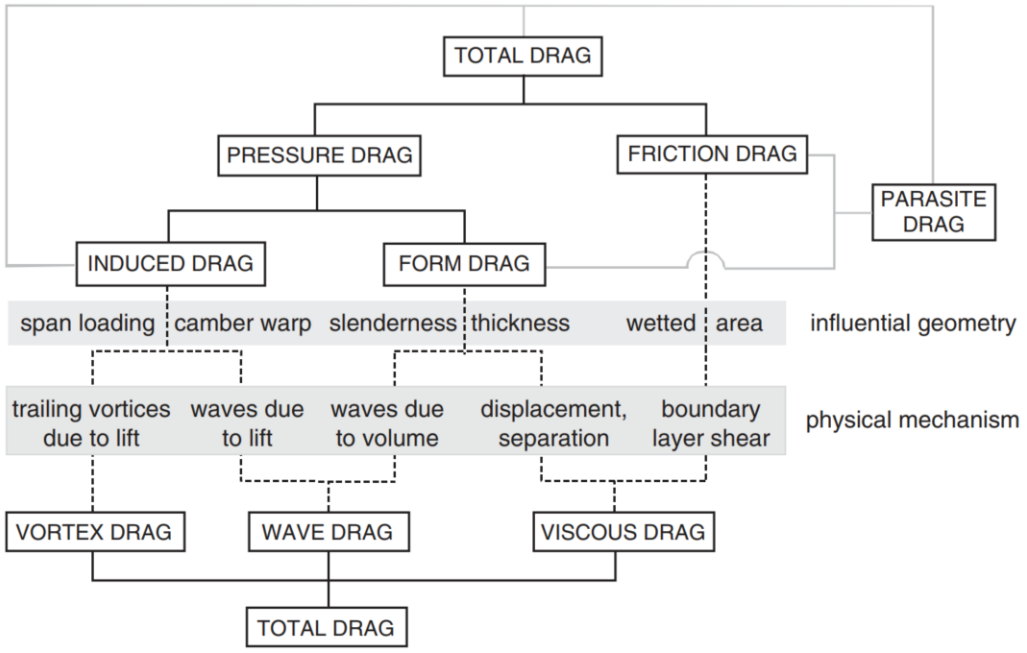

Figure 3.3: Scheme for decomposing the Drag of a supersonic flight vehicle

towards the leading edge. The velocity is sufficiently low to result in a Mach angle μ larger than the angle γ, causing the flow parameter m to become less than one. This results in a subsonic leading edge and a supersonic trailing edge and the lift slope can be derived from the slender wing theory [6].

$$C_{L_\alpha} = \frac{2\pi m}{E'(m)\beta} \tag{3.8}$$

with

$$E'(m) = 1 + (\pi/2 - 1)m^\eta \quad \text{where} \quad \eta = 1.226 + 0.15\pi(1 - \sqrt{m})$$

The same approach can be extended to the arrow wing configuration.

Drag Coefficient

The Drag Coefficient of the Torenbeek model is given by the composition of several contributions, whose complete scheme is shown in figure 3.3.

In the proposed approach, referring to the coefficients, the Total Drag of the aircraft is decomposed into a constant term C_{D_0}, given by the sum of the Skin Friction Drag C_{D_F} and the Wave Drag due to Volume $C_{D_{WV}}$, and an induced term ΔC_D (also referred to as Drag due to Lift), obtained by summing the Wave Drag due to lift $C_{D_{WL}}$ and the Vortex-Induced Drag $C_{D_{VL}}$.

$$C_D = C_{D_0} + \Delta C_D = (C_{D_\mathrm{F}} + C_{D_\mathrm{WV}}) + (C_{D_\mathrm{WL}} + C_{D_\mathrm{VL}}) \tag{3.9}$$

This relationship can be adopted in the initial design phase of a SCV, in which several minor

drag components cannot be assessed until a comprehensive understanding on the shape of the surface exposed to the flow is obtained. Below is presented the evaluation of the various contributions to Drag for the three different configurations analysed by the model.

Delta Wing configuration For this configuration reference is made to the geometry reported in figure 3.2.

- Skin Friction Drag:
  Skin Friction Drag affects both lifting and non-lifting components of flight vehicles and is commonly estimated during the conceptual design phase using the flat-plate analogy, where each component exposed to the airflow is modeled as a smooth, flat plate with the same length and surface area exposed to the flow. These plates are positioned in undisturbed flow at the same Reynolds number. The total skin friction drag area is determined by summing the drag areas of all airplane components, so the Skin Friction Drag coefficient is given by:

$$C_{D_F} = \frac{\sum (C_F \cdot K_F \cdot S_{\text{wet}})}{S_{\text{pln}}} \tag{3.10}$$

  where C_F is the friction coefficient, the factor K_F takes into account non-ideal drag resulting from imperfections like surface roughness, seams, control surface slots, and cabin entrance doors and assumes the values

$$K_F = \begin{cases} 1 & \text{Wing} \\ 1.05 & \text{Fuselage} \\ 1.15 & \text{Vertical fin and a horizontal stabilizer} \end{cases}$$

  and S_{wet} and S_{pln} are respectively the wetted surface and the reference area. The friction coefficient C_F is evaluated through the Prandtl–Schlichting formula

$$C_{\text{F}} = \frac{0.455}{r_{\text{T}}} \left(\log_{10} \text{Re} - 2.80 \log_{10} r_{\text{T}}\right)^{-2.58} \tag{3.11}$$

  where the factor r_T accounts for the kinetic heating due to stagnation of the boundary layer and depends on the Prandtl number

$$r_{\text{T}} = 1 + \mathcal{P} r^{1/3} \frac{\gamma - 1}{2} M_\infty^2 \simeq 0.71$$

- Wave Drag due to Volume:
  The Wave Drag due to Volume in a delta wing is caused by the formation of shock waves and it is directly dependent on the volume distribution. Its coefficient $C_{D_{WV}}$ is expressed as the product of the wing aspect ratio (A_w) and the square of the airfoil thickness ratio. For a slender wing, wave drag due to volume is based on the Sears–Haack body pressure

drag and can be expressed as follow:

$$C_{D_{WV}} = K_{WV}\ A_W \left(\frac{t}{c}\right)^2 \tag{3.12}$$

with the parameter K_{WV} is a function of the Sears-Haack body factor K_{SH} and can be written as

$$K_{WV} = 2.2 \cdot K_{SH} \quad \text{where} \quad K_{SH} = 1.17 \cdot \frac{1 + 1.5\beta \cdot \cot \Lambda}{1 + 4\beta \cdot \cot \Lambda}$$

In addition to the contribution of the wing, that of the fuselage must also be considered. Calling d_f the fuselage diameter, l_n the nose length and l_t the tail length, the Wave Drag due to Volume coefficient related to the fuselage is

$$C_{\mathrm{D_{WV}}_f} = \frac{1}{S_{pln}} K_\beta \frac{\pi}{4} d_{\mathrm{f}}^2 \left[(d_{\mathrm{f}}/l_{\mathrm{n}})^2 + (d_{\mathrm{f}}/l_{\mathrm{t}})^2 \right]. \tag{3.13}$$

- Wave Drag due to Lift
  This contribution is related to the fact that a wing subjected to a flow with a low angle of attack encounters lift-dependent drag attributed to shock and expansion waves. The Wave Drag due to Lift coefficient is obtained through the equation

$$C_{D_{WL}} = K_{WL} \cdot \frac{\beta^2\ C_L^2\ AR}{8\pi} \tag{3.14}$$

  where $K_{WL} \simeq 1.15$ in a realistic early design assumption. It naturally depends on the Lift Coefficient, but also on the aspect ratio AR and on the Mach number through β.

- Vortex-Induced Drag:
  Vortex Induced Drag is generated by the circulation around the airfoil, which creates vortices in the airflow trailing behind the wing. The minimum vortex-induced drag coefficient for a planar wing in subsonic flow is established by Munk's classical solution. The optimal condition corresponds to an elliptical lift distribution along the wing span. According to linearized theory, the induced drag of a delta wing is given by:

$$C_{D_{\mathrm{VL}}} = K_{\mathrm{VL}} \frac{C_L^2}{\pi A_{\mathrm{w}}} \tag{3.15}$$

  where the term K_{VL} accommodates the deviation from the minimum vortex-induced drag and in a early design stage can be assumed as $K_{VL} = K_{WL} \simeq 1.15$.

Arrow Wing configuration The reference geometry of the arrow wing configuration is presented in figure 3.4. The analysis of this configuration can be made starting from the delta

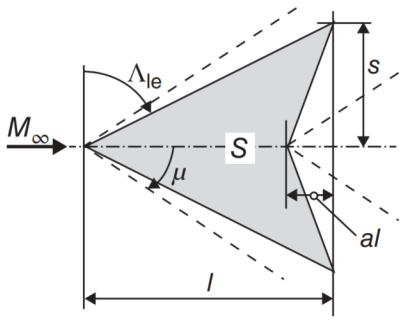

Figure 3.4: Geometry of the flat arrow wing

wing geometry and modifying it by the introduction of the notch ratio a, defined as

$$a = \frac{\cot \Lambda_{\text{le}}}{\cot \Lambda_{\text{te}}}$$

In this adjustment, the center-line section remains stationary, while the tips are shifted downstream parallel to the center-line, ensuring that the wing span remains constant. Parameters such as the planform area (S_{pln}), aspect ratio (AR), and volume remain constant. Instead, the leading edge sweep angle Λ_{le} is increased.
Notching the trailing edges has a notable impact on both the wave drag attributed to volume and the wave drag associated with lift, reducing the total Drag and increasing the aerodynamic efficiency, but off-design aerodynamics and structural weight constraints impose limitations on it.

- Skin Friction Drag:
  This contribution is analyzed in the same manner as the delta wing configuration in equation 3.10, with the exception of the Reynolds number calculation in which mean geometric chord becomes equal to $l_w(1-a)/2$.

- Wave Drag due to Volume:
  The reduction in Wave Drag due to Volume is accounted for by the factor $(1-a)^2$ to accommodate the overall increment in wing length. The equation of the Wave Drag due to Volume coefficient become:

$$C_{D_{WV}} = (1-a)^2 \; K_{WV} \; A_W \left(\frac{t}{c}\right)^2 \tag{3.16}$$

  Otherwise, no distinction is made in the assessment of the fuselage contribution.

- Wave Drag due to Lift:
  The same reasoning made for the Wave Drag due to Volume can be applied to the Wave Drag due to Lift, so the relative coefficient can be written as

$$C_{D_{WL}} = (1-a)^2 \cdot K_{WL} \cdot \frac{\beta^2 \; C_L^2 \; AR}{8\pi} \tag{3.17}$$

- Vortex-Induced Drag:
  Given that the arrow wing maintains the same aspect ratio as the previous configuration and the lift coefficient is determined using the same method, it is possible to calculate the Vortex Induced Drag in the same manner described in equation 3.15.

Blended Body configuration The Blended Body configuration is characterized by distributing the volume both longitudinally and laterally, the leading edges are positioned well behind the Mach cone, leading to a considerably lower optimal slenderness ratio as can be seen in figure 3.5.

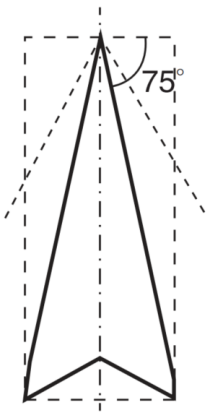

Figure 3.5: Blended Body configuration geometry for M=2 [6]

This configuration results in a decrease in the total wetted area, leading to a reduction in skin friction drag. Additionally, the leading edges of this concept are positioned well behind the Mach cone, resulting in a lower wave drag due to volume.
The only difference with the other configurations regarding the Drag coefficients relates to the Wave Drag due to Volume because there is no longer a distinct separation between the fuselage and wings, so only the contribution of the entire body is taken into account. The corresponding coefficient is given by the relation

$$\frac{C_{D_{\text{wv}}}}{C_L} = r_{\text{S}} K_{\text{SH}} K_\beta \frac{128\bar{\tau}^2 \beta \bar{s}/\bar{l}}{\pi \beta C_L} \tag{3.18}$$

where r_S and τ are respectively the area ratio and the equivalent thickness ratio, that are defined as follow

$$r_S = \frac{S_{\text{pln}}}{2 \cdot s \cdot l_{\text{w}}}$$
$$\bar{\tau} = \frac{\text{Vol}_{\text{w}}}{S_{\text{pln}} \cdot l_{\text{w}}}$$

with $2 \cdot s$ the wing span, l_w the longitudinal wing length and Vol_{w} the wing volume.

The Torenbeek aerodynamic model provides a more detailed analytical formulation of

aerodynamic coefficients compared to the Curran model. It introduces the dependence of these coefficients on the angle of attack (α) as well as the Mach number, with a manageable geometric input requirement. The Torenbeek model also considers the influence of tail surfaces on the coefficient variations. However, it has notable limitations. It is restricted to three specific configurations (delta wing, arrow wing, blended body), which, while representative of the main categories of Horizontal Take-Off and Landing (HTOL) aircraft under study, restricts the freedom to choose arbitrary geometries. Additionally, it is applicable only in the supersonic regime ($1.2 < M < 5$, where air can be treated as a calorically perfect gas with constant specific heats), limiting its use in the conceptual design of the ascent to a specific phase.

3.1.3 Williams model

The Williams aerodynamic model is derived from the book "Estimated Aerodynamics of All-Body Hypersonic Aircraft Configurations" by Louis J. Williams [32]. It reports the analyses conducted to estimate the aerodynamics of a representative family of all-body hypersonic aircraft configurations. This model refers to only a representative configuration of all-body hypersonic vehicle, reported in figure 3.6.

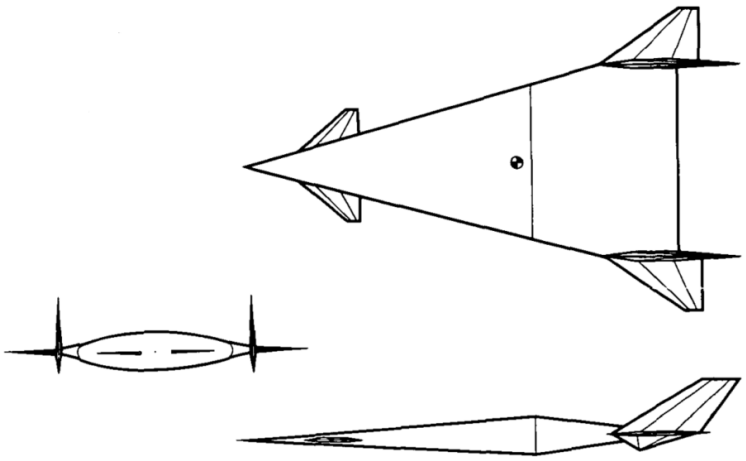

Figure 3.6: Nominal configuration studied in Williams aerodynamic model

In this configuration "the body has a delta planform, with an elliptical cone forebody and an elliptical cross-section afterbody that forms a smooth transition surface from the end of the forebody to a straight-line trailing edge" [32]. The shape is defined by three independent parameters:

1. the sweepback of the body leading edge Λ;
2. the location of the breakpoint between the forebody and afterbody that can be defined as the breakpoint length ratio l_π/l, with l as the length of the total body;

3. the fatness ratio, defined as the ratio of the maximum cross-section area to the total planform area S_π/S.

These shape's parameters allow to define the forebody cross-section ellipse ratio:

$$\frac{a}{b} = \frac{\pi \left(l_\pi/l\right)^2 \cot \Lambda}{\left(S_{\pi/S}\right)} \ . \tag{3.19}$$

The graphical interpretation of all parameters that define the body shape of the configuration can be seen in figure 3.7.

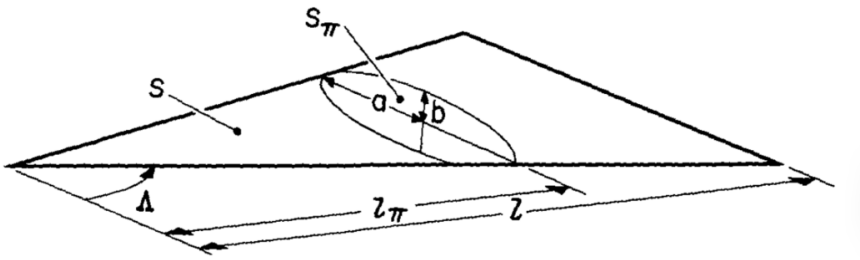

Figure 3.7: Body shape parameters

The mathematical treatment of the Williams model for defining aerodynamic coefficients is presented below.

Lift Coefficient

The lift coefficient for the reference configuration of this model is calculated based on an approximation of the lift equations using nonlinear relationships for a delta wing. These equations were derived through curve fitting data for low aspect ratio wings and applying Gothert's rule or shock-expansion theory where applicable. The coefficients employed in these equations were adjusted to accommodate the rounded leading edge of the all-body configuration. This adjustment accommodates the linear subsonic variation of the elliptic-cone lift coefficient, contrasting with the significant nonlinear variation observed for the sharp leading edge of a delta wing.
The lift coefficient equation formulation is reported below:

$$C_L = C_1 \sin(\alpha) + C_2 \sin^2(\alpha) \tag{3.20}$$

where C_1 and C_2 are coefficient dependents on the flight conditions:

- $\mathrm{M} \leq 1.0$

$$\begin{cases} C_1 = \frac{\pi \cdot AR}{2} - 0.355 \cdot \beta^{0.45} \cdot AR^{1.45} \\ C_2 = 0 \end{cases}$$

- M > 1.0 and $\beta < \frac{4}{\mathrm{AR}}$

$$\begin{cases} \mathrm{C}_1 = \dfrac{\pi \cdot \mathrm{AR}}{2} - 0.153 \cdot \mathrm{AR}^2 \\ \mathrm{C}_2 = \text{linear interpolation with respect to } \beta \text{ from} \\ \qquad \mathrm{C}_2 = 0 \text{ at } \beta = 0 \text{ to} \\ \qquad \mathrm{C}_2 = \mathrm{e}^{[0.955-(4.35/\mathrm{M})]} \text{ at } \beta = 4/\mathrm{AR} \end{cases}$$

- M > 1.0 and $\beta \geq \frac{4}{\mathrm{AR}}$

$$\begin{cases} C_1 = \frac{4.17}{\beta} - 0.13 \\ C_2 = e^{0.955-(4.35/M)} \end{cases}$$

Drag Coefficient

The Total Drag coefficient is the sum of the Zero-Lift Drag C_{D_0} and the Induced Drag C_{D_i}

$$C_D = C_{D_0} + C_{D_i} \tag{3.21}$$

The following lines explain how these two contribution are decomposed.

Induced Drag The induced drag relation utilizes the equation for the sharp leading-edge delta wing, which is modified by a coefficient K_m to accommodate the rounded leading edge of the elliptic cone. This modification leads to leading-edge suction subsonically.

$$C_{D_i} = K_m \cdot C_L \cdot \tan(\alpha) \tag{3.22}$$

where

$$\begin{cases} K_m = 0.25 \cdot (1 + M) & \text{if } M < 3 \\ K_m = 1.0 & \text{if } M \geq 3 \end{cases}$$

Zero-Lift Drag The Zero-Lift Drag can be subdivided into the sum of the body contribution and the tails (fins) contribution:

$$C_{D_0} = C_{D_{B_0}} + C_{D_{F_0}} \tag{3.23}$$

At the same time, these terms can be decomposed in a deep analysis as follow.

- Zero-Lift Body Drag
  The Zero-Lift Body Drag of the basic body was determined by combining the pressure (or wave), skin friction, and nose bluntness drag components (respectively $C_{D_{B_p}}$,$C_{D_{B_f}}$,$C_{D_{B_b}}$). The calculation method for each of these components depended on the Mach number range.

$$C_{D_{B_0}} = C_{D_{B_p}} + C_{D_{B_f}} + C_{D_{B_b}}$$

For the configuration studied, the body pressure contribution can be neglected for subsonic flight ($C_{D_{B_p}} \simeq 0$). In supersonic condition, the wave drag was obtained by numerical integration of the body pressure distribution. Finally, under hypersonic conditions, the Newtonian theory is used. Regarding the body base, Prandtl-Meyer expansion of forebody pressure distribution is used unless $C_{p_{\text{BASE}}} < C_{p_{\text{2D}}}$, when $C_{p_{\text{BASE}}} = -1/(0.91 \cdot M^2 - 0.2 \cdot M + 1.51)$.

The friction drag of the body was computed using a relation based on turbulent boundary layer, flat-plate skin friction, and incorporates an empirical correction for thickness-induced pressure fields. For M<0.8

$$C_{D_{B_f}} = 0.455 \cdot \frac{\left[1 + 2\left(\frac{t}{c}\right)_{\text{body}}\right] \cdot \left(\frac{S_{\text{wet}}}{S_{\text{pln}}}\right)}{(\log_{10} \text{Re})^{2.58} \cdot \left(1 + \frac{\gamma-1}{2} M_0^2\right)^{0.467}} \tag{3.24}$$

where

$$\begin{cases} \text{Re} = \rho_0 \cdot M_0 \cdot a_0 \cdot \frac{\text{MAC}_{body}}{\mu_0} \\ \left(\frac{t}{c}\right)_{body} = \frac{2\frac{l_\pi}{l}}{\frac{a}{b} \cdot \tan \Lambda} \end{cases}$$

and for M>1.2 from numerical integration of local skin friction coefficients on body.

Considering M>1.2, the Body Bluntness Drag is proportional to the nose radius evaluated for a given maximum radiation equilibrium temperature T_{le} and for a given emissivity of the skin $\varepsilon_{\text{Skin}}$, while it can be neglected in the subsonic regime and in the transonic one it is calculated as a linear interpolation between the others.

$$C_{D_{B_b}} = \frac{\pi \cdot r_{\text{nose}}^2}{S_{\text{pln}}} \tag{3.25}$$

where

$$r_{\text{nose}}^{0.5} = \frac{1820 \cdot \left(\frac{\rho}{\rho_{sl}}\right)^{1/2} \cdot \left(M_{max} \cdot a \cdot 10^{-4}\right)^{3.15}}{\varepsilon_{skin} \cdot \left(\frac{T_{le}}{1000}\right)^4} \tag{3.26}$$

- Zero-Lift Fin Drag

  The Zero-Lift Fin Drag was estimated by combining the pressure (or wave), friction, and leading-edge bluntness drag components, indicated respectfully as $C_{D_{F_p}}$, $C_{D_{F_f}}$, $C_{D_{F_b}}$. The aerodynamics of the vehicle did not incorporate trim drag penalties, vertical fin toe-in, or body-fin flow field interactions.

$$C_{D_{F_0}} = C_{D_{F_p}} + C_{D_{F_f}} + C_{D_{F_b}}$$

The component relative to pressure (or wave) is assumed to zero in subsonic flight ($C_{D_{F_p}}$ for M<0.8). In the transonic regime (0.8<M<1.0), it was assumed that the quantity increases linearly concerning the Mach number, starting from zero and reaching its computed value at Mach 1. The wave drag of the fin at Mach number 1 was estimated

using an empirical equation as follow

$$C_{D_{F_p}} = 3.4 \cdot \left(\frac{t}{c}\right)_{fin}^{\frac{5}{3}} \cdot \frac{S_{fin}}{S_{pln}} \cdot \cos^2\left(\Lambda_{fin}\right) \tag{3.27}$$

At Mach numbers equal to or greater than the shock attachment Mach number M_{SA}, the wave drag was estimated using linear supersonic theory as in the following equation

$$C_{D_{F_p}} = 6 \cdot \left(\frac{t}{c}\right)_{fin}^{2} \cdot \frac{1}{\beta} \cdot \frac{S_{fin}}{S_{pln}} \tag{3.28}$$

Finally, for $1< M < M_{SA}$ the wave drag was found by linear interpolation.
Fin Friction Drag contribution is derived from a relationship for turbulent boundary layer, flat-plate skin friction corrected for the effects of pressure gradients, like the body one.

$$C_{D_{F_f}} = 0.455 \cdot \frac{\left[1 + 2\left(\frac{t}{c}\right)_{\text{fin}}\right] \cdot \left(\frac{(S_{WET})_{\text{fin}}}{S_{\text{pln}}}\right)}{\left(\log_{10} \text{Re}_{\text{fin}}\right)^{2.58} \cdot \left(1 + \frac{\gamma-1}{2} M_0^2\right)^{0.467}} \tag{3.29}$$

where

$$\text{Re}_{fin} = \rho_0 \cdot M_0 \cdot a_0 \cdot \frac{MAC_{fin}}{\mu_0}$$

Finally, the last part of the total Zero-Lift Fin Drag related to the Fin Bluntness is estimated from the Newtonian flow approximation. For $M \geq 1.0$ is described by the following equation

$$C_{D_{F_b}} = \frac{8}{3} \cdot \frac{r_{le,fin} \cdot b_{fin}}{S_{pln}} \cdot \cos^2\left(\Lambda_{fin}\right) \tag{3.30}$$

where

$$r_{le,fin} = \left(0.725 \cdot \cos^{1.2}\left(\Lambda_{\text{fin}}\right)\right)^2 \cdot r_{\text{nose}}$$

while in subsonic conditions it can be considered zero and for $0< M <1$ it is assumed to vary linearly with respect to M.

In conclusion, the Williams model allows for a reasonably detailed calculation of aerodynamic coefficients, suitable for an initial design phase. Lift and drag coefficients are expressed as functions of the angle of attack and Mach number, with no limitations regarding the flight regime, making it applicable from subsonic to hypersonic speeds. Additionally, it enables the consideration of the aerodynamics of tail surfaces and canards. However, the downside of this model, aside from the high number of geometric inputs that may represent a challenge at this project stage, is that the study conducted is specific to a certain configuration. Although the shape can be modifiable through the three parameters described, it may not always be representative of a modern high-speed aircraft, thereby limiting the range of configurations that can be studied.

3.1.4 Raymer model

Raymer's aerodynamic model is taken from the book "Aircraft Design: A Conceptual Approach" edited by Daniel P. Raymer [7]. It presents an in-depth analytical treatment of aerodynamic coefficients and represents the most complete model of those analysed. It is able to enhance the accuracy of results compared to previous methods, expressing the coefficients as functions of both the Mach number and the angle of attack α with no limitations for M. It takes into account the contributions of key components of the aircraft, including the wing, fuselage, and tail planes, as well as intricate elements such as air intakes, engine nacelles, and various other components. This results in a high number of inputs.
The problem is that the Raymer model refers to a generic high-speed aircraft configuration where there is a clear distinction between the fuselage and the delta wing, as in the configuration model reported in figure 3.8. This constitutes a significant limitation in the design of a

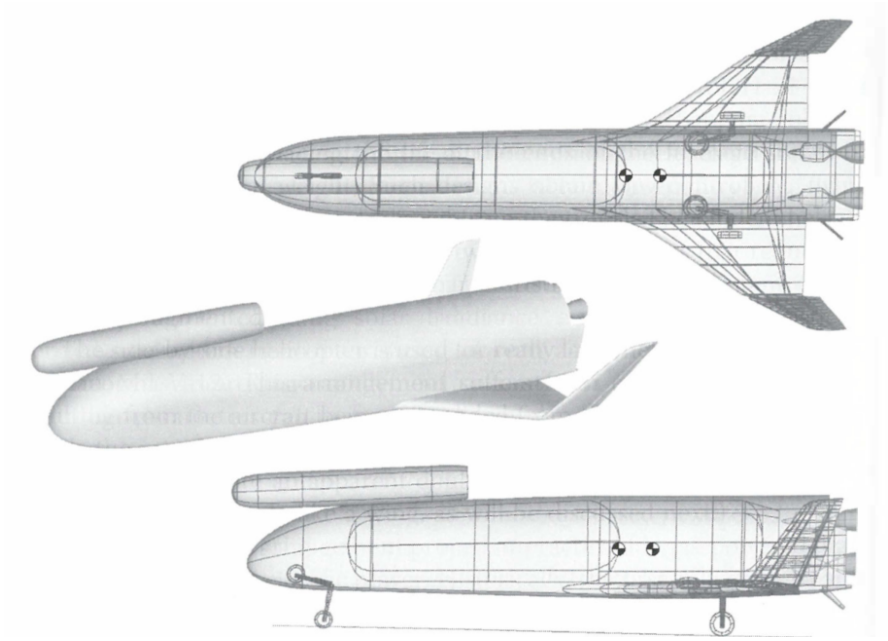

Figure 3.8: Reusable launch vehicle [7]

hypersonic access-to-space vehicle as it does not allow for the consideration of blended-body configurations. For this reason, this model has been discharged from the current case study, so its treatment has not been reported here.

3.2 Selected models

The procedure for selecting aerodynamic models to implement in the methodology is detailed below. It is essential to remember that the ultimate goal is to incorporate one or more of these models into a software tool useful for the conceptual design of a reusable access-to-space vehicle, where this design phase faces limited availability of geometric data for obvious reasons.

As mentioned earlier, the use of these analytical/semi-empirical models can be complemented (or entirely substituted) by aerodynamic data from experimental databases or CFD analyses of real or prototype aircraft, as extensively documented in [33]. This type of approach is called *multifidelity approach*, as explained by figure 3.9.

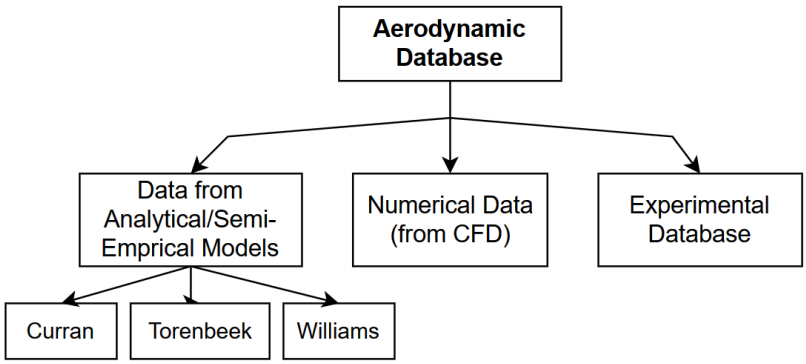

Figure 3.9: Multifidelity approach for aerodynamic database

This perspective allows the user complete freedom of choice. Additionally, the idea is to enable users to optionally input their aerodynamic databases, in the unlikely event that they possess their own CFD data or data from real aircraft. Figure 3.10 reports a schematic representation of the different ways to obtain aerodynamics data, separating the tool-obtained data from the user-inserted one.

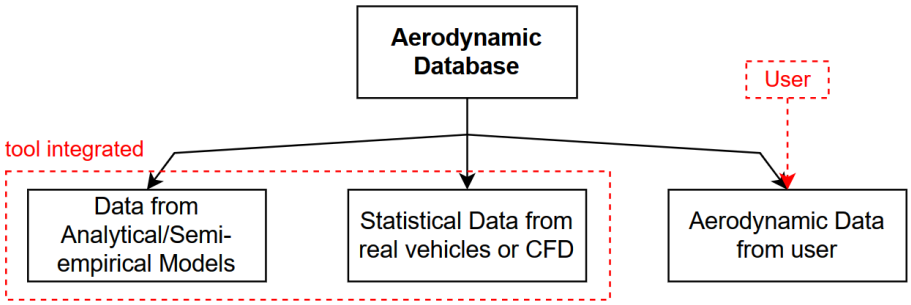

Figure 3.10: Aerodynamic data sources

The Curran model provides a simplified and fast analysis of aerodynamic coefficients. Importantly, it imposes no limits on the studied configuration or flight Mach number. It disregards the dependence on the angle of attack, expressing coefficients solely as a function of Mach number. Consequently, it may be somewhat inaccurate, but for an initial design phase, it remains a valid choice.
The Torenbeek model, on the other hand, proves to be more detailed and reliable compared to Curran, although it is limited to the study of three specific configurations (delta wing, arrow wing, blended body), considered representative of the type of aircraft under examination. It expresses aerodynamic coefficients as functions of both Mach number and angle of attack.

However, its application is restricted to the Mach number range of $1.2 < M < 5$. This implies that it can only be used in the supersonic regime and, consequently, must be complemented by other models for a comprehensive analysis of access-to-space missions.
The Williams model expresses the aerodynamic coefficients of a specific configuration representative of high-speed supersonic aircraft, in which geometry can be varied through three geometric parameters. This makes it less suitable for blended-body geometries, but it can still be used at the expense of less precise results. Therefore, it can still be implemented into the methodology, with a disclaimer attesting to its limitations. The Williams model provides coefficients as functions of both Mach and angle of attack and does not have limitations related to flight Mach number, but it requires a relatively high number of inputs.
Finally, Raymer's aerodynamic model represents the most accurate method for calculating aerodynamic coefficients. It is a relatively complex model based on the build-up approach, requiring a high number of inputs and consequently a good understanding of the geometry. In terms of applicability, this model refers to aircraft with a clear distinction between the wing and fuselage, making it less suitable for the aerodynamic characterization of blended-body aircraft. For this reason, the Raymer model has been discarded. The information regarding the aerodynamic models is summarized in table 3.1 (where *#Input* indicates the number of geometric inputs required by the model).

Model:	**Variables:**	**Configuration limits:**	**M limits:**	**#Inputs:**
Curran	M	-	-	3
Torenbeek	M, α	High-speed configuration allowed: generic with a delta wing; generic with an arrow wing; blended wing body configuration	$1.2 \div 5$	20
Williams	M, α	Delta planform, with an elliptical cone forebody and an elliptical cross-section afterbody that forms a smooth transition surface from the end of the forebody to a straight-line trailing edge	-	20
Raymer	M, α	Aircraft with clear distinction between wing and fuselage	-	28

Table 3.1: Comparison of analysed aerodynamic models

In conclusion, among the analyzed aerodynamic models, not all have been deemed suitable for the aerodynamic characterization required in conceptual design. The Curran model has been chosen as the most suitable for an initial implementation in the sizing code due to its simplicity and speed of application, and it proves to be accurate enough, as demonstrated in [34], where the obtained data using the model are compared with data from various types of

real aircraft. A MATLAB [44] code implementing the model has been developed and inserted in the sizing code of the tool.

Chapter 4

Propulsion Strategies

This chapter discusses the propulsion strategies studied for the propulsive characterization of a reusable Single-Stage-To-Orbit launcher. The goal is to find propulsion models with relatively simple analytical treatments capable of expressing thrust (or specific thrust) as a function of Mach number and altitude, enabling their integration into the sizing code of the conceptual design tool. In the diagram in figure 4.1, the work flow for the propulsive characterisation implemented in the developed methodology is shown.

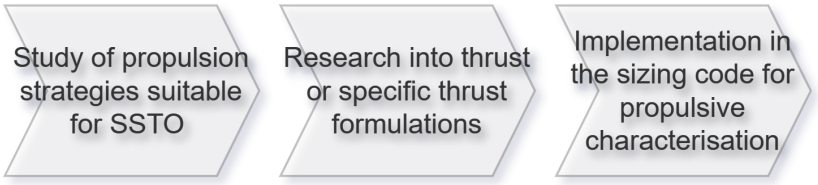

Figure 4.1: Work flow for the propulsive characterisation

Firstly, the types of propulsion systems that represent the best alternatives for the SSTO are presented. The choice of propulsor type (or types) is a fundamental step in the conceptual design of a access-to-space mission, especially for the ascent phase. The main propulsion systems analyzed include turbojet and turbofan, ramjet, scramjet, and rocket. It is important to emphasize that none of these types of engines individually allows the vehicle to achieve SSTO, except for the rocket accepting an infinitesimal payload. Therefore, it becomes necessary to combine multiple propulsion systems in the vehicle for sequential use, or use the so-called "combined cycle" engines, which integrate multiple propulsion modes in the same engine.

An analysis of statistical data on ramjet and scramjet engines is then presented, which was necessary to obtain initial thrust values for insertion into the first iteration of the sizing cycle. Subsequently, the sizing of the air intake for the ramjet/scramjet engine is reported.

4.1 Engines

Before introducing the various types of propulsion systems, it is essential to describe the Brayton cycle. It outlines the functioning of all airbreathing engines and is characterized by four processes: isentropic compression, isobaric heat addition, isentropic expansion, and isobaric heat rejection. In figure 4.2 is depicted the Brayton cycle in a temperature-entropy ($T - s$) diagram [14].

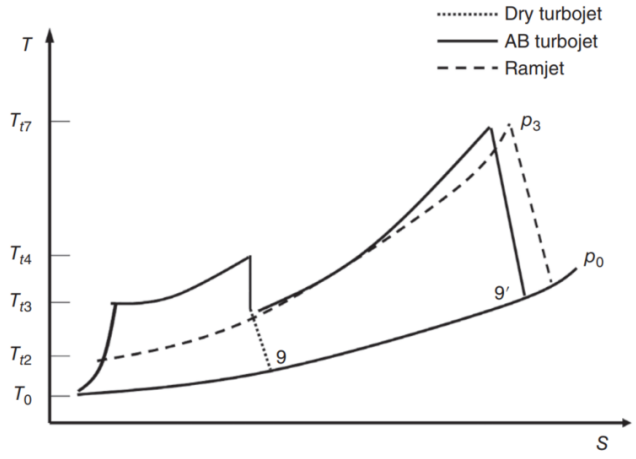

Figure 4.2: Temperature–entropy diagram for turbojet (dry and with afterburner) and ramjet engines (Brayton cycle)

As mentioned earlier, none of the propulsion systems presented above, when used individually, is capable of achieving SSTO. The only exception is represented by the rocket, which can reach a VLEO but with an extremely low payload fraction, making it impractical. Consequently, a vehicle for orbital access must use these types of engines sequentially, transitioning from one to another at an appropriate Mach number. Alternatively, innovative combined-cycle propulsion systems can be employed, which will be discussed in the following section. The initial mission phase, from take-off to low subsonic speeds, can be accomplished with a turbojet/turbofan engine or an ejector rocket. Subsequently, the transition can be made to a ramjet and scramjet (or dual-mode scramjet), covering the Mach number range of approximately 2.0<M<12. Finally, the ascent is completed using a rocket. Figure 4.3 depicts a comparison between these propulsive systems in terms of specific impulse, i.e., the impulse gained per unit mass of propellant (which is inversely proportional to specific fuel consumption), as a function of flight Mach number. Airbreathing engines have greater I_{sp}: the benefit of air-breathing propulsion compared to rocket propulsion lies in its utilization of atmospheric oxygen for combustion. Naturally, the effectiveness of a propulsion system in a flight vehicle is determined not solely by the fuel consumption per unit time but by the cumulative consumption over the entire mission duration. Therefore, another fundamental parameter for assessing the performance of a propulsion system is the thrust-to-weight ratio T/W_e, which relates the engine thrust to its weight. Considering only this parameter, the rocket has a significant advantage

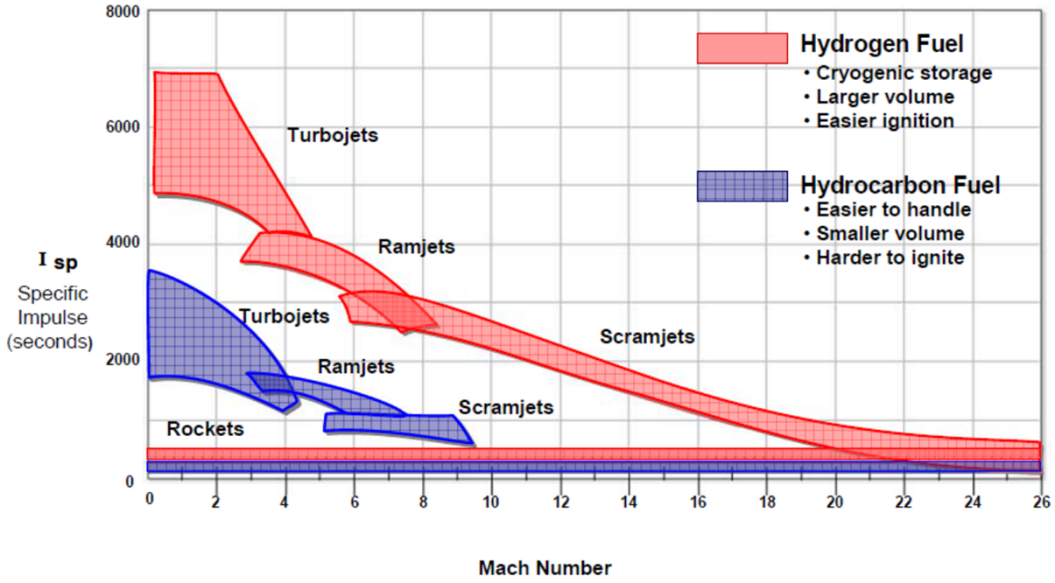

Figure 4.3: Specific impulse I_{sp} of different, hydrogen-fueled and hydrocarbon-fueled propulsion systems as function of the flight Mach number [8]

because it does not require an inlet.
Nevertheless, it is the specific performance $T \cdot I_{sp}/W_e$, defined as the product of specific impulse and thrust-to-weight ratio, which determines performance of a propulsion system. In figure 4.4 is reported the range of this parameter for different propulsion systems as a function of flight Mach number. Figure 4.4 provides an initial indication of the Mach numbers at

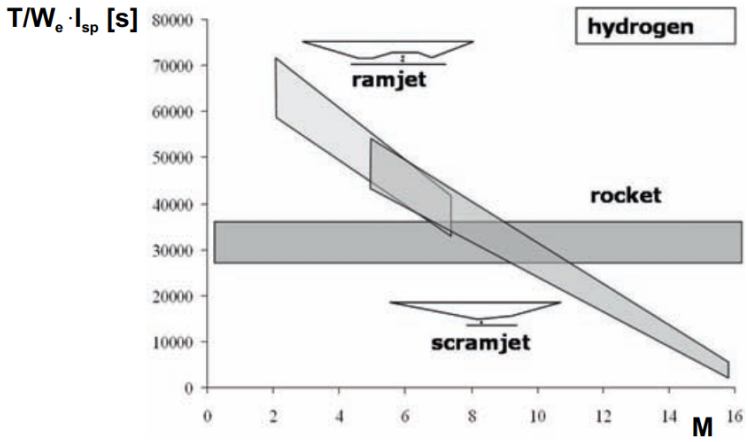

Figure 4.4: Specific performance of different, hydrogen-fueled propulsion systems as function of the flight Mach number [9]

which to change the propulsion system (for example, from scramjet to rocket at approximately $M = 12$). However, this should not be taken as a reference since it considers only the characteristics of the propulsion system and not those of the entire vehicle, which strongly influences

performance.

Follow a description of the spaceplane's main engines.

4.1.1 Turbojet/Turbofan

Turbojet and Turbofan are the best engines for the subsonic and early supersonic flight. Indeed, they are capable of generating thrust under take-off conditions (M=0) and exhibit good performance up to Mach numbers around 2. In this conditions, an increase in pressure of the incoming atmospheric air requires mechanical compression through a compressor.

Turbojet

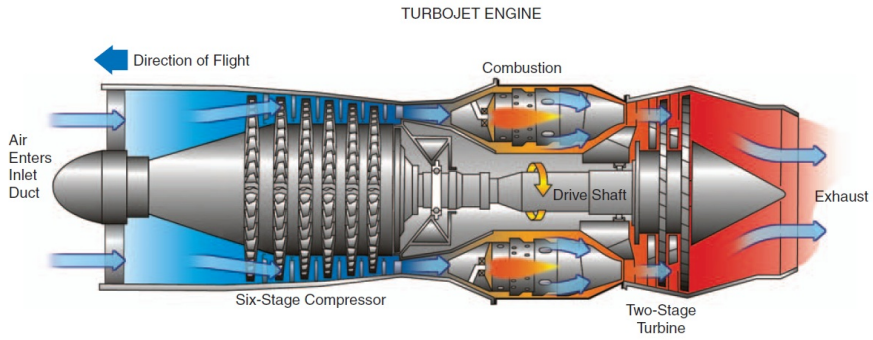

Figure 4.5: Basic turbojet engine [10]

The Turbojet, as seen in Figure 4.5, is composed, in order, of an intake, a mechanical compressor, a combustor, a turbine, and a nozzle. In this engine, the air ingested by the motor is mechanically compressed and slowed down by an axial compressor, then passes into the combustion chamber where it is mixed with fuel, and combustion occurs. The hot combustion gases are first expanded in a turbine connected to the compressor through a common driveshaft. The expansion process is constrained to ensure that the work required to drive the compressor is solely provided by the turbine, with the remaining expansion taking place in the exhaust nozzle to generate a high-velocity stream of hot gas, which is responsible for producing the thrust force. The engine's geometry remains consistent in both the subsonic and supersonic versions, except for variations in the intake and nozzle.
As reported in [12], in case the exhaust plane pressure is atmospheric (adapted nozzle condition), the specific thrust is given by

$$\frac{\mathcal{T}}{\dot{m}_a} = [(1+f)w_e - u] \tag{4.1}$$

where w_e is the exhaust velocity (or nozzle exit velocity) and u is the flight speed. The exit

velocity can be obtained through the total enthalpy conservation in the adapted nozzle:

$$w_e = \sqrt{2\ c'_p\ T_4^\circ \left[1 - \frac{1}{(\varepsilon_n \beta_n)^{\frac{\gamma'-1}{\gamma'}}}\right]} \tag{4.2}$$

with ε_n and β_n the expansion ratios of respectively turbine and nozzle. Denoting the thermal efficiency as $\eta*$, the thrust specific fuel consumption is given by

$$\text{TSFC} = \frac{\dot{m}_f}{\mathcal{T}} = \frac{f}{(1+f)w_e - u} = \frac{w_e + u}{2\eta^* H_i}. \tag{4.3}$$

Turbofan

Since thermal efficiency is inherently limited by the Carnot cycle, to reduce fuel consumption, it is necessary to consider decreasing the specific work w_e. To decouple thrust generation from gas generation, a portion of power is extracted to accelerate a second flow not involved in combustion (fan or cold flow), introducing a new degree of freedom μ, known as the By-Pass Ratio (BPR).

$$\mu = \frac{\dot{m}_f}{\dot{m}_c}$$

that is defined as the ratio between the "fan" flow rate (cold) and the "core" flow rate (hot). This transition leads from the Turbojet to the Turbofan engine [11].

The Turbofan can be seen as a turbojet with an additional duct (figure 4.6), of which two main configurations can be identified:

- *Separated flows turbofan*: characterized by a high BPR, this type of turbofan is conventionally employed in subsonic flight. While it offers low fuel consumption, it is associated with larger overall dimensions.

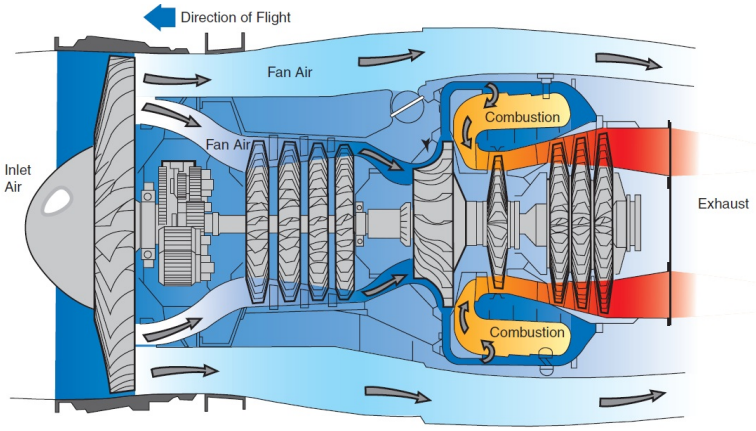

Figure 4.6: Turbofan engine [10]

- *Mixed flows turbofan*: characterized by a limited By-Pass Ratio (BPR), in which the two flows are mixed in a mixer before expanding in the nozzle. They are typically used for supersonic flight.

As seen in figure 4.7, mixing ensures a greater specific thrust at a given consumption (thus better performance), but it leads to an increase in the engine's weight due to the presence of the mixer.

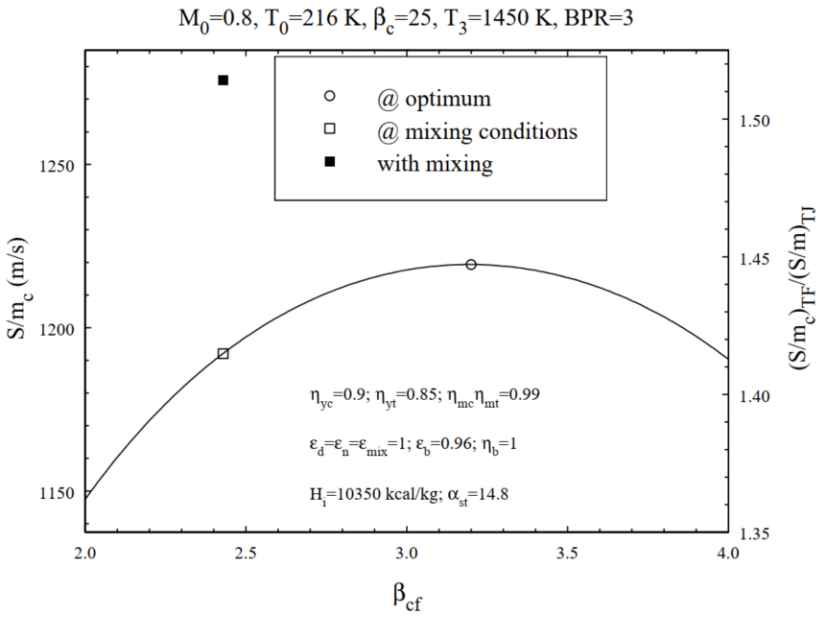

Figure 4.7: Specific thrust referred to core flux of turbofan in function of the compression ratio of the cold (fan) flux [11]

The specific thrust of a turbofan engine can be expressed [12] as follow:

$$\frac{\mathcal{T}}{\dot{m}_a} = (1+f)w_e + \mu \cdot w_{e_f} - (1+\mu)u \tag{4.4}$$

where w_e is the core exhaust velocity, while w_{e_f} indicates the fan nozzle exit velocity. The latter is calculated as

$$w_{e_f} = \sqrt{2\ \eta_{f_n}\ c_p\ T^{\circ}_{2f}\left[1 - \left(\frac{1}{\beta_{n_f}}\right)^{(\gamma-1)/\gamma}\right]} \tag{4.5}$$

in which η_{f_n} is the adiabatic efficiency for the cold (fan) nozzle, T°_{2f} the fan outlet total temperature and β_{n_f} the expansion ratio of the cold nozzle, while

$$w_e = \sqrt{2\ \eta_{c_n}\ c'_p\ T^{\circ}_{4}\left[1 - \left(\frac{1}{\beta_{n_c}}\right)^{(\gamma'-1)/\gamma'}\right]} \tag{4.6}$$

with η_n is the adiabatic efficiency for the hot (core) nozzle, T_4° the turbine outlet total temperature, β_{n_c} the expansion ratio of the hot (core) nozzle and the superscript indicates burned gas conditions.
The thrust specific fuel consumption of a turbofan engine is calculated as follows:

$$\text{TSFC} = \frac{\dot{m}_f}{\mathcal{T}} = \frac{f}{(1+f)w_e + \mu \cdot w_{e_f} - (1+\mu)u} \tag{4.7}$$

With afterburner

A significant increase in thrust can be achieved by utilizing an afterburner. This is an additional combustion chamber located after the turbine and before the nozzle (refer to figure 4.8) and can be used in both turbojet and turbofan engines. The afterburner raises the temperature of the gas preceding the exhaust nozzle. As a consequence of this temperature increase, there is an approximately 40% surge in thrust during take-off and an even greater percentage at higher speeds once the vehicle is airborne. In these cases, part of the heat is supplied at lower pressures, resulting in lower efficiency.

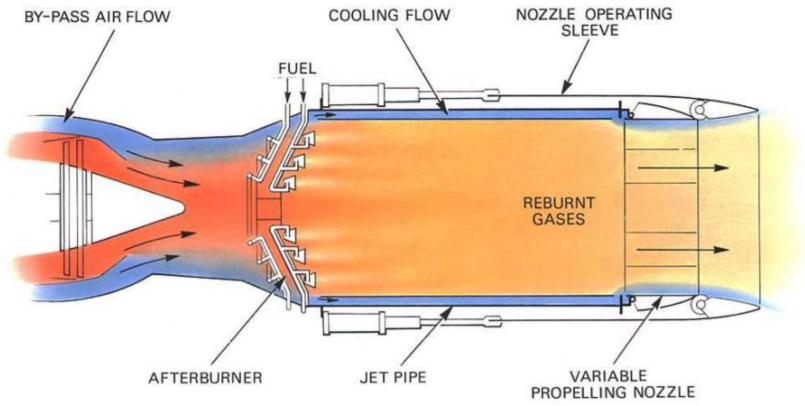

Figure 4.8: Schematic diagram of a turbojet engine with afterburner [12]

To consider the afterburner's contribution to the specific thrust to include it in the sizing code, the nozzle exit velocity (equation 4.2 for turbojet, equation 4.6 for turbofan) is modified, now including the total temperature at the afterburner exit T_5°. The nozzle exit velocity becomes:

$$w_e = \sqrt{2\ c_p'\ T_4^\circ \left[1 - \frac{1}{(\varepsilon_n \beta_n)^{\frac{\gamma'-1}{\gamma'}}}\right]} \tag{4.8}$$

4.1.2 Ramjet

The ramjet is the simplest of all air-breathing engines, utilizing the natural "ram effect" to compress the ingested free-stream air. It consists of three main components: an inlet diffuser,

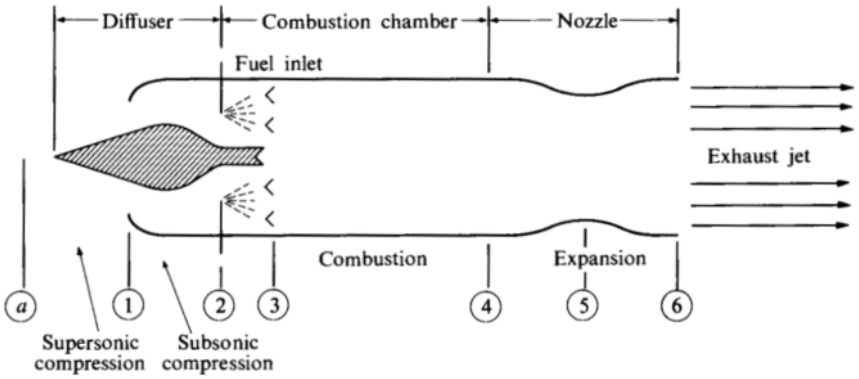

Figure 4.9: Schematic diagram of a ramjet engine [13]

a combustor or burner, and a thrust nozzle, as depicted in figure 4.9 where the ramjet has a spike-like inlet diffuser [12].

In this type of engines, the incoming atmospheric air, flowing at supersonic speed, is first compressed at the nose of the vehicle by passing through the oblique shock anchored by the central spike. Then, after encountering a terminal normal shock at the cowl lip, the air flows into the core of the engine. In the diffuser, the majority of the air's kinetic energy is transformed into a pressure increase. Following compression by the inlet shocks, the air significantly slows down, attaining subsonic velocity. Within the subsonic diffuser, the airflow experiences an additional increase in pressure before reaching the combustion chamber. In the combustor fuel is injected and mixed with the compressed air and ignited (isobaric heat addition in Brayton cycle). Then, the hot combustion gas expands, passing through a convergent-divergent nozzle, before being expelled at high velocity to generate thrust.

The ramjet is capable of generating thrust even in subsonic flight, but due to the absence of shocks that compress the flow, the performance will be poor, i.e., the specific thrust would be very low. A similar consideration applies to hypersonic flight, where the ramjet is replaced by the scramjet. Therefore, the ramjet engine can operate effectively in the flight Mach range of 1.0<M<6.0, as demonstrated by the figure 4.10 which shows the trend of specific thrust as the flight Mach varies. According to [12] and considering an ideal ramjet engine (compression and expansion processes in the engine are reversible and adiabatic, and the combustion process takes place at constant pressure), the Specific Thrust $\mathcal{T}/\dot{m}_a$ can be expressed as follow:

$$\frac{\mathcal{T}}{\dot{m}_a} = \mathrm{M}\sqrt{\gamma R T_a}\left[(1+f)\sqrt{T_{04}/T_a}\left(1+\frac{\gamma-1}{2}\mathrm{M}^2\right)^{-1/2} - 1\right] \tag{4.9}$$

where T_{04}/T_a is the ratio of the maximum temperature to the ambient temperature, and f is the fuel-air ratio.
Accordingly, the thrust specific fuel consumption (TSFC) is given by

$$\mathrm{TSFC} = \frac{\mathcal{T}}{\dot{m}_f}. \tag{4.10}$$

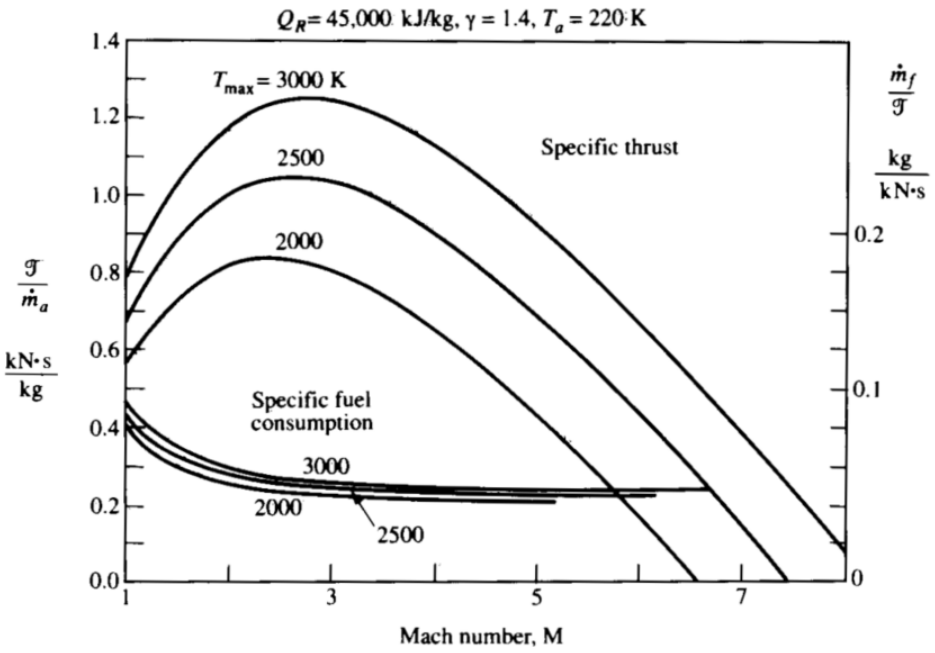

Figure 4.10: Ideal ramjet thrust and fuel consumption in function of flight speed [12]

In figure 4.10 is shown the dependence of specific thrust and TSFC on flight Mach number and maximum temperature.

4.1.3 Scramjet

The scramjet engine works similarly ramjet, but it's used where the flight Mach number exceed 5 (entering in hypersonic regime). The difference is that, at these velocities, the temperature increase following the ram compression to subsonic speeds is so high that little or no additional heat can be added in the combustor by burning fuel. The only alternative is to utilize the inlet to decelerate the flow from the flight speed to a lower supersonic Mach number, preventing excessive temperature rise. So the combustion process takes place at supersonic conditions, and ramjet becomes supersonic combustion ramjet (SCramjet), shown in figure 4.11. The

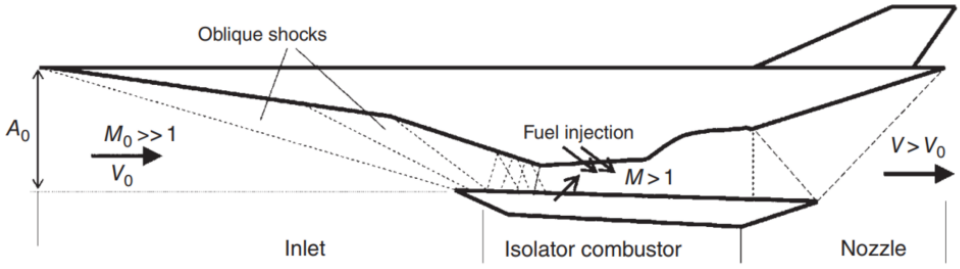

Figure 4.11: Schematic of vehicle-integrated scramjet engine [14]

scramjet engine can operate effectively in the Mach flight range 5.0<M<15, representing a

hypersonic air-breathing engine.

To estimate the specific thrust of a scramjet, a treatment in terms of Kinetic Energy Efficiency can be used. This method is built on the premise that each significant component of the engine operates in accordance with its capability to handle the working fluid. It is assumed that the working fluid behaves as a calorically perfect gas with consistent calorific constants across the entire engine. Consequently, the kinetic energy efficiencies of the engine's inlet, combustor, and nozzle are denoted respectively as $\eta_{KE,c}$, $\eta_{KE,b}$, and $\eta_{KE,e}$. The total kinetic energy efficiency of the scramjet is equal to

$$\eta_{\mathrm{KEO}} = \eta_{\mathrm{KE,c}} \cdot \eta_{\mathrm{KE,b}} \cdot \eta_{\mathrm{KE,e}}. \tag{4.11}$$

According to [14], can be assumed that the overall kinetic energy efficiency of the air-breathing engine falls within the range of $0.65 < \eta_{\mathrm{KEO}} < 0.75$. Thus, the specific thrust of a scramjet engine is given by:

$$\frac{\mathcal{T}}{\dot{m}_a} = \mathrm{M}\sqrt{\gamma R T_a}\left\{\sqrt{\eta_{\mathrm{KEO}}\ (1+f)\left[1+\frac{\eta_b\ f\ H_i}{c_p T_a\,(1+((\gamma-1)/2)M^2)}\right]}-1\right\} \tag{4.12}$$

where H_i indicates the lower heating value (or lower calorific value) of the fuel and the subscript 'a' indicates values referring to ambient conditions.

Dual-mode Scramjet

The Dual-mode Scramjet engine has the capability to function both as a ramjet and a scramjet, depending on whether it combusts fuel in subsonic or supersonic conditions. It can transit between these engine modes, allowing it to propel a vehicle within the flight regime where $2.0 < \mathrm{M} < 15$.

4.1.4 Chemical Rocket

Rockets differ from air-breathing propulsion engines in the fact that they carry their entire propellant with them. They generate thrust by transferring energy and momentum to the propellant as it is expelled from the engine. For this reason, their performance is independent of flight speed and external conditions, making them suitable for space applications, unlike air-breathing engines. Additionally, they can operate across a broad range of thrust levels, although their fuel consumption is significantly higher compared to air-breathing engines.
The chemical rocket may differ depending on the types of propellants it uses:

- *Solid Rocket Motor* if it uses solid propellant: in this case, it is not possible to control thrust (without using complex devices such as variable geometry nozzles) and extinguishing the motor is challenging, but the engine is simpler;
- *Liquid Rocket Engine* if it uses liquid propellants, it is possible to vary thrust by regulating the flow of propellants, but the system is much more complex;

- *Hybrid Rocket Engine* if one of the propellants is in solid form while the other is in liquid form (usually the oxidizer is liquid), they allow a certain degree of flexibility and control similar to liquid rocket engines, while retaining a certain construction simplicity typical of solid rocket motors.

In this discussion, only the liquid rocket engine is considered, where figure 4.12 reports a scheme.

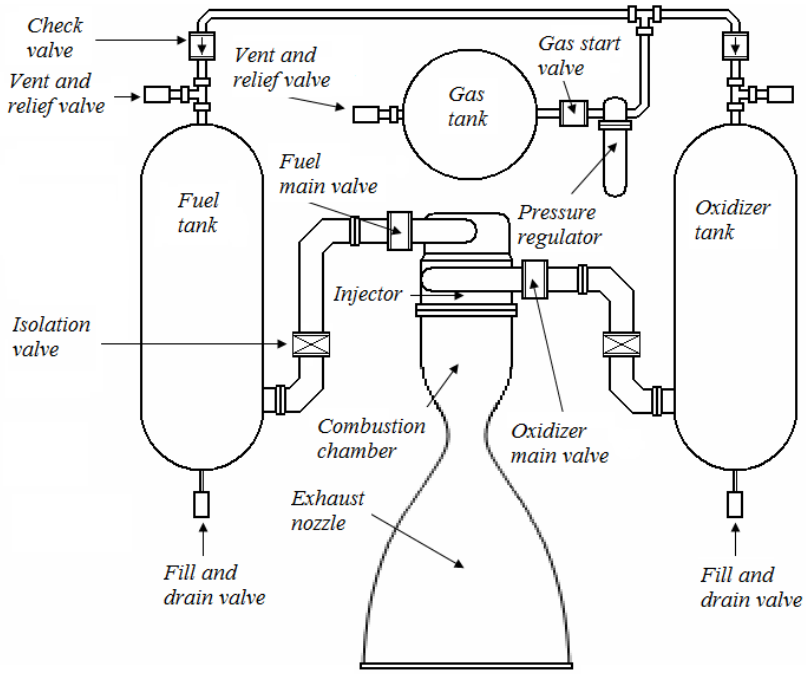

Figure 4.12: Scheme of a Liquid Rocket Engine with pressurized gas propellant feed system [15]

The thrust of a rocket engine, using a simplified 1D model, is given by the following equation:

$$\mathcal{T} = \dot{m}\ w_e + A_e\,(p_e - p_o) \tag{4.13}$$

where the flow mass ratio in the nozzle $\dot{m}$ is

$$\dot{m} = \frac{A_t\ p_t}{\sqrt{T_t}} \sqrt{\frac{\gamma}{\mathrm{R}}} \left(\frac{\gamma+1}{2}\right)^{-\frac{\gamma+1}{2(\gamma-1)}} \tag{4.14}$$

where subscript 't' indicates the conditions in the nozzle throat (i.e. minimum cross-section). In this section, the hot exhaust flow is choked, which means that the Mach number is equal to 1.0 in the throat.

The specific impulse of a rocket is:

$$I_{sp} = \frac{I_t}{g_0 \; M_p} = \frac{\mathcal{T} \; dt}{g_0 \; dm} = \frac{c}{g_0} \; . \tag{4.15}$$

Here, I_t represents the total impulse, obtained by integrating the thrust over the burning time, M_p is the propellant mass, and c is the effective exhaust velocity. As shown in figure 4.3, rocket engines have a significantly lower I_{sp} than airbreathing engines.

As mentioned at the beginning of the chapter, space access vehicles propelled only by fixed-geometry rockets are capable of achieving Single Stage to Orbit (SSTO) with a negligible payload, making it considered infeasible. To demonstrate this, can be used the Rocket Equation (or Tsiolkovsky Equation). It is derived from the definition of thrust as a change in momentum and expresses the maximum change of velocity of the vehicle ΔV (with no external forces acting):

$$\Delta V = c \cdot \ln \frac{m_i}{m_f} = I_{\text{sp}} \cdot g_0 \cdot \ln \frac{m_i}{m_f} \tag{4.16}$$

where m_i and m_f represent respectively the initial and final mass of the vehicle during the SSTO. Rearranging the previous equation can be obtained the mass ratio:

$$\frac{m_i}{m_f} = e^{-\frac{\Delta V}{c}} \; . \tag{4.17}$$

A graphical representation of the rocket equation is presented in Figure 4.13, displaying the mass ratio as a function of the change in velocity. A value of the latter of approximately 10 km/s is associated with reaching a Low Earth Orbit (LEO). Various combinations of oxidizers and fuels were considered, and these are detailed in table 4.1. It can be noted that, for

Oxidizer	**Fuel**	***c*** [m/s]
LOX	LH2	450
LOX	CH4	380
LOX	RP-1	310
LOX	UDMH	290
N2O4	MMH	320

Table 4.1: Propellants for Liquid Rocket Engine and I_{sp} correlated

the combination of liquid hydrogen and liquid oxygen, which represents the best solution, the m_f/m_i ratio for a ΔV of 10 m/s is approximately 0.1. Therefore, 90% of the initial mass of the vehicle is propellant mass m_p. The remaining mass must include the mass of structures and systems (including the engine) m_s and the payload mass m_u. To better understand the problem, it is useful to introduce two parameters, the structural coefficient ε, and the payload

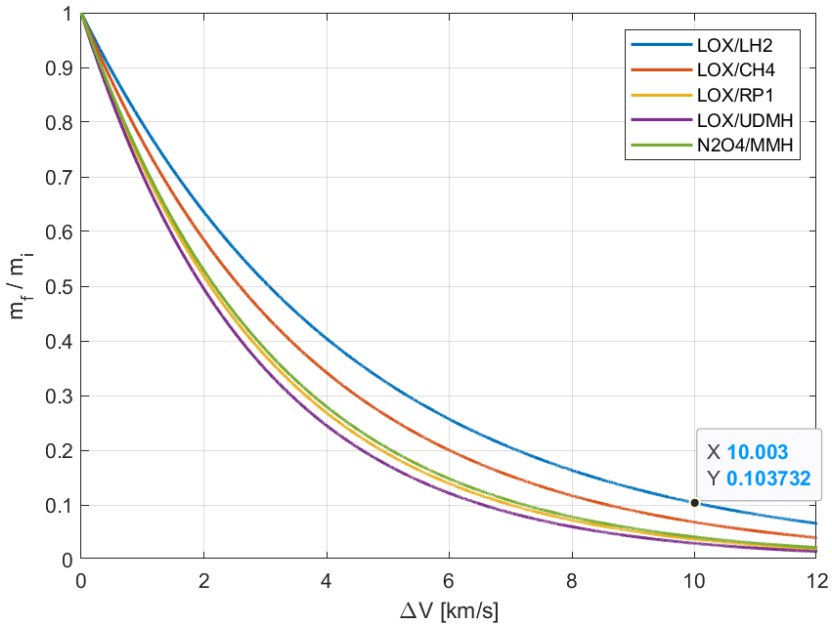

Figure 4.13: Vehicle mass ratio in function of mission ΔV

fraction λ, defined as:

$$\varepsilon = \frac{m_s}{m_s + m_p} \qquad \text{and} \qquad \lambda = \frac{m_u}{m_i}$$

Since the goal of a space access mission is to place a certain payload into orbit, it is desired that the payload fraction be as high as possible. This can be expressed as a function of the change in velocity as follows:

$$\lambda = \frac{e^{-\frac{\Delta V}{c}} - \varepsilon}{1 - \varepsilon}. \tag{4.18}$$

To evaluate the structural coefficient, it is important to differentiate whether the propellants are cryogenic or not. Through [36] and [37], values for ε have been approximated, as reported in Table 4.2. It is emphasized that these are estimated values and tend to be conservative.

Propellants	$\boldsymbol{\varepsilon}$
Both storable	0.08
One cryogenic	0.10
Both cryogenic	0.13

Table 4.2: Structural coefficient depending on propellants characteristics

In Figure 4.14, the results obtained for the payload fraction in a SSTO with only rockets are presented. Specifically, Figure 4.14a shows the trend of λ with varying change in velocity, while in Figure 4.14b the payload fraction is calculated as a function of the orbit altitude to provide a clearer indication of the rocket's performance in SSTO at a glance. In the latter, given the orbit

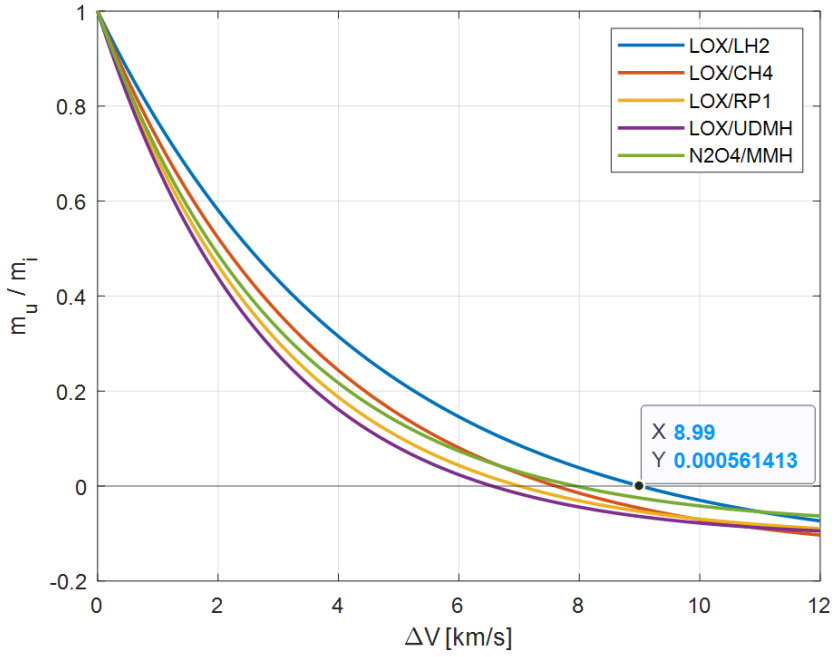

(a) Payload fraction in function of change in velocity

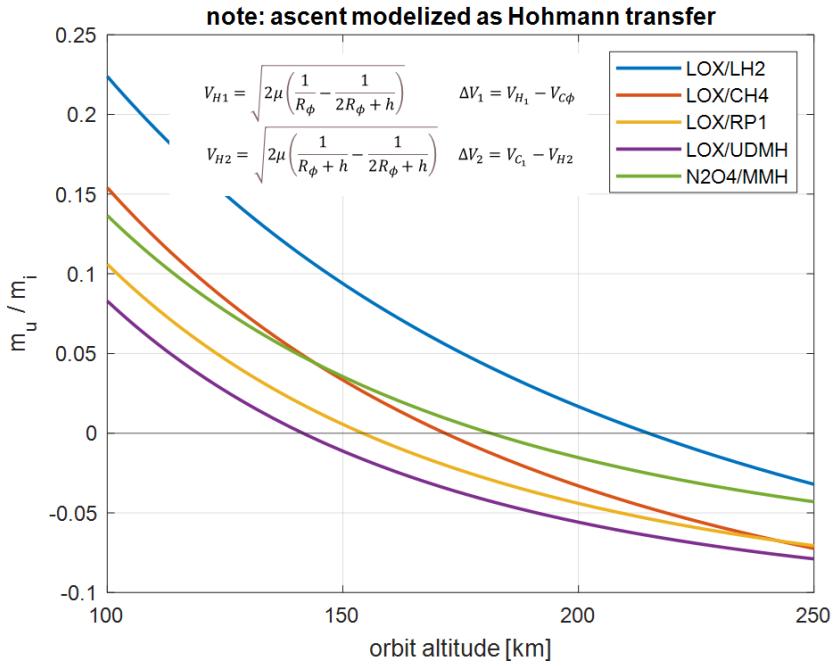

(b) Payload fraction in function of target orbit altitude

Figure 4.14: Payload fraction for rocket SSTO

altitude, the change of velocity to be inserted into Equation 4.18 is calculated by simplifying

the ascent trajectory with a Hohmann transfer[1]. This is an assumption not verifiable for several reasons: (1) related to dynamic pressure $\frac{1}{2}\rho V^2$, which is directly proportional to aerodynamic forces, so if ρ is high (low altitude), then V cannot be excessive, and therefore the initial Hohmann velocity cannot be reached; (2) related to heat flux, which also limits the speed where density is high; (3) related to the prohibition of flying near inhabited areas at low altitudes. Nevertheless, it represents a conservative formulation of how ΔV varies with altitude and it is adopted here for simplicity.
From Figure 4.14a, it can be observed that even with the LOX/LH2 propellant combination, which ensures the highest I_{sp}, the maximum achievable change in velocity with a SSTO rocket is approximately km/s. Furthermore, this result corresponds to a payload mass m_u of zero; therefore, to ensure the concreteness of the mission, even lower ΔV values must be considered. A similar discussion applies to what is shown in Figure 4.14b, where it can be seen that not even reaching VLEO orbits is guaranteed. This demonstrates that a SSTO space access mission with single-stage rockets is not feasible.

4.2 Combined-Cycle Engines

Combined-cycle engines are propulsion systems capable of operating in various modes, integrating multiple engine cycles into a single propulsion system and transitioning from one propulsive method to another under specific Mach number and altitude conditions. These propulsion systems offer a potential alternative for space access compared to current multi-stage rockets. To ensure space access through reusable spaceplanes, it is imperative that the final phase of ascent, where the air becomes excessively rarefied for airbreathing propulsion, is executed using rocket-mode propulsion.

The following outlines the primary categories of Combined-Cycle Engines.

4.2.1 Liquid Air Cycle

Liquid Air Cycle Engines (LACE) have the peculiarity of leveraging the cooling capacity of cryogenic liquid hydrogen to liquefy the atmospheric air. These engines integrate air-breathing technology with conventional rockets by utilizing liquid hydrogen as the fuel, which is burned within a combustion chamber. The oxidizer required for combustion is sourced directly from the atmosphere, exchanging heat with the liquid hydrogen that has been pumped into a precooler and a condenser. The process allows air to be liquefied, which is then pumped into the combustion chamber where it burns with hydrogen from the cooling jacket, similar to conventional liquid rocket engines. Then, hot gases are expanded into a supersonic nozzle. These propulsion systems offer the following advantages:

[1]The Hohmann transfer is a minimum-energy transfer between two coplanar circular orbits. The transfer is accomplished by applying two impulses, one to raise the perigee of the initial orbit to the radius of the desired circular orbit, and the other to lower the apogee of the resulting elliptical orbit to the radius of the desired circular orbit. [38]

- Compared to rockets, they utilize oxygen directly from the atmosphere for combustion, eliminating the need to carry it in tanks;
- In contrast to turbojets/turbofans, they mitigate issues associated with high temperatures at high Mach numbers, and significantly reduce compression costs, enabling a higher pressure ratio.

A more advanced iteration of the LACE, known as the Air Collection Enrichment (ACE) system, integrates a liquid oxygen separator following the liquefaction process. This feature enables the simultaneous provision of fuel to the rocket's combustion chamber and the replenishment of oxidizer tanks while the rocket ascends using air-breathing propulsion.

Neither traditional LACE nor ACE technologies prove optimal for a SSTO launcher due to their significant fuel consumption. At sea level, basic LACE demands fuel-air ratios up to eight times higher than stoichiometric levels for efficient air cooling. Moreover, the intricate technological nature of these systems fails to offset the marginal increase in specific impulse compared to conventional thermochemical rockets [24].

4.2.2 Turbine-Based Combined Cycle

Turbine-Based Combined Cycle (TBCC) engines utilizes an high specific impulse turbine-based engine for accelerating the vehicle from take-off until it reaches the mode transition flight conditions (Mach number about 3). At this point, the propulsion system switches from the turbine to a dual-mode scramjet engine, where the incoming airflow is redirected to bypass the turbojet section, utilizing the compression effect induced by the duct's geometry.

Various architectures have been suggested for TBCC engines: the simplest one involves separate flow paths for distinct operating modes, which notably adds to the overall weight of the engine; alternatively, other configurations aim to merge the turbojet and the dual-mode ramjet-scramjet subsystem within a single airflow path, incorporating specific devices capable of redirecting the airflow towards the appropriate subsystem based on prevailing flight conditions.

Figure 4.15 reports a representation of a Turbine-Based Combined Cycle (TBCC) engine.

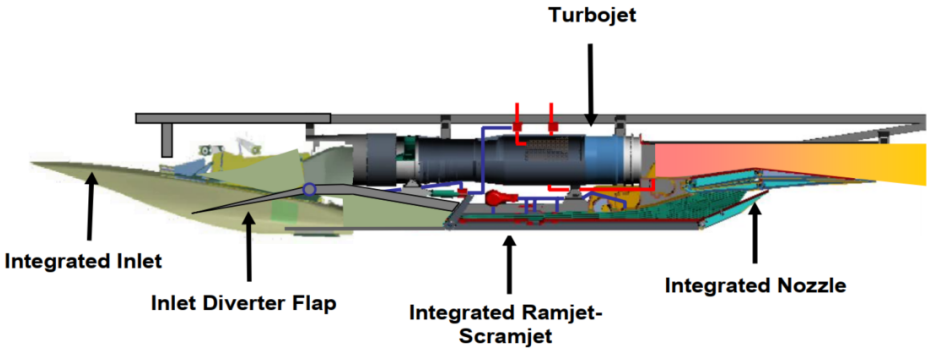

Figure 4.15: A Turbine-Based Combined Cycle (TBCC) engine configuration [16]

4.2.3 Rocket-Based Combined Cycle

Rocket-Based Combined Cycle (RBCC) engines combine airbreathing engine technology with rocket propulsion elements, forming a singular integrated engine capable of multi-mode operation, suitable for use from ground take-off up to orbit. The rocket engine is utilized to generate thrust under static conditions for the initial flight phase, operating as an ejector rocket from take-off until reaching supersonic speeds. Once a Mach number ranging between 2 and 3 is attained, the dual-mode scramjet subsystem is engaged. Initially, this subsystem functions in ramjet mode, accelerating until reaching approximately Mach 5 or 6, where the transition to scramjet mode occurs. In this propulsion mode, external air is compressed and decelerated through a series of shocks within the inlet, the design of which was conducted in section 4.4. Upon reaching a flight Mach number ranging between 10 and 12, when an altitude where the air is too thin to allow an airbreathing device to work properly is reached, RBCC engines close the inlet and work as a pure rocket, allowing the vehicle to reach orbit.
Two types of RBCC engines can be identified:

- Axisymmetric configuration engines: the rocket is positioned along the central axis, configured as a conical rocket installation (figure 4.16a);
- Rectangular section engines: configuration more similar to scramjet, which enables integration of the inlet with the vehicle body, as well as the nozzle. This design leverages the advantageous effects of forebody compression and afterbody expansion of the flow entering and exiting the engine, like in strut-jets [40] (figure 4.16b).

Rocket-Based Combined Cycle engines allow both horizontal and vertical take off, due to the substantial thrust generated by the rocket during the initial acceleration phase. This type of engines represent an optimal candidate for SSTO LEO missions [24].

Ejector Rocket

In the first phase of the flight, from take off to the ideal ramjet conditions (Mach number about 3), a Rocket-Based Combined Cycle engine can operate in Ejector Rocket mode. In the rocket-ejector mode, the engine operates on an ejector cycle where the rocket functions as the primary or drive-jet. This mode enhances the thrust of the rocket through a jet pumping process, which transfers momentum from the high-velocity rocket exhaust to the ingested air. The ejector process increases the total mass flow while reducing the exit velocity, resulting in a higher specific impulse compared to rocket-only operation.

4.2.4 Precooled Hybrid Airbreathing-Rocket Engines

Precooled Hybrid Airbreathing-Rocket engines represent a type of propulsion system currently undergoing research and experimentation. They are capable of integrating air-breathing and rocket propulsion in two distinct phases of the mission, utilizing the same combustion chamber and nozzle. These engines can be viewed as an evolution of LACE engines; however, instead of liquefying external air, they utilize high-pressure hydrogen to cool the flow. The fuel flow is

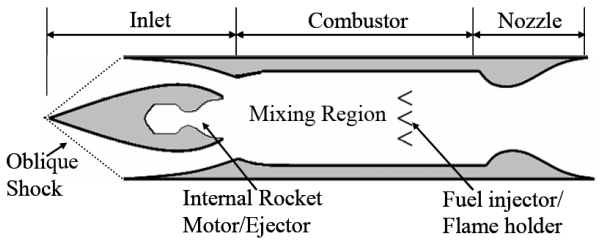

(a) Axisymmetric configuration engine [39]

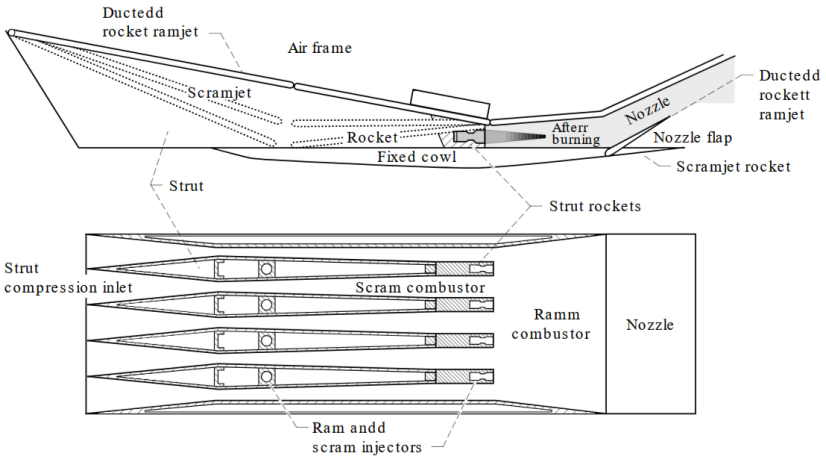

(b) Rectangular section engine [40]

Figure 4.16: Rocket-Based Combined Cycle (RBCC) configurations

then divided into two separate streams: two-thirds of the available flow is directed to expand in a turbine to generate power for the compressor, while the remaining hydrogen is injected into the combustion chamber.

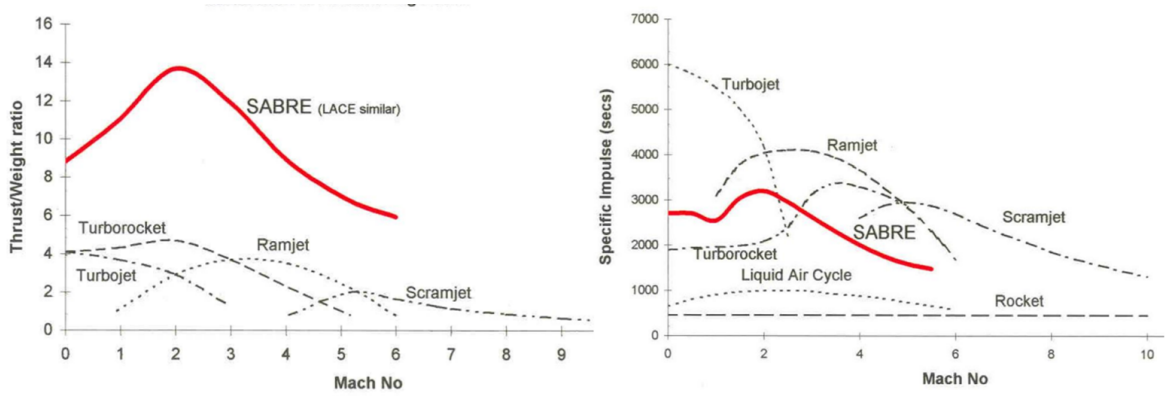

Figure 4.17: Variation with Mach number of thrust–weight ratio and specific impulse of the SABRE [17]

The Synergetic Air-Breathing Rocket Engine (SABRE) is a hybrid air-breathing rocket engine developed by Reaction Engines Ltd., designed as propulsion system of the SKYLON spaceplane. A detailed description of this propulsive unit is reported in section 2.2, while in figure 4.17 the SABRE performance are reported.

4.2.5 Resume

A summary of the thrust or specific thrust formulations found for the various propulsion modes is given in table 4.3.

TBCC		**Turbojet**	$\frac{\mathcal{T}}{\dot{m}_a} = [(1+f)w_e - u]$
		Turbofan	$\frac{\mathcal{T}}{\dot{m}_a} = (1+f)w_e + \mu \cdot w_{e_f} - (1+\mu)u$
	RBCC[2]	**Ramjet**	$\frac{\mathcal{T}}{\dot{m}_a} = \mathrm{M}\sqrt{\gamma R T_a}\left[(1+f)\sqrt{T_{04}/T_a}\left(1+\frac{\gamma-1}{2}\mathrm{M}^2\right)^{-1/2} - 1\right]$
		Scramjet	$\frac{\mathcal{T}}{\dot{m}_a} = \mathrm{M}\sqrt{\gamma R T_a}\left\{\sqrt{\eta_{\mathrm{KEO}}\ (1+f)\left[1+\frac{\eta_b\ f\ H_i}{c_p T_a(1+((\gamma-1)/2)M^2)}\right]} - 1\right\}$
		Rocket	$\mathcal{T} = \dot{m}\ w_e + A_e\,(p_e - p_o)$

Table 4.3: Resume of thrust or specific thrust formulations found for the various propulsion modes

4.3 Transition Mach numbers

Once the main propulsion strategies for the ascent to orbit of a SSTO vehicle were studied, implementing a propulsion modelling into the sizing code required analyzing the transition conditions between propulsion systems (modes) and their subsequent counterparts. To separate this analysis from specific mission details, the transition altitude was disregarded, and the flight Mach number was considered as the reference parameter for the propulsion mode switch. In this regard, an in-depth literature review was conducted.

Turbojet-Ramjet transition

The transition from turbine mode to ramjet mode is a key process in TBCC engines. Turbojet-to-ramjet transition has been recognized as a critical regime in TBCC operations, pivotal for the successful functioning of the combined cycle system, due to the insurrection of the *thrust trap* problem. In fact, the mode-transition point typically occurs at the upper limit

[2]The RBCC also includes the ejector rocket propulsion mode, considered here as a variation of the rocket

of the turbojet engine's working Mach number and the lower limit of the ramjet engine's Mach number, a transition process can lead to an imbalance between thrust and drag. This imbalance may result in continued deceleration of the aircraft and the inability to establish suitable flow conditions for the normal start of the ramjet engine. Typical transition Mach number values are in the $2.5 \div 3.5$ range. Some solutions have been proposed to deal with the thrust trap: for example, a possible solution is in an Thrust Augmentation Control Schedule, with early opening ramjet by-pass (at Mach number 2.2) [18], as shown in figure 4.18.

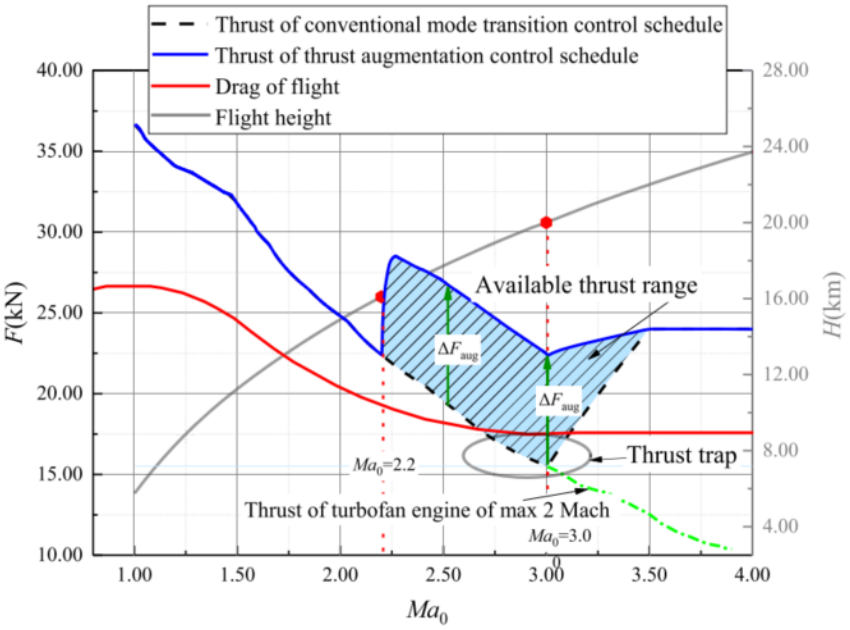

Figure 4.18: Thrust augmentation control schedule adopted for the turbojet-to-ramjet transition [18]

Ramjet-Scramjet transition

The transition from ramjet mode to scramjet mode of a dual-mode scramjet is fundamental for both TBCC and RBCC engines. As can be seen from Figure 4.3, the specific impulse I_{sp} of the ramjet is higher than that of the scramjet, resulting in lower fuel consumption. Ideally, the ramjet mode should be utilized for as long as possible. The transition in combustion mode within a dual-mode scramjet engine should occur within the Mach number range of $6 \div 7$. If ramjet and scramjet are modelled using ideal thermodynamic cycles, as reported in [41], a maximum Mach number for the ramjet engine can be identified, which can be taken as the transition value:

$$M_0^* = \sqrt{\frac{1}{\gamma - 1}\left[(\gamma + 1)\frac{T_{\max}}{T_0} - 2\right]} \tag{4.19}$$

Scramjet-Rocket transition

When the flight Mach number become greater than 10-12, transition from scramjet to rocket mode become necessary. In fact, as the air density diminishes beyond the point where sustaining an efficient airbreathing cycle becomes unfeasible, the engine transitions to pure-rocket operation. The air inlet is closed, and the rocket is reignited to supply thrust, facilitating the spacecraft's insertion into orbit.
Scramjet-Rocket transition takes place at flight Mach number between 10 and 15, as can be seen in figure 4.19.

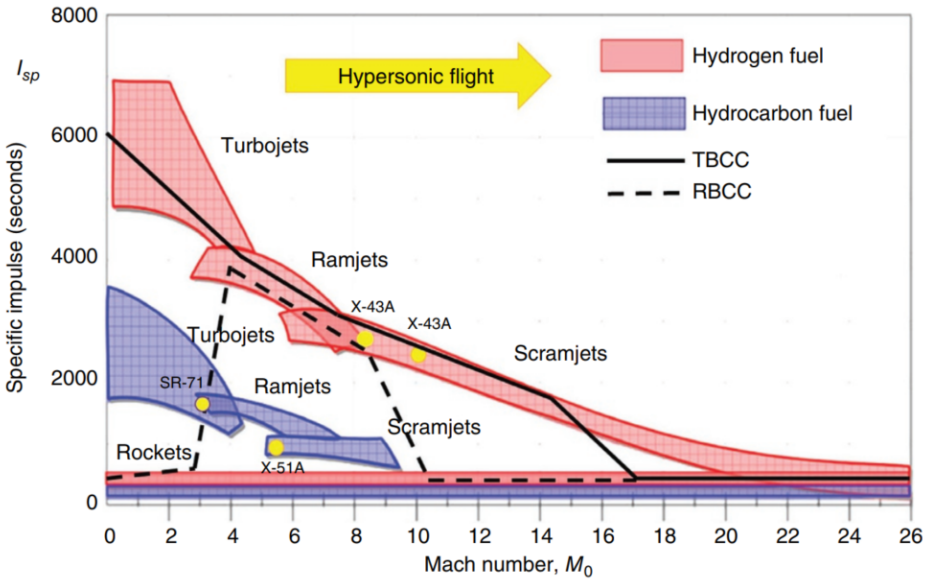

Figure 4.19: Combined-Cycle Engines: transition between propulsive modes [14]

Ejector-Ramjet transition

The transition from ejector-rocket mode to ramjet mode is a crucial process in RBCC engines. This transition should occur at a flight Mach number ranging between 2 and 3. The ejector-ramjet transition can occur in two commonly used ways:

- *"Range-type" transition*: the mode transition is accomplished in a small Mach number range. In this case, during the initial operation of the engine in the ejector-rocket mode, the embedded rockets were gradually throttled down prior to transitioning to ramjet operation. Just before the rockets were shut down, the downstream ram fuel was significantly increased. Subsequently, the engine thrust decreased before stabilizing at an approximately constant ramjet thrust.

- *"Point-type" transition*: the mode transition happens at a certain flight Mach number. For example, for the hydrogen-fueled Strutjet engine designed for space launch propulsion, the transition was chosen to be fulfilled at Mach 2.4; the embedded rockets were

turned off directly before the ramjet fuel and the engine transited naturally to the sustained ramjet operation and, subsequently, the Strutjet engine operated smoothly in the ramjet mode.

4.4 Implementation: Statistical Analysis and Inlet Sizing

Once the potential propulsion technologies for the ascent phase of a Single-Stage-To-Orbit aircraft were identified, and after studying the analytical formulations of thrust or specific thrust, as well as the transition conditions between the various propulsion modes of combined-cycle engines, a statistical analysis of thrust became necessary. The purpose of this analysis is to incorporate statistical thrust values into the first loop of the iterative convergence process. While a considerable amount of data is available for turbojet/turbofan and rocket engines due to their widespread use, the same cannot be said for ramjet and scramjet engines used in combined-cycle engines, which are mostly in the developmental phase currently. For this reason, the statistical analysis reported here is limited to this type of propulsion system.

Table 4.4 presents the reference statistical database for ramjet engines.

Vehicle	**Thrust [N]**	**Other PSs**	**MTOW [kg]**
CIM-10 Bomarc	53366	rocket	7250
Focke-Wulf Ta 283	11772	rocket*	5450
Leduc 0.10	15700	-*	3000
Leduc 0.21	64000	-*	6000
Leduc 0.22	63600	turbojet	8975
Lockheed AQM-60 Kingfisher	51000	rocket	3600
Lockheed D-21	7300	-*	4990
Nord 1500-2 Griffon II	67800	turbojet	6745
North American MQM-42	8000	rocket	408
Convair Kingfish	44500	turboramjet	9692

Table 4.4: Statistical database of ramjet engines ('*' indicates that the vehicle is launched from an aircraft or has a secondary propulsion system for take-off support)

The graph in figure 4.20 reports the statistical curve for the thrust of ramjet engines. Subsequently, starting from the specific thrust formulations of dual-mode scramjets reported earlier, calculating thrust requires determining the airflow entering the engine. To evaluate this, sizing the inlet became necessary. For simplicity, the inlet was considered to have constant geometry, thus varying the airflow based on flight conditions. The inlet sizing followed the procedure outlined in [11] for a supersonic inlet with a prominent flat ramp, similar to the one

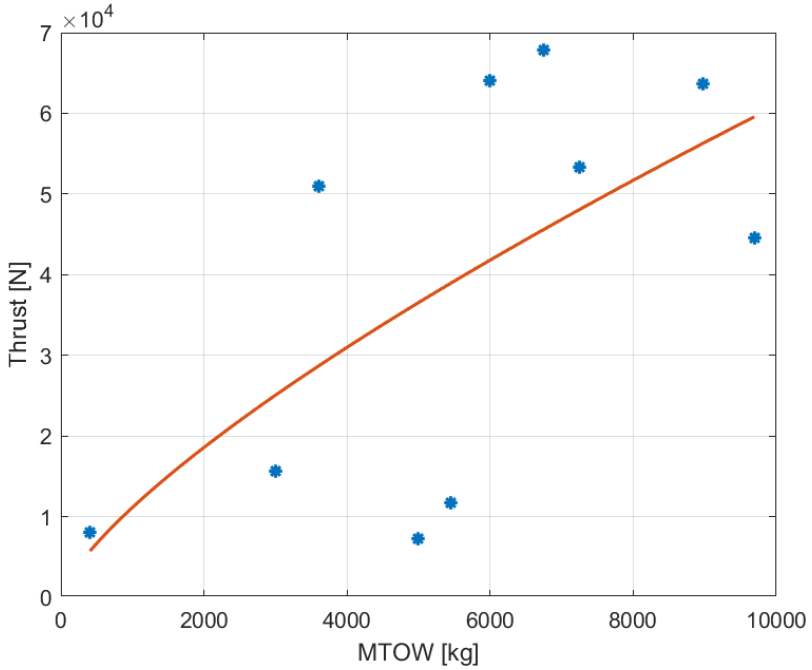

Figure 4.20: Statistical analysis of the ramjet engine's thrust

shown in Figure 4.21. Under on-design conditions, the oblique shock encounters the inlet lip. Initially, a single-ramp inlet was sized, which entails the occurrence of an oblique shock and a

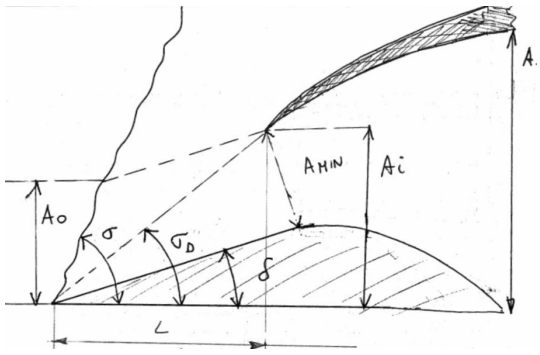

Figure 4.21: Supersonic air intake with prominent flat ramp [11]

normal shock in the inlet throat (see figure 4.21). However, initial analyses revealed that the total pressure ratio (or Ram Efficiency) is very low for high Mach number values typical of dual-mode scramjet operation. Therefore, a multi-ramp inlet is evaluated. With three ramps, the obtained Ram Efficiency values were significantly improved and consistent with those of real inlets (see figure 4.22).

For this purpose, a MATLAB function has been created.

```
[eps_d,Amin,Ai]=SupersonicInletSizing(M,h,delta1,delta2,delta3)
```

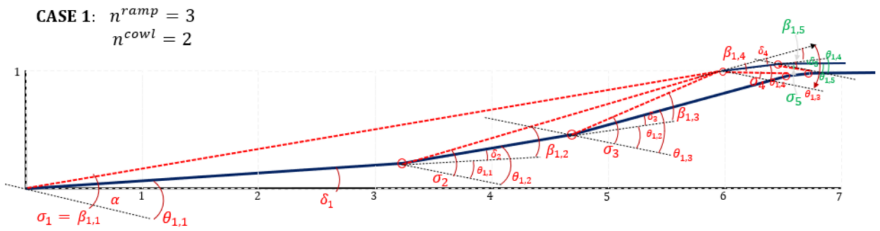

Figure 4.22: Supersonic air intake with prominent flat ramp with three ramps [19]

To be implemented into the sizing code, this function takes as input the flight Mach number, altitude, and the values of the three ramp angles. If the latter are omitted (*null* input), the function uses three reference values [19]. If fewer ramps are desired, the last (or last) input angles can be set to zero (for example, if you want to size an inlet with two ramps, delta3 should be set to zero). The outputs of this function are the Ram Efficiency ε_d, the minimum area at the throat A_{min}, and the inlet area (or exit area of the inlet) A_i, concerning figure 4.21. In appendix A the entire MATLAB function is reported.

Chapter 5

Matching Chart Analysis

In this chapter, the Matching Chart tool is revised to extend its applicability beyond the aeronautical sector, including access to space missions. The Matching Chart (MC) tool was introduced by NASA in the 1980s, a simple way of representing propulsion system requirements matching with the vehicle configuration. It involves a graphical representation that correlates thrust-to-weight ratio (T/W) with wing loading (W/S) on a 2D chart. This chart enables the identification of a feasible design space and the determination of a design point, describing the optimal vehicle configuration in terms of maximum thrust, maximum take-off weight (MTOW), and wing surface while meeting all high-level requirements. In figure 5.1 is reported an example of Matching Chart for a commercial aircraft.

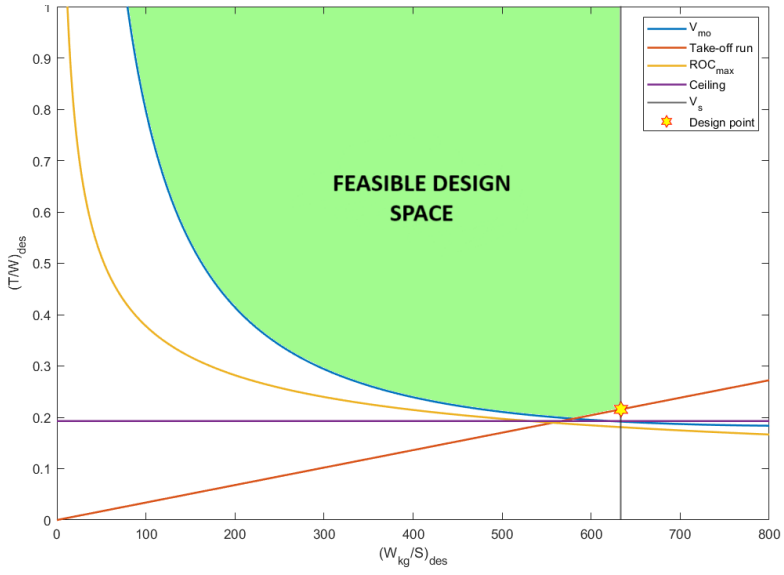

Figure 5.1: Example of Matching Chart for a commercial aircraft

To extend the MC tool to space access applications, the Multiple Matching Charts (MMC) tool approach is utilized and upgraded, adding a new requirement representing the minimum thrust-weight ratio as a function of wing loading necessary to reach the target orbit.

Firstly, the requirements of the reusable SSTO vehicle ascent phase are identified. Then, is presented the application of the latter to the reaching orbit requirement, where an analytical retraction of the Rocket Equation is made to express the thrust-to-weight ratio (T/W) as a function of the wing loading (W/S). Graphical results are then reported.

5.1 Ascent High-Level Requirements

Here are reported the main high-level requirements for the ascent phase of a reusable SSTO launcher, which represents the target of this thesis. Focusing on HTOL vehicles, the following requirements can be identified:

1. Full reusability;
2. Horizontal take-off and landing;
3. Single stage;
4. Minimising fuel consumption;
5. Operation in different atmospheric conditions;
6. Compliance with safety and emission standards;
7. Reaching target orbit.

In terms of operation, the above requirements can be translated as follows:

Maximum payload mass	m_{pay} [kg]
Maximum Mach number	M_{max} [ ]
Rate of Climb	ROC [m/s]
Orbit altitude	h [m]
Change in velocity	ΔV [m/s]

Table 5.1: Operational requirements for a SSTO HTOL vehicle

5.2 Orbit Reaching Requirement

The objective of this activity is to extend the applicability of the Matching Chart (MC) tool to reusable launchers, i.e. to find a formulation of T/W as a function of wing loading W/S from the requirements of this type of aircraft. What distinguishes the latter from conventional aircraft is the fact that they must access space and thus reach orbital speeds. For this reason, to apply the MC to the conceptual design of these, we focused on the requirement to reach orbit, making use of the Multiple Matching Charts (MMC) approach described below.

5.2.1 Multiple Matching Charts

The Multiple Matching Charts (MMC) approach is designed to overcome the issues that arise when applying the MC tool to hypersonic vehicles. These issues come up because the conventional tool is unable to handle complex propulsion systems that change operational modes, as seen in hypersonic vehicles (and reusable launchers). Additionally, normalizing engine thrust using a single reference point (such as sea level) is misleading for high-speed vehicles due to varying atmospheric conditions across flight regimes. Finally, considering a single design point for the entire mission of this type can lead to inaccurate results.

The MMC design methodology proposed in [42] overcomes the issues described. It allows the analysis of each flight regime (subsonic, supersonic, hypersonic) separately through different charts to assess performance needs, imposing a consistency requirement due to the fixed size of the wing surface. Each regime will have a "local design point" based on its specific needs for wing size and thrust and the consistency of the wing surface is determined by the most demanding condition. The MMC approach allows the identification of a "global design point" that reflects the final wing size and the highest required thrust across all regimes (see figure 5.2).

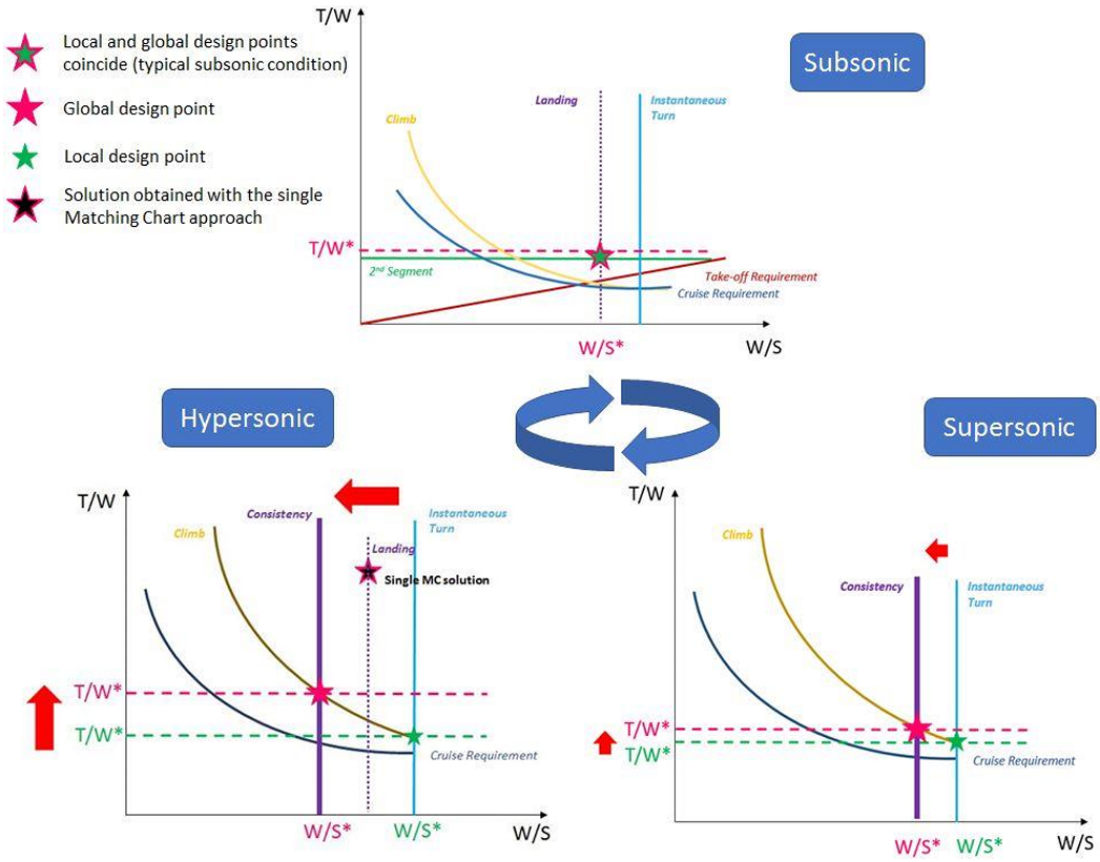

Figure 5.2: Example of Multiple Matching Charts approach

5.2.2 Analytical formulation

To identify a formulation of the thrust-to-weight ratio (T/W) as a function of the wing loading (W/S) to be inserted into the MC tool for the orbit attainment requirement, the proposed treatment start from the Rocket Equation:

$$\Delta V = I_{\text{sp}} \ \cdot g_0 \cdot \ln\left(\frac{W_i}{W_f}\right) \tag{5.1}$$

where, denoting by $\dot{W}_{\text{ppl}}$ the propellant mass flow rate, the specific impulse can be expressed as follows:

$$I_{sp} = \frac{T\ g_0}{\dot{W}_{\text{ppl}}\ g_0} = \frac{T\ g_0}{\frac{W_{\text{ppl}}}{t_b} g_0} \tag{5.2}$$

where $t_b = \text{ROC}/h$ is the burning time. The thrust T is multiplied by g_0 to express it in kilograms (in this discussion forces and weights have kilogram units). Returning to the rocket equation and multiplying and dividing by W gives:

$$\Delta V = \frac{T}{W}\frac{W}{W_{\text{ppl}}}\ t_b\ g_0\ \ln\left(\frac{W_i}{W_i - W_{\text{ppl}}}\right) \tag{5.3}$$

from which can be isolated the thrust-to-weight ratio

$$\frac{T}{W} = \frac{W_{\text{ppl}}}{W}\frac{\Delta V\ g_0}{t_b\ \ln\left(\frac{W_i}{W_i - W_{\text{ppl}}}\right)}\ . \tag{5.4}$$

At this point, it is considered a semi-empirical formulation of the Propulsion Index given in [5], which expresses it as a function of the maximum Mach number attainable with the propulsion system used:

$$I_P = \frac{\rho_{\text{ppl}}}{\text{WR} - 1} = 107.6 \cdot 10^{-0.081 \cdot M_{\max}} \tag{5.5}$$

where WR= W_i/W_f represents the weight-ratio, which can be written as follows:

$$\text{WR} - 1 = \frac{W_{\text{ppl}}}{W_f}\ . \tag{5.6}$$

Combining the last two equations yields a formulation for the weight of the propellant:

$$W_{\text{ppl}} = \frac{\rho_{\text{ppl}} \cdot W_f}{I_P} \tag{5.7}$$

Referring to [5], a formulation of the planform surface S_{pln} is used:

$$S_{pln} = \left[\frac{I_p}{I_{str}} \cdot \frac{K_w}{\tau} \cdot \frac{1}{K_v} \cdot \frac{1}{K_{str}} \cdot \left(1 + \frac{W_{\text{pay}}}{W_f}\right)\right]^{1.409} \tag{5.8}$$

in which the parameters appearing are made explicit in appendix B and from which the final weight W_f can be isolated and substituted into the equation 5.7.

$$W_{\text{ppl}} = \frac{W_{\text{pay}}\ \rho_{ppl}\ K_w}{S_{pln}^{0.71}\ I_{str}\ \tau\ K_v\ K_{str} - I_p\ K_w} \tag{5.9}$$

Multiplying and dividing by $W^{0.71}$ gives:

$$W_{\text{ppl}} = \frac{\rho_{\text{ppl}}\ W_{\text{pay}}\ K_W}{(W/S)^{-0.71}\ W^{0.71}\ a - b} \tag{5.10}$$

where parameters a and b are defined as follows:

$$\begin{cases} a = I_{str} \cdot \tau \cdot K_v \cdot K_{str} \\ b = I_p \cdot K_w \end{cases} \tag{5.11}$$

Finally, substituting the $W_{textppl}$ found (eq.5.10) into the equation 5.4 yields:

$$\frac{T}{W} = \frac{\rho_{\text{ppl}}\ W_{pay}\ K_W}{(W/S)^{-0.71}\ W^{1.71}\ a - W\ b} \cdot \frac{\Delta V}{g_0\ t_b\ \ln\left(W \Big/ \left(W - \frac{\rho_{\text{ppl}}\ W_{\text{pay}}\ K_W}{(W/S)^{-0.71}\ W^{0.71}\ a\ -\ b}\right)\right)} \tag{5.12}$$

which represents a new formulation of the thrust-to-weight (T/W) ratio as a function of wing weight-ratio (W/S), referring to the orbit reaching requirement. This is designed to be applied to each mission phase, using the Multiple Matching Charts approach.

5.2.3 Results

The practical results of the newly developed formulation are now presented. For this purpose, a MATLAB function was created

```
[T_W] = orbitReachingReq(tau,W,W_pay,Mmax,h,ROC,Istr,rho_pay,DV)
```

which takes the following parameters as input

tau	Küchemann parameter τ [5]
W	Maximum Take-Off Weight
W_pay	Payload mass
Mmax	Maximum Mach number (of the phase)
h	Maximum altitude (of the phase)
ROC	Rate Of Climb (of the phase)
Istr	Structural index [5]
rho_pay	Payload mean density
DV	Change in velocity (of the phase)

Table 5.2: Input of the orbit reaching requirement function

and returns as output a function handle of the T/W as a function of the W/S. In appendix A the entire MATLAB function is reported.

Figure 5.3 presents the graph resulting from the application of the requirement to the first phase of SKYLON (airbreathing phase). It can be seen how the formulation developed for the requirement translates into a plausible curve (see the MC example shown in Figure 5.1), which will have to be inserted into the MC together with the curves representing the other requirements to identify a feasibility area. It is noted that the thrust-to-weight ratio values obtained are relatively low for this phase, concluding that this requirement is not a sizing factor for the airbreathing ascent.

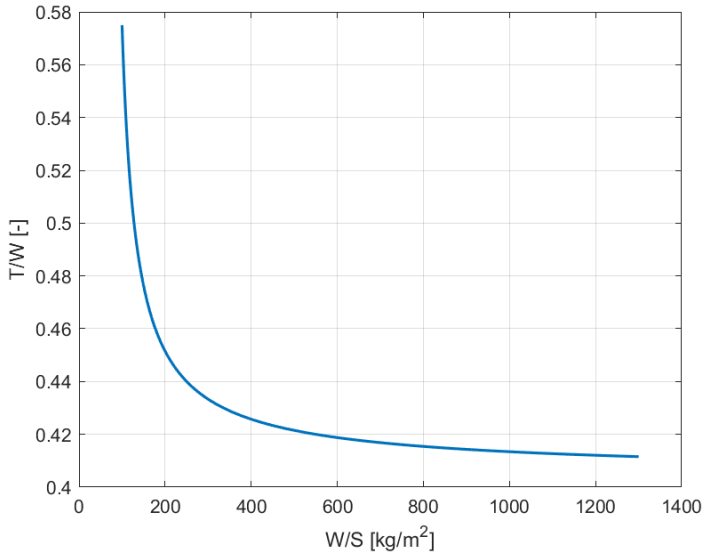

Figure 5.3: Orbit reaching requirement curve for the **airbreathing** phase

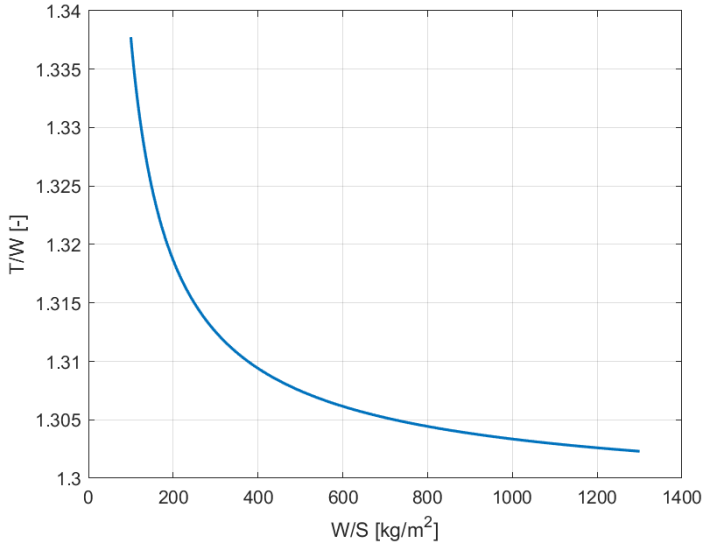

Figure 5.4: Orbit reaching requirement curve for the **rocket** phase

To apply the formulation to the rocket phase of SKYLON, it was necessary to modify the propulsion index. This is because the semi-empirical formulation of I_P reported in [5] (see Eq. 5.5) was found to be unsuitable for describing this propulsion mode, as it is probably related to airbreathing engines and is also quite dated. To overcome this problem, the propulsion index was expressed in terms of propellant density and weight ratio WR. The latter was estimated to be around 4.5 for the rocket phase. Figure 5.4 shows the curve obtained for SKYLON.
As can be seen, in this phase the thrust-to-weight ratio assumes significantly higher values, of the order of 1.3, which are justified for the rocket phase.

Below, in figure 5.5, the complete graphs (containing all the requirements) of the MMC referring to SKYLON, developed by Tommaso Molinari [43] (see the organizational chart in figure 1.9) for testing the methodology, are presented. As previously mentioned, for the airbreathing phase, the curves related to the orbit attainment requirement are not influential for the calculation of the design point; conversely, for the rocket phase, this requirement is dimensioning the thrust-to-weight ratio.

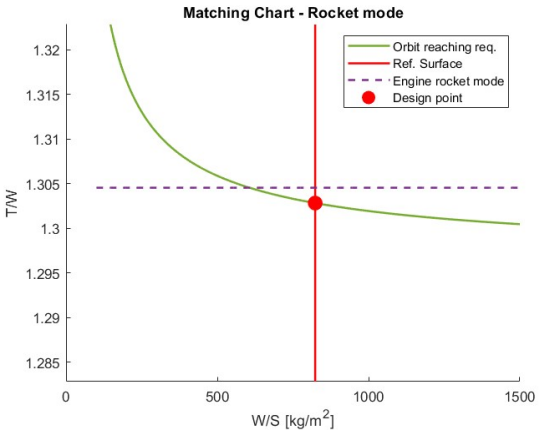

(a) Turbine mode

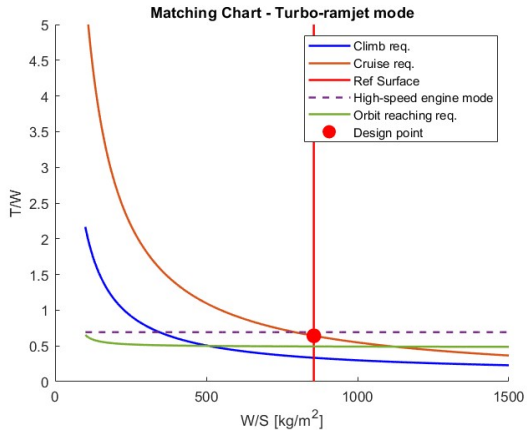

(b) Turbo-ramjet mode

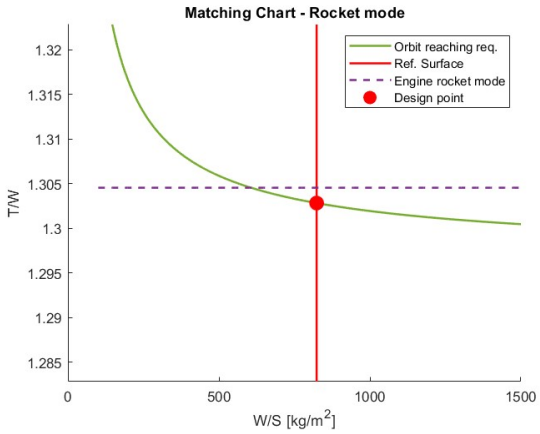

(c) Rocket mode

Figure 5.5: Multiple Matching Charts (MMC) of the case study SKYLON

Chapter 6

Mission Analysis

This chapter present mission analysis in nominal and out-of-nominal conditions. For this purpose, the commercial software ASTOS[1] (Aerospace Trajectory Optimization Software) is used. The purpose of the mission analyses presented is to verify the consistency of the data obtained from the developed conceptual design methodology. Specifically, the methodology is applied to the case study, and for the mission analysis using ASTOS, the masses (empty mass and propellant mass) obtained from the sizing code developed were incorporated. The achieved results are then verified and compared with the case study. As stated in Chapter 2, the applied case study is the SKYLON spaceplane, currently under development by the British company Reaction Engines Limited. Since SKYLON is currently a concept vehicle of

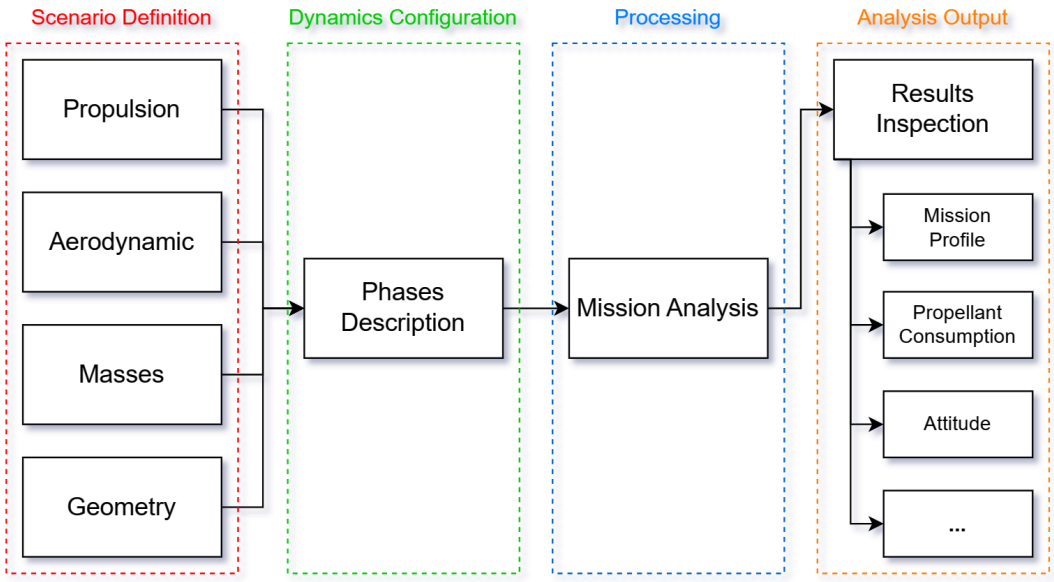

Figure 6.1: Scheme of mission analysis procedure through ASTOS

[1]ASTOS is a tool dedicated to mission analysis, trajectory optimization, vehicle design and simulation for space scenarios, i.e. launch, re-entry missions, orbit transfers, Earth observation, navigation, coverage and re-entry safety assessments. (source: Wikipedia)

a private company, publicly available data is quite limited. For this reason, to characterize the geometry, aerodynamics, and propulsion of SKYLON, reference is mainly made to test articles and analyses of the spaceplane in question, as well as the SKYLON User's Manual [2]. In the scheme of figure 6.1 is presented the mission analysis procedure through ASTOS.

6.1 Mission Definition

Below is the mission definition in ASTOS, where a scenario is created through the characterization of aerodynamics, propulsion, geometry, and weights followed by the dynamic configuration through the definition of the various phases. Remembering that the ultimate goal is to verify the results of the methodology developed for conceptual design, the masses entered are derived from the sizing code of the tool, while the other aforementioned inputs come from official SKYLON data or studies conducted by third parts.

Aerodynamic

The aerodynamic data entered in ASTOS define the lift and drag coefficients of SKYLON as a function of flight Mach number and angle of attack α. They are divided into two different databases, one related to the airbreathing phase up to approximately Mach 5, and one concerning hypersonic aerodynamics corresponding to the rocket phase.

The data for the airbreathing phase are derived from CFD analyses conducted on a scale model of SKYLON within the project MORE&LESS of Politecnico di Torino. In this case, the aerodynamic coefficients are expressed as functions of Mach number and angle of attack, as shown in figure 6.2.
For higher Mach numbers, including the rocket phase of the SKYLON, the aerodynamic coefficients are taken from [20], an independent partial assessment conducted by the NASA Ames Research Center to evaluate the technical feasibility of the Skylon aerospace plane concept. In this study, the contribution to the coefficients due to the interaction of the plume with the spaceplane is considered, which represents a positive contribution (increase in lift

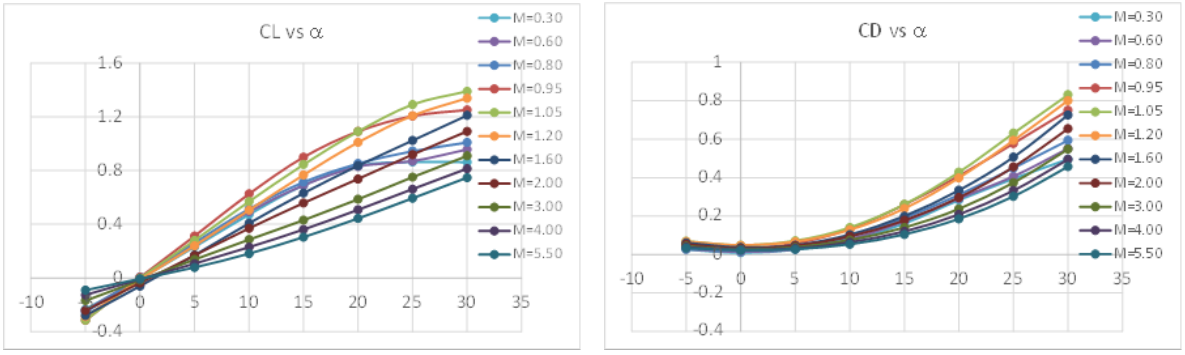

(a) Lift coefficient (b) Drag coefficient

Figure 6.2: SKYLON aerodynamic data for the air-breathing phase

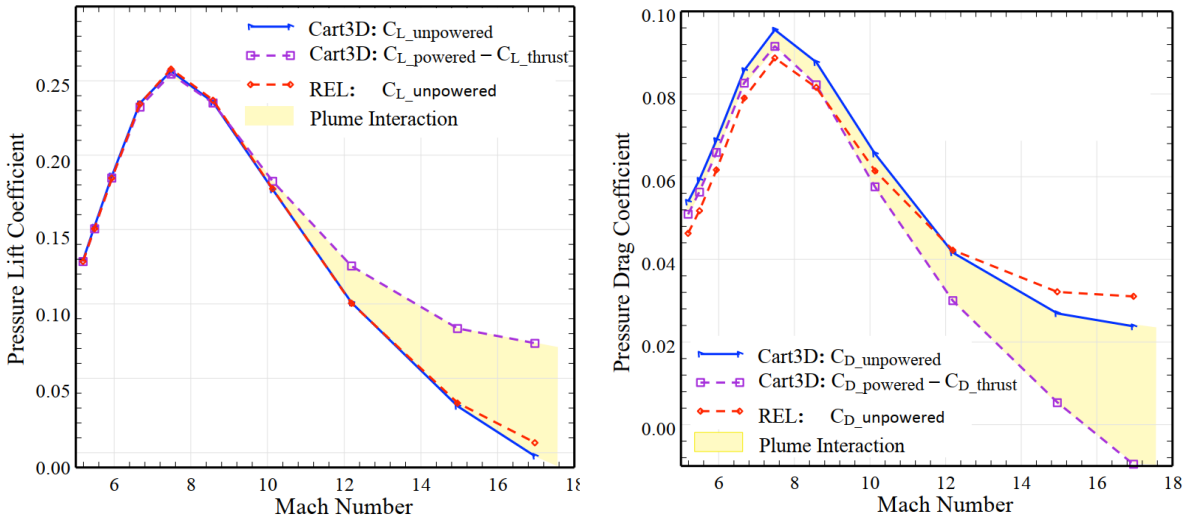

(a) Lift coefficient (b) Drag coefficient

Figure 6.3: SKYLON aerodynamic data for the hypersonic phase comprehending rocket [20]

coefficient and decrease in drag coefficient, see the purple curves in figure 6.3). Only in the case of the drag coefficient, for conservatism, it was decided not to consider the plume interaction (blue curve).

As a Reference Area for the calculation of aerodynamic forces, a wing area of 345.77 m^2 was entered, calculated from the measurements of SKYLON provided in the SKYLON User's Manual [2]. In appendix C the complete aerodynamic database used is reported.

Propulsion

For the propulsion characterization, real data from the SABRE engine provided by Reaction Engines Ltd. are adopted.

Specifically, for the air-breathing phase, both the gross thrust T_g and the uninstalled thrust T_u are available as functions of flight Mach number. The former considers the engine thrust values without accounting for any losses due to the aerodynamic resistance of the aircraft itself, while the latter is the thrust derived from ground tests of the engine considering aerodynamic resistance but without installation on the aircraft. The complete data are reported in Appendix C. To model the thrust of the two SABRE engines in ASTOS, it is chosen to use the uninstalled thrust T_u as it is more realistically close to the in-flight thrust of SKYLON. As the fuel mass flow rate is required, the $\dot{m}_f$ profile as a function of Mach number relative to the SABRE model developed in [3] is inserted.

To properly model the rocket-propelled phase, a new propulsion system (termed as an "actuator" in ASTOS) capable of providing constant thrust equal to $T = 2000\ kN$ with a mass flow rate of $\dot{m}_f = 416.8\ kg/s$ was created (see SKYLON User's Manual [2]). Although the rocket is a mode of operation of the SABRE engine and not a separate propulsion system, creating a separate actuator is necessary to better model the propulsion phase within the

software without causing compatibility issues with the data.

Table 6.1 provides the input data for the propulsive characterization of the case study, for both the air-breathing and rocket modes of the SABRE engine.

Propulsive mode	**Mach range**	**Thrust [kN]**	**Fuel flow rate [kg/s]**
Air-breathing	0 - 5	1224 - 884 [2]	10.3 - 11.7
Rocket	5 - 25	2000	416.8

Table 6.1: Input data for the propulsive characterization of SKYLON in ASTOS

Geometry

The definition of the SKYLON geometry in ASTOS is not a crucial step for the mission analysis, except for the stability of the aircraft, which is neglected in this initial phase of conceptual design. Therefore, SKYLON is modeled with two parallelepiped-shaped components, representing the structure of the spaceplane and the payload bay. The dimensions of these components are listed in Table 6.2.

	X [m]	**Y [m]**	**Z [m]**
Structure	83.13	26.82	13.50
Payload bay	13.00	4.80	4.85

Table 6.2: Geometrical description of SKYLON in ASTOS

In figure 6.4 is shown the obtained geometry, with the payload bay at the center of the main structure, and the two engines on the sides centrally.

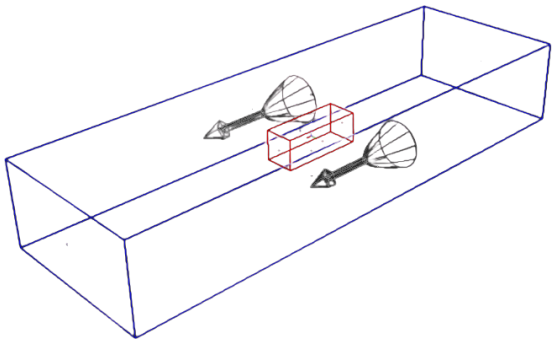

Figure 6.4: Geometric shape of SKYLON implemented in ASTOS

[2] the thrust values decrease as the Mach number increases.

Masses

The definition of SKYLON's masses is the cornerstone of the mission analysis at hand since it is through this that the developed methodology is applied. Indeed, the entered masses are part of the outputs of the iterative sizing code applied to the case study, except for the payload mass, for which the maximum mass defined in the User's Manual [2] is referenced. Table 6.3 presents the masses of SKYLON defined in the ASTOS scenario.

Payload mass	15'000 kg
Structural (dry) mass	55'648 kg
Propellant mass	270'260 kg

Table 6.3: Masses definition of SKYLON in the ASTOS scenario

The masses obtained from the developed methodology are inevitably slightly different from those of SKYLON due to the simplifications adopted to adapt the latter to the conceptual design of a wide range of aircraft.

Phases definition

The definition of mission phases in ASTOS is a task of significant importance and difficulty as it defines the dynamic configuration of the mission itself. Through the definition of phases, ASTOS is directed on which aerodynamic and propulsion databases to draw for a certain flight condition, and the vehicle's attitude is controlled.
Table 6.4 lists the identified phases to configure SKYLON's dynamics in ASTOS, along with the associated end phase conditions.

Phase:	**Description:**	**SABRE mode:**	**End condition(s):**
Take-Off	Take-Off with high values of AoA	Air-breathing	Altitude: 50 m
Low-Speed Climb	From subsonic flight to low supersonic speed Pitch angle decreasing	Air-breathing	Mach number: 1.5
Supersonic Climb	Last phase of air-breathing propulsion Pitch angle approx. constant	Air-breathing	Mach number: 5 Altitude: $\geq$28 km
Propulsive-mode Switch	Switch from air-breathing mode to rocket mode No thrust	-	Duration: 30 sec
Hypersonic Climb	Hypersonic speed with SABRE on rocket mode High values of AoA	Rocket	Mach number: 8.5
Hypersonic Climb pt.2	Orbit reaching with rocket AoA strongly decreasing	Rocket	Altitude: $\geq$90 km

Table 6.4: Phases description in the ASTOS scenario

6.2 Analysis Results

Once the scenario is defined, the mission simulation begins. If the inputs provided generate a feasible mission model, the simulation is successful ("*process terminated with status 0*") and outputs all the resulting data, which can be visualized in a highly customizable manner directly in ASTOS.

To verify the results of the conducted mission analysis and ensure the robustness of the developed methodology, the outcomes derived from the simulation are meticulously compared with those obtained from SKYLON, as provided by Reaction Engines Ltd. This comparative analysis aims to validate the accuracy and reliability of the conceptual design approach, thereby enhancing confidence in the derived mission parameters and performance predictions.

Consider the mission profile (altitude versus mission time) shown in figure 6.5. In the ASTOS analysis, it is not possible to simulate the Take-Off phase optimally as the ground roll is not considered, which in SKYLON's mission profile (figure 6.5b) takes about 100 seconds during which the spaceplane remains at zero altitude. Excluding this sub-phase, it can be observed that the profile obtained from the simulation (figure 6.5a) is very similar to the actual SKYLON profile (figure 6.5b). It can be seen that the air-breathing phase of the ascent occurs with a low Rate Of Climb, while the rocket phase is characterised by a high ROC. Corresponding to the propulsive mode switch there is a decrease in altitude.

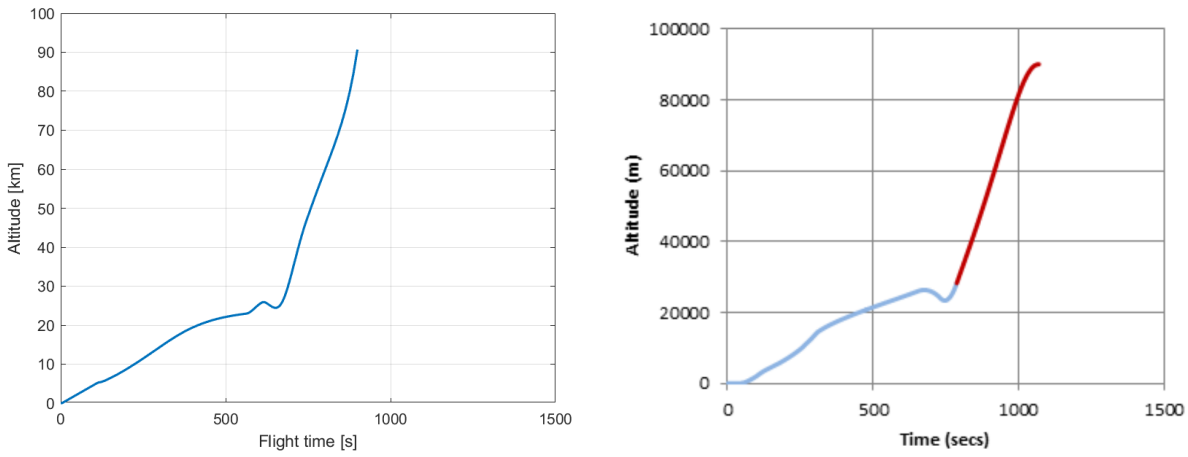

(a) Simulated (b) Given by User's Manual [2]

Figure 6.5: Mission profile of SKYLON

A similar discussion can be made with other mission characteristic quantities, such as the mass of the spaceplane and the flight Mach number as a function of mission time, depicted in figure 6.6 and figure 6.7, respectively. As can be observed, the total mass of the aircraft varies following the mass of the consumed propellant. Specifically, during the airbreathing phase, the temporal variation of mass remains low due to the high specific impulse of the airbreathing mode of the two SABRE engines. Conversely, a steep decrease in mass occurs during the rocket phase. Conversely, the flight Mach number exhibits an opposite trend.

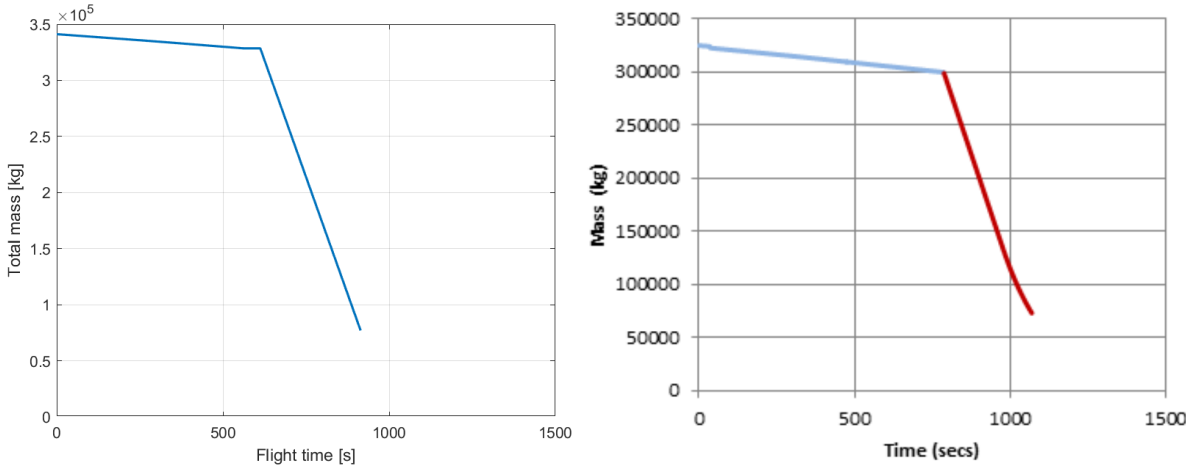

(a) Simulated (b) Given by User's Manual [2]

Figure 6.6: Total mass profile of SKYLON during the mission time

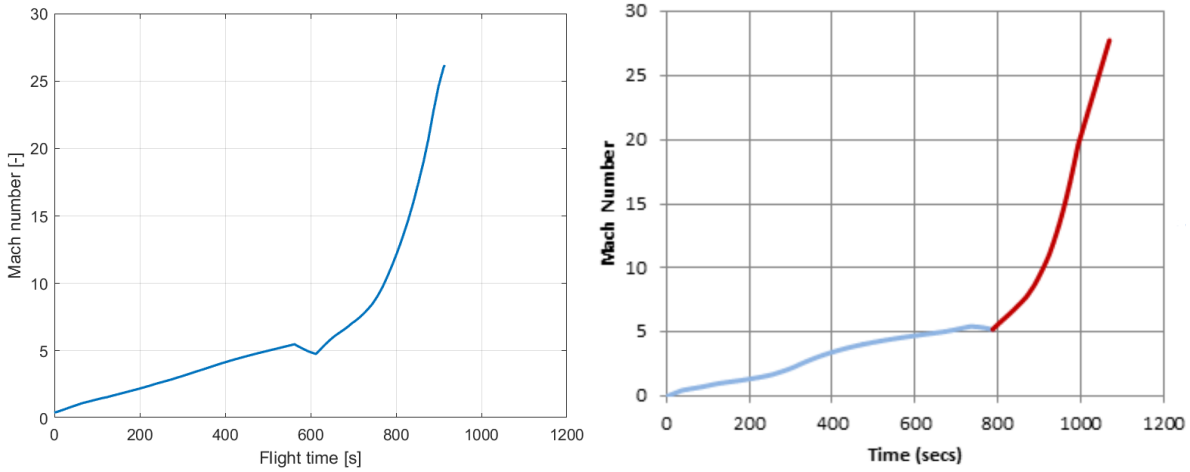

(a) Simulated (b) Given by User's Manual [2]

Figure 6.7: Flight Mach number of SKYLON during the mission time

A fundamental parameter to be verified is the propellant mass, which comes from the sizing code of the developed methodology. As can be seen from figure 6.8, which shows the profile of the consumed propellant as a function of the SKYLON altitude, the kilograms of fuel estimated by the methodology is sufficient to reach orbit. It can be noted that considering a target altitude of 100 km, there are approximately 7.5 tons of residual propellant, an additional quantity of fuel and oxidizer loaded aboard to ensure that there is sufficient reserve available to manage any deviations from the planned trajectory or to compensate for variations in engine performance during flight. This reserve is critical to ensuring the success of the mission and the safety of the crew or payload.

This demonstrates that the masses derived from the tool incorporating the methodology for SKYLON are accurate and translate into a feasible mission.

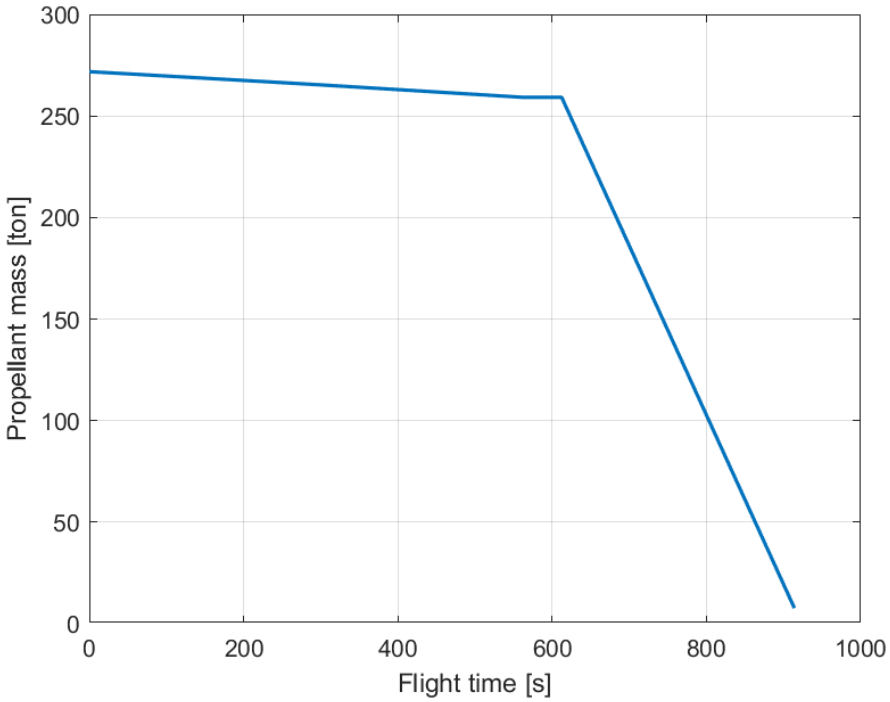

Figure 6.8: Simulated propellant consumption of SKYLON during the ascent

Chapter 7

Conclusion

The purpose of this thesis was to characterize the ascent phase in the conceptual design of reusable Single-Stage-To-Orbit (SSTO) vehicles, and subsequently to verify the reliability of the applied models and the developed methodology through ascent simulation using the commercial mission analysis software ASTOS. All efforts to achieve these objectives are detailed in the preceding pages, starting from the research of suitable aerodynamic models for SSTO vehicles to the study of propulsion models for orbital access, and concluding with the creation of a new formulation to be incorporated into the Matching Chart for the orbit attainment requirement and the ascent mission analysis.

In characterizing aerodynamics, an in-depth literature analysis was conducted to identify implementable aerodynamic models, which are relatively simple analytically yet reliable for all flight phases. This review work is significant as it identifies and reports suitable aerodynamic models for characterizing the ascent of a generic SSTO vehicle.

Subsequently, a study of propulsion systems helped understand the propulsion strategies that enable space access with a single-stage vehicle. For each of these systems, literature analysis was carried out, and formulations of thrust or specific impulse were reported to model their performance within the sizing code.

Significant effort was devoted to developing the orbit access requirement to be implemented in the Multiple Matching Charts, for which a new analytical formulation was created through a derivation from the Rocket Equation.

Lastly, as a verification of the developed conceptual design methodology, an ascent simulation was conducted using the commercial ASTOS mission analysis software. By inputting the analysis with the outputs of the developed code applied to SKYLON, mission data closely resembling the official SKYLON data were obtained. Through this, the validity and accuracy of the tool could be confirmed.

It is acknowledged that the present conceptual design tool has limitations related to the modelling of ascent. These limitations stem from the difficulty in finding a simple model capable of characterizing aerodynamics for all flight phases and configurations envisaged in the scenario. The models found represent a compromise between the required simplicity and good reliability. Additionally, the targeted aircraft of this work utilize extremely innovative

propulsion systems, currently under research, hence their modelling has been approximated as a transition between well-known engines (e.g., turbojet, ramjet, rocket), each representing a propulsion mode. Concerning the Matching Chart (MC), the new formulation incorporates semi-empirical parameters derived from literature, which may not entirely reflect current technologies. To enhance results, future developments could incorporate more complex and reliable aerodynamic models, especially for high Mach numbers (e.g., Newtonian theory). Furthermore, innovative engine models studied in this work will become available in the near future, enabling better propulsion characterization and a broader statistical database. Finally, a reevaluation of parameters used in the orbit attainment requirement formulation through the addition of corrective coefficients could be considered.

Remembering that this thesis work is part of an ambitious research project aimed at developing a conceptual design tool for fully reusable space access vehicles, it can be concluded that solid foundations have been laid upon which the tool can be completed and made available to researchers, students, and engineers. Given the constant and rapid growth in interest in reusable space access vehicles (even from space agencies such as the European Space Agency (ESA)), a potential application of this tool could be in the conceptual design of isolated configurations of these vehicles, providing a quick but reliable feasibility check.

Appendix A

MATLAB codes

This appendix contains the MATLAB codes developed during the thesis work and cited in the paper.

Supersonic air intake with prominent flat ramp [three ramps] sizing code:
N.B.: MATLAB Add-On "Oblique Shock Calculator" [45] is required.

```
function [eps_d,Amin,Ai] = SupersonicInletSizing(M,h,delta1,
   delta2,delta3)

if isempty(delta1)
    delta1=4.46;
end
if isempty(delta2)
    delta2=5.31;
end
if isempty(delta3)
    delta3=6.34;
end

gamma = 1.4;
[T0,~,P0,~] = atmosisa(h);
[~,Tratio,Pratio,~,~] = flowisentropic(gamma,M);
Ptot0 = 1/Pratio*P0;
Ttot0 = 1/Tratio*T0;

% first olique shock
M1 = M;
[beta1,~] = oblique_angle_calc(M1,'mach',delta1,'theta',gamma);
M1n = M1*sind(beta1);
[~,~,~,~,M2n,Ptot1,~] = flownormalshock(gamma,M1n,'mach');
```

```
M2 = M2n/sind(beta1-delta1);

% second oblique shock
Ptot2 = 1;              % inizialization
if(delta2~=0)
    [beta2,~] = oblique_angle_calc(M2,'mach',delta2,'theta',gamma
       );
    M2n_ = M2*sind(beta2);
    [~,~,~,~,M3n,Ptot2,~] = flownormalshock(gamma,M2n_,'mach');
    M3 = M3n/sind(beta2-delta2);
end

% third oblique shock
Ptot3 = 1;              % inizialization
if(delta3~=0)
    [beta3,~] = oblique_angle_calc(M3,'mach',delta3,'theta',gamma
       );
    M3n_ = M3*sind(beta3);
    [~,~,~,~,M4n,Ptot3,~] = flownormalshock(gamma,M3n_,'mach');
    M4 = M4n/sind(beta3-delta3);
end

% normal shock
if(delta2~=0 && delta3==0)
    M4 = M3;
elseif(delta2==0 && delta3==0)
    M4 = M2;
end
[~,~,~,~,M5,Ptot4,~] = flownormalshock(gamma,M4,'mach');

funM = @(Mach) sqrt(gamma)*Mach/(1+0.5*(gamma-1)*Mach^2)^((gamma
   +1)/(2*(gamma-1)));
R = 287.05;              % molar gas constant for air
m_dot = 382;             % statistical value

eps_d = Ptot1*Ptot2*Ptot3*Ptot4;                    % ram
   efficiency
Amin = m_dot*sqrt(R*Ttot0)/(Ptot0*eps_d*funM(M5)); % throat area
Ai   = Amin*eps_d*funM(M5)/funM(M);                % inlet area

end
```

Orbit reaching requirement analytical formulation code:

```
function [T_W] = orbitReachingReq(tau,W,W_pay,Mmax,h,ROC,Istr,
   rho_pay,DV)

g0 = 9.81;
Kv0 = 0.4*(rho_pay/175.6)^0.123;                % (metric)
Kv = (Kv0 - 6.867e-3*tau^-1 + 8.2777e-4*tau^-2 ...
    - 2.811e-5*tau^-3)*1.1857;                  % Scaled
       propellant volume fraction
Kstr = (0.317)*tau^0.205;                       % Structural
   coefficient
tb = h/ROC;                                     % Burning time
rho_f = 70.52;                                  % LH2 density [kg
   /m^3]
rho_ox = 1141;                                  % LOX density [kg
   /m^3]
MR = 6;                                         % Mixure ratio
rho_ppl = rho_f*(1+MR)/(1+(rho_f/rho_ox)*MR);   % Propellent
   density
Kw = -93.831*tau^3 + 59.920*tau^2 - 5.648*tau ...
    + 2.821;                                    % for wing body
Ip = 107.6*10^(-0.081*Mmax);                    % Propulsion
   index

a = Istr*Kv*Kstr*tau;
b = Ip*Kw;
W_ppl = @(W_S) (rho_ppl*W_pay*Kw./(a*W^0.71.*W_S.^-0.71-b));

T_W = @(W_S) W_ppl(W_S).*DV./ (W*g0*tb.*log(W./(W-W_ppl(W_S))));
end
```

Appendix B

Curran Parameters

Below are the parameters that appear in the formulation of the orbit reaching requirement for the Multiple Matching Charts (MMC). The definition of these is taken from the book *Scramjet propulsion* [5].

$$\tau = \frac{V_{tot}}{S_{pln}^{1.5}} \tag{B.1}$$

$$I_P = \frac{\rho_{\text{ppl}}}{\text{WR} - 1} = 107.6 \cdot 10^{-0.081 \cdot M_{\max}} \tag{B.2}$$

$$I_{str} = 20 \quad \text{(this parameter has been estimated from statistical analysis)} \tag{B.3}$$

$$K_w = -93.831\ \tau^3 + 59.920\ \tau^2 - 5.648\ \tau + 2.821 \tag{B.4}$$

$$K_v = (K_{v_0} - 6.867e-3\ \tau^{-1} + 8.2777e-4\ \tau^{-2} - 2.811e-5\ \tau^{-3}) \cdot 1.1857 \tag{B.5}$$

where

$$K_{v_0} = 0.4 \left(\frac{\rho_{pay}}{175.6}\right)^{0.123} \tag{B.6}$$

$$K_{str} = 0.317 \cdot \tau^{0.205} \tag{B.7}$$

Appendix C

SKYLON Dataset

In this appendix, the aerodynamic data of SKYLON and the propulsion data of the SABRE implemented in the ASTOS software for the mission analysis are reported.

Aerodynamic database:

Mach	**Alpha**	**CL**
0.30	-5	-0.23
0.30	0	-0.01
0.30	5	0.23
0.30	10	0.47
0.30	15	0.69
0.30	20	0.84
0.30	25	0.86
0.30	30	0.86
0.60	-5	-0.24
0.60	0	0.01
0.60	5	0.26
0.60	10	0.49
0.60	15	0.69
0.60	20	0.83
0.60	25	0.87
0.60	30	0.96
0.80	-5	-0.26
0.80	0	0.01
0.80	5	0.26
0.80	10	0.51
0.80	15	0.72
0.80	20	0.86
0.80	25	0.95

Mach	**Alpha**	**CD**
0.30	-5	0.024
0.30	0	0.007
0.30	5	0.029
0.30	10	0.083
0.30	15	0.159
0.30	20	0.281
0.30	25	0.396
0.30	30	0.494
0.60	-5	0.024
0.60	0	0.012
0.60	5	0.037
0.60	10	0.088
0.60	15	0.176
0.60	20	0.293
0.60	25	0.408
0.60	30	0.555
0.80	-5	0.034
0.80	0	0.017
0.80	5	0.029
0.80	10	0.086
0.80	15	0.191
0.80	20	0.313
0.80	25	0.452

0.80	30	1.01		0.80	30	0.594
0.95	-5	-0.32		0.95	-5	0.071
0.95	0	0.01		0.95	0	0.042
0.95	5	0.31		0.95	5	0.059
0.95	10	0.63		0.95	10	0.137
0.95	15	0.90		0.95	15	0.262
0.95	20	1.09		0.95	20	0.411
0.95	25	1.21		0.95	25	0.572
0.95	30	1.25		0.95	30	0.751
1.05	-5	-0.32		1.05	-5	0.076
1.05	0	0.01		1.05	0	0.051
1.05	5	0.28		1.05	5	0.073
1.05	10	0.57		1.05	10	0.144
1.05	15	0.85		1.05	15	0.264
1.05	20	1.09		1.05	20	0.428
1.05	25	1.29		1.05	25	0.631
1.05	30	1.39		1.05	30	0.831
1.20	-5	-0.29		1.20	-5	0.073
1.20	0	-0.02		1.20	0	0.051
1.20	5	0.24		1.20	5	0.068
1.20	10	0.50		1.20	10	0.130
1.20	15	0.77		1.20	15	0.240
1.20	20	1.01		1.20	20	0.399
1.20	25	1.21		1.20	25	0.594
1.20	30	1.34		1.20	30	0.800
1.60	-5	-0.28		1.60	-5	0.066
1.60	0	-0.07		1.60	0	0.042
1.60	5	0.17		1.60	5	0.054
1.60	10	0.41		1.60	10	0.108
1.60	15	0.63		1.60	15	0.200
1.60	20	0.83		1.60	20	0.335
1.60	25	1.03		1.60	25	0.506
1.60	30	1.21		1.60	30	0.724
2.00	-5	-0.24		2.00	-5	0.064
2.00	0	-0.05		2.00	0	0.039
2.00	5	0.17		2.00	5	0.051
2.00	10	0.37		2.00	10	0.095
2.00	15	0.56		2.00	15	0.178
2.00	20	0.74		2.00	20	0.296
2.00	25	0.92		2.00	25	0.457
2.00	30	1.09		2.00	30	0.655

3.00	-5	-0.17	3.00	-5	0.049
3.00	0	-0.02	3.00	0	0.029
3.00	5	0.14	3.00	5	0.039
3.00	10	0.29	3.00	10	0.078
3.00	15	0.43	3.00	15	0.142
3.00	20	0.59	3.00	20	0.240
3.00	25	0.75	3.00	25	0.374
3.00	30	0.91	3.00	30	0.550
4.00	-5	-0.12	4.00	-5	0.039
4.00	0	-0.01	4.00	0	0.024
4.00	5	0.11	4.00	5	0.034
4.00	10	0.23	4.00	10	0.068
4.00	15	0.36	4.00	15	0.125
4.00	20	0.51	4.00	20	0.210
4.00	25	0.67	4.00	25	0.333
4.00	30	0.81	4.00	30	0.496
5.50	-5	-0.09	5.50	-5	0.032
5.50	0	-0.01	5.50	0	0.024
5.50	5	0.08	5.50	5	0.029
5.50	10	0.18	5.50	10	0.054
5.50	15	0.30	5.50	15	0.105
5.50	20	0.44	5.50	20	0.186
5.50	25	0.59	5.50	25	0.303
5.50	30	0.75	5.50	30	0.460
5.94	9	0.19	5.936	9.324	0.068
6.67	12	0.23	6.673	11.583	0.086
7.48	13	0.26	7.483	12.779	0.095
8.58	12	0.24	8.577	12.453	0.088
10.13	11	0.18	10.131	10.626	0.064
12.19	8	0.13	12.189	7.512	0.042
14.95	4	0.08	14.952	3.510	0.027
16.97	1	0.07	16.969	0.907	0.024

Table C.1: Aerodynamic data of the SKYLON for air-breathing phase (source: MORE&LESS project, Politecnico di Torino)

Propulsive database:

Mach number	**F_u [kN]**
0.0034	612.8280

Mach number	**F_g [KN]**
0.0048	613.3992

0.1100	621.5371
0.1845	629.3827
0.3976	647.6756
0.5005	656.3859
0.5645	653.7396
0.7849	644.9161
0.8810	637.8855
0.9805	636.9760
1.2043	647.3933
1.2966	653.4835
1.3747	658.7040
1.6021	669.1200
1.6802	670.8420
1.7762	674.3070
2.0106	680.3474
2.0818	672.4508
2.1671	666.2985
2.4018	650.4729
2.4730	642.5763
2.5618	637.2974
2.7823	618.8529
2.8606	613.5777
2.9530	606.5483
3.1451	588.1137
3.2340	580.2109
3.3407	571.4272
3.5292	551.2447
3.6323	544.2115
3.7319	536.3049
3.9275	515.2452
4.0164	509.0917
4.1125	500.3117
4.3400	483.6141
4.4254	479.2110
4.5178	473.0562
4.7454	456.3585
4.8094	451.9630
4.9054	444.0577
5.0014	442.2748

0.0690	629.1537
0.1474	645.7871
0.3935	700.061
0.4755	717.5696
0.5753	731.5885
0.7179	745.6223
0.8106	754.3947
0.9211	762.2994
0.9924	769.3163
1.0851	787.7026
1.1600	801.7128
1.3561	831.4973
1.4274	846.3802
1.5059	857.7696
1.7233	883.1916
1.8160	894.586
1.8980	902.4806
2.0976	920.9044
2.1939	922.686
2.2830	928.8352
2.5040	936.7784
2.6002	941.1821
2.6857	943.834
2.9103	954.4004
3.0030	957.9288
3.1027	957.9637
3.3059	961.5307
3.4021	965.0604
3.5126	965.973
3.7443	967.802
3.8441	971.3329
3.9367	970.4913
4.1577	974.9385
4.2361	977.5879
4.3074	977.6128
4.5711	980.327
4.6566	979.4829
4.7529	981.2646
4.9845	983.9675

Table C.2: Propulsive data of the SABRE engine (source: Reaction Engine Ltd.)

Bibliography

[1] Ernst Heinrich Hirschel. *Basics of Aerothermodynamics: Second, Revised Edition.* Springer International Publishing, Cham, 2nd ed. 2015 edition, 2015. (Cited on pages 6 and 14.)

[2] Bond. A. and M. Longstaff, R. Hempsell. SKYLON Users' Manual. 1.1, 2010. (Cited on pages 6, 23, 24, 25, 27, 79, 80, 82, 83, and 84.)

[3] Victor Fernandez Villace. Simulation, Design and Analysis of Air-Breathing Combined-Cycle Engines for High Speed Propulsion, 2022. (Cited on pages 6, 23, 26, and 80.)

[4] Giovanni Grimaldi. Development of a conceptual design tool to predict performance and pollutant and ghg emissions of high-speed vehicles using liquid hydrogen, 2021-12-10. (Cited on pages 6, 23, and 27.)

[5] S.N.B. Murthy, E.T. Curran, S.N.B. Murthy, S.N.B. Murthy, and E.T. Curran. *Scramjet propulsion / ed. by E.T. Curran, S.N.B. Murthy.* Progress in astronautics and aeronautics ; v. 189. AIAA, Reston, 2000. (Cited on pages 6, 23, 29, 30, 74, 75, 77, and 92.)

[6] Egbert Torenbeek. *Essentials of supersonic commercial aircraft conceptual design.* Aerospace series. Wiley, Hoboken, New Jersey, 2020. (Cited on pages 6, 23, 31, 33, and 37.)

[7] Daniel P. Raymer. *Aircraft design: a conceptual approach.* AIAA Education Series. AIAA, Reston, 5th ed edition, 2012. (Cited on pages 6, 23, and 43.)

[8] Ming Tang, Booz Allen Hamilton, and Ramon L Chase. The Quest for Hypersonic Flight with Air-Breathing Propulsion. *AIAA paper*, 2008. (Cited on pages 7, 23, and 49.)

[9] Ernst Heinrich Hirschel, Claus Weiland, and Ernst Heinrich Hirschel. *Selected aerothermodynamic design problems of hypersonic flight vehicles.* Springer, Berlin Heidelberg, 2009. (Cited on pages 7, 23, 29, and 49.)

[10] Federal Aviation Administration. Transition to jet-powered airplanes. In *Airplane Flying Handbook*. Skyhorse Publishing Company, Incorporated, United States, 2022. (Cited on pages 7, 23, 50, and 51.)

[11] Dario Pastrone. Lecture notes in jet propulsion. Master's Course in Aerospace Engineering, Politecnico di Torino, March 2023. (Cited on pages 7, 23, 51, 52, 68, and 69.)

[12] Philip G. Hill, Carl R. Peterson, and Philip G. Hill. *Mechanics and thermodynamics of propulsion / Philip G. Hill, Carl R. Peterson.* Addison-Wesley, Reading (Mass.), 2nd ed. edition, 1992. (Cited on pages 7, 23, 50, 52, 53, 54, and 55.)

[13] Ahmed F El-Sayed. *Fundamentals of Aircraft and Rocket Propulsion.* Springer London, Netherlands, 1 edition, 2016. (Cited on pages 7, 23, and 54.)

[14] Dora Musielak. *Scramjet propulsion: a practical introduction.* Aerospace. John Wiley and Sons, Incorporated, Hoboken, New Jersey, 2023. (Cited on pages 7, 23, 48, 55, 56, and 67.)

[15] H.E. Tacca, P. Rachov, and Diego Lentini. Electric feed systems for liquid propellant rocket engines. 12 2010. (Cited on pages 7, 23, and 57.)

[16] The Quest for Hypersonic Flight with Air-Breathing Propulsion. In *American Institute of Aeronautics and Astronautics. AIAA Conference Papers*, Reston, 2008. American Institute of Aeronautics and Astronautics. (Cited on pages 7, 23, and 62.)

[17] Roger Longstaff and Alan Bond. The SKYLON Project. In *17th AIAA International Space Planes and Hypersonic Systems and Technologies Conference.* American Institute of Aeronautics and Astronautics, 2011. (Cited on pages 7, 23, and 64.)

[18] Zhihua Xi, Haibo Zhang, Ming Chen, Changpeng Cai, and Jian Wang. Design of thrust augmentation control schedule during mode transition for turbo-ramjet engine. *Aerospace science and technology*, 138:108352–, 2023. (Cited on pages 7, 23, and 66.)

[19] Harinkumar Patel. Conceptual Design Level Airframe/Propulsion Integration Using the Generic Synthesis Framework AVDS: Application to Supersonic and Hypersonic Aerospace Vehicles, 2022. (Cited on pages 7, 23, and 70.)

[20] Unmeel Mehta, Michael Afosmis, Jeffrey Bowles, and Shishir Pandya. Skylon Aerodynamics and SABRE Plumes. In *NASA Center for AeroSpace Information (CASI). Conference Proceedings*, Hampton, 2015. NASA/Langley Research Center. (Cited on pages 7, 23, 79, and 80.)

[21] Joseph N. Pelton. *The World of Space in Flux*, pages 1–14. Springer International Publishing, Cham, 2019. (Cited on pages 11 and 12.)

[22] Norbert Frischauf, Rainer Horn, Tilo Kauerhoff, Manfred Wittig, Ingo Baumann, Erik Pellander, and Otto Koudelka. Newspace: New business models at the interface of space and digital economy: Chances in an interconnected world. *New Space*, 6(2):135–146, 2018. (Cited on page 11.)

[23] Loïs Miraux. Environmental limits to the space sector's growth. *Science of The Total Environment*, 806:150862, 2022. (Cited on page 12.)

[24] S. Salvi, C. Paravan, and L. Galfetti. SSTO Reusable Launchers: a Critical Comparison of Propulsion Concepts, 2022. (Cited on pages 13, 23, 62, and 63.)

[25] Bhavana Y. Reusable launch vehicles: Evolution redefined. *Journal of aeronautics & aerospace engineering*, 2(2), 2013. (Cited on page 13.)

[26] Steven J Dick and Roger D Launius. Reusable Launch Vehicles or Expendable Launch Vehicles? A Perennial Debate. In *Critical Issues in the History of Spaceflight*. Nova Science Publishers, Incorporated, United States, 2018. (Cited on page 15.)

[27] R. L. Chase. *Earth-to-orbit reusable launch vehicles: A comparative assessment*. Legacy CDMS, 1978. (Cited on page 17.)

[28] C. Gelzer. Rockwell x-30. `https://www.nasa.gov/aeronautics/aircraft/x-30/`, 2016. (Cited on page 17.)

[29] Flug revue, 1989. (Cited on page 18.)

[30] R GOPALASWAMI, S Gollakota, P Venugopalan, M Nagarathinam, and A Sivathanu Pillai. Concept definition and design of a single-stage-to-orbit launch vehicle- hyperplane. In *IAF, International Astronautical Congress, 39th, Bangalore, India; INTERNATIONAL ORGANIZATION; 8-15 Oct. 1988*, 1988. (Cited on page 19.)

[31] Radian Aerospace. Radian Aerospace Official Site. `https://www.radianaerospace.com/`, 2024. Accessed: April 2024. (Cited on page 20.)

[32] L. J. Williams. *Estimated aerodynamics of all-body hypersonic aircraft configurations*. Legacy CDMS, 1971. (Cited on pages 23 and 38.)

[33] Claus Weiland. *Aerodynamic Data of Space Vehicles*. Springer Berlin Heidelberg, Berlin, Heidelberg, 2014. edition, 2014. (Cited on pages 23 and 44.)

[34] Luca Nepote Fus. Methodology and tools to improve the aerodynamic characterization of high-speed vehicles during the conceptual design phase, 2021-04-13. (Cited on pages 23 and 45.)

[35] Davide Ferretto, Roberta Fusaro, and Nicole Viola. A conceptual design tool to support high-speed vehicle design. 2020. (Cited on pages 23 and 31.)

[36] Diego Lentini. Fundamentals of rocket propulsion. `http://dma.dima.uniroma1.it:8080/STAFF2/baires18_Seminar.pdf`, September 2018. (Cited on pages 23 and 59.)

[37] Matthew M. Peet. Lecture notes in spacecraft dynamics and control. `https://control.asu.edu/Classes/MAE462/462Lecture11.pdf`, 2023. (Cited on pages 23 and 59.)

[38] Roger R. Bate, Donald D. Mueller, Jerry E. White, and Roger R. Bate. *Fundamentals of astrodynamics / Roger R. Bate, Donald D. Mueller, Jerry E. White*. Dover books on astronomy and astrophysics. Dover, New York, 1971. (Cited on pages 23 and 61.)

[39] Tian-tian Zhang, Zhen-guo Wang, Wei Huang, Jian Chen, and Ming-bo Sun. The overall layout of rocket-based combined-cycle engines: a review. *Journal of Zhejiang University. A. Science*, 20(3):163–183, 2019. (Cited on pages 23 and 64.)

[40] A Siebenhaar and M Bulman. The Strutjet engine - The overlooked option for space launch. In *31st Joint Propulsion Conference and Exhibit*. American Institute of Aeronautics and Astronautics, 1995. (Cited on pages 23, 63, and 64.)

[41] R. F Cao, J. T Chang, J. F Tang, Z. Q Wang, and D. R Yu. Study on combustion mode transition of hydrogen fueled dual-mode scramjet engine based on thermodynamic cycle analysis. *International journal of hydrogen energy*, 39(36):21251–21258, 2014. (Cited on pages 23 and 66.)

[42] Davide Ferretto, Roberta Fusaro, and Nicole Viola. Innovative multiple matching charts approach to support the conceptual design of hypersonic vehicles. *Proceedings of the Institution of Mechanical Engineers. Part G, Journal of aerospace engineering*, 234(12):1893–1912, 2020. (Cited on pages 23 and 73.)

[43] T. Molinari. Conceptual design methodology and tool for reusable single-stage-to-orbit vehicles with horizontal take-off and landing, 2024. (Cited on pages 23 and 77.)

[44] The MathWorks Inc. Matlab version: 9.12.0 (R2022a). `https://www.mathworks.com`, 2022. (Cited on page 46.)

[45] Jason Ryan. Oblique Shock Calculator. `https://www.mathworks.com/matlabcentral/fileexchange/44756-oblique-shock-calculator`, 2013. Accessed: April 2024. (Cited on page 89.)